Biomechanics of the Insect Flight Motor

Rachel Han Soc Tran

PhD Thesis

Submitted in accordance with the requirements for the degree of

Doctor of Philosophy

The University of Leeds

School of Biomedical Sciences

February 2024

Intellectual Property Rights

The candidate confirms that the work submitted is her own and that appropriate credit has been given where reference has been made to the work of others.

Acknowledgements

I would first like to thank my supervisors, Dr Simon Walker and Dr Graham Askew for their patience and wisdom throughout this PhD. Without their guidance, this research would not have been possible. My gratitude extends to the University of Leeds for the funding opportunity and my collaborators, Prof. Richard Bomphrey (RVC), Prof. Joerg Albert (UCL) and Dr Paloma Gonzalez-Bellido (UMN) for their insightful comments and suggestions. Also, to Marcos Georgiades (RVC) and David Munkvold (UMN) for their brief assist during data collection.

I am also deeply grateful for the other members of Garstang 5.61. Cowboy Scott for our back-and-forth on insect flight lingo. Dr Doody for her continuous support before conference presentations and her maths brain. Aziz for providing delicious office snacks and teaching everyone in Yorkshire DeepLabCut. Maddie for her wild stories on Concord Street, and Dani for our impromptu meals and online writing sessions.

Shout out to my mum, not so little brother Alexander and friends, Emily, Safi, and Asiya for their unwavering belief in me. Lastly, special thanks to my sister Natalie for her time proofreading my work and cooking for me during my write up period.

Abstract

This thesis presents novel insights into the free-flight kinematics of pterygotes; a new standard for reporting high-precision insect body, leg and wing kinematics, the importance of non-wing appendages on flight stability, methods for handling large datasets and time-varying parameters to test against independent variables, and how insects generate extreme manoeuvres. Research here was facilitated by the development and use of a new ten high-speed camera rig to acquire footage, followed by a completely automated voxel-carving package to report kinematics of unprecedented resolution including wing torsion and bending. *Anopheles* (mosquito) underwent substantial wing deformation with varying ambient temperature and stimuli to encourage flight manoeuvres. Wing kinematics were significantly different between male and female subjects. Meanwhile, subjects were able to reduce their stroke amplitudes to angles lower than any other flying insect previously reported in literature. With a supplementary leg tracker and centre of mass measurements, mosquito legs were also shown to contribute substantially to flight stability in the roll axis, whilst damaged mosquitoes that had experienced leg loss adjusted the kinematics of remaining limbs. Wingbeat frequency increased with temperature but plateaued at different temperatures for male and female subjects. Whilst, overall body kinematics did not correlate with temperature. This subsequently led to the Fourier fitting and principal component analysis of the same mosquito dataset, to create descriptor wingbeats to test the effect of temperature and estimate other summary parameters (e.g., stroke plane) while compacting data. Aerial hunters, *Coenosia* (killer fly), performed a large range of manoeuvres from backwards to upside down flight in the presence of one of two different configurations of artificial prey available. Incredibly high angular rates and accelerations were achieved whilst maintaining subtle changes in wing kinematics. These insights may feed into topics of flight control, aerodynamics and the development of micro-air vehicles.

Table of Contents

List of Figures

List of Tables

List of Equations

Abbreviations

Re	Reynolds number
ρ	Fluid density
V	Velocity
l	Length
μ	Dynamic viscosity
L	Lift
D	Drag
C_L	Lift coefficient
C_D	Drag coefficient
ρ	Air density
U	Speed
S	Surface area
AR	Aspect ratio
ϕ	Roll (x-axis of rotation)
θ	Pitch (y-axis of rotation)
Ψ	Yaw (z-axis of rotation)
φ	Stroke angle
θ	Deviation angle
ω	Pitch angle
φ_{leg}	Swing angle
θ_{leg}	Elevation angle
ω_{leg}	Tilt angle
$\{X_b, Y_b, Z_b\}$	Body axis system

$\{X_L, Y_L, Z_L\}$	Left wing axis system
$\{X_R, Y_R, Z_R\}$	Right wing axis system
$\{X_{Lleg}, Y_{Lleg}, Z_{Lleg}\}$	Left leg axis system
$\{X_{Rleg}, Y_{Rleg}, Z_{Rleg}\}$	Right leg axis system
r	Wings radical coordinate
A	Amplitude
r	Radius
$I_{ellipsoid}$	Moment of inertia of an ellipsoid
I_{body}	Total body moment of inertia
I_{sphere}	Moment of inertia of a sphere
I_{legs}	Total leg moment of inertia
m	Mass
a	Ellipsoids semi-major axis
b	Ellipsoids semi-minor axis
d	Distance
$\dot{V}O_2$	Oxygen consumption
$\dot{V}CO_2$	Carbon dioxide output
K_0	Time linear variable
K_1	Constant offset
$f(\varphi)$	Any kinematic parameter
K_A^{φ}	Fourier output per wingbeat
X^{φ}	Fourier output per sequence
X	Principal component decomposition matrix
n	Harmonic order
T	Transpose

C	PC coefficients
S	PC scores
P	Significant PC coefficients
R	Significant PC scores
m	Mean
LoS	Line of sight
PN	Proportional navigation
$\dot{\gamma}$	Rotation rate
N	Navigation constant
$\dot{\lambda}$	Line of sight rotation rate
MAV	Micro-air vehicle
LAZA	Liquid-amplified zipping actuator
LEV	Leading edge vortex
TEV	Trailing edge vortex
MOI	Moment of inertia
COM	Centre of mass
TTM	Tegro-trochanter muscle
EDT	Extracoxal depressor trochanter muscle
DVM	Dorsal ventral muscle
DLM	Dorsal longitudinal muscle
SR	Sarcoplasmic reticulum
B1 - 3	Basalar muscles
I1 and I2	First axillaries / Pterales I muscles
III1-4	Third axillaries / Pterales III muscles

Hg1 - 4	Fourth axillaries/ Posterior notal wing process muscles
EMG	Electromyography
Tn	Troponin
TnC	Troponin C
Tm	Tropomyosin
TnT	Troponin subunit T
TnI	Troponin subunit inhibitory
ATP	Adenosine triphosphate
ADP	Adenosine diphosphate
Pi	Inorganic phosphate
Ax1	Pterales I
Ax2	Pterales III
Ax3	Posterior notal wing process
PWP	Pleural wing process
RS	Radical stop
LPTCs	Lobular plate tangential cells
R-cells	Retinula cells
CFF	Critical flicker fusion frequency
FFF	Flicker fusion frequency
3D	3-dimensional
2D	2-dimensional
LED	Light emitting diode
PWM	Pulse width modulation
ROI	Region of interest
GUI	Graphic user interface

dof	Degrees of freedom
PCA	Principal component analysis
PC	Principal component
FFT	Fast Fourier transform
Vel	Velocity
Acc	Acceleration
WL	Wing length
SD	Standard deviation
BET	Blade element theory
CFD	Computational fluid dynamics
RVC	Royal Veterinary College
UCL	University College London
UMN	University of Minnesota

Chapter 1

General Introduction

1.1 Introduction of Insect Flight Biomechanics

Insects are one of the most successful organisms, with over one million named species, and an estimated 8.4 million undiscovered species that colonise a wide range of environments (Stork, 2018). They were also the first to achieve aerial locomotion 400 million years ago and remain the most competent fliers to date, performing the most complex manoeuvres such as upside down flight and saccadic turns (Ross, 2017, Misof et al., 2014). Some insects have developed additional flight behaviours besides locomotion. Male mosquitoes for instance increase their wingbeat frequency to attract nearby females without any obvious benefit in aerodynamic force production (Somers et al., 2022). Insects are therefore an excellent model that demonstrates the use of fundamental aerodynamics at low Reynolds numbers (where fluid flowing around the wing is more laminar as viscous forces dominate, see **Section 1.3**) despite challenges imposed by scaling as insects must remain small due to their reliance on passive diffusion of gases (lack of an active circulatory system) to respire, and cuticular exoskeleton for support.

In this thesis, I thereby ignore the wingless and only take interest in the pathways leading up to the development of their wings and flight ability. Pterygotes are a subclass of winged and secondary wingless (insects whose ancestors had wings)

insects composed of *Neoptera* (e.g., *Diptera* (flies), *Coleoptera* (beetles)), *Palaeoptera* (*Ephemeroptera* (mayflies) and *Odonata* (dragonflies and damselflies)) and unclassified *Pterygota* (Almudi et al., 2020). These can then be segregated usefully into those that possess one (*Diptera*) or two (e.g., *Odonata*) pairs of wings used for flight, as insects with one pair of wings are easier to investigate due no fore- and hind-wing wake interactions. When studying insect flight there are two approaches, (I) tethered flight and (II) free flight. (I) Tethered flight involves a physical attachment to the insect's thorax (fixed body axis and usually dorsally) and has been used when studying together highly sensitive neurological systems prone to error (noise) and wing kinematics simultaneously (Balint and Dickinson, 2001, Balint and Dickinson, 2004). (II) Whereas in free flight experiments, the insect is allowed to fly freely (naturally) but often in a chamber when exploring body and wing kinematics at varying degrees of resolution and accuracy for example, when only extracting flight paths and wingbeat frequencies versus wing kinematics such as wing torsion (Walker et al., 2009, Rossoni et al., 2021). Both studying techniques have trade-offs that must be considered but both enable the estimation of aerodynamic force production (Bomphrey et al., 2017, Urca et al., 2020). Several papers have reported the effects of tethering to significantly change wingbeat frequency by limiting thorax deformation (Arthur et al., 2014, Cator et al., 2011). Whilst Villarreal et al. (2017) found no significant difference between the two techniques, thereby warranting further investigation, but likely to be due to differences in tethering technique such as point of attachment and type of adhesive used (Villarreal et al., 2017).

One obvious or common aim littered throughout the introductions of primary literature, is the application of this knowledge to ultimately elevate micro-air

vehicle (MAV) production and performance for surveillance and sample collection in harsh and humanly unreachable terrain. Existing insect-inspired MAVs such as RoboBee X-Wing (Jafferis et al., 2019) and robotic fly (Fuller et al., 2014) still lack agility in comparison to their living counterparts. When building a biomimetic MAV, a complex framework is required to use a flapping mechanism and operate at similar spatiotemporal scales to flying insects. Ideally, quick actions involving sensing that then lead to changes in wing kinematics must exceed or match the speed, or even better predict turbulent external stimuli (forces) that may come interplay. A more recent pursuit in MAV development suggested we step away from transmission systems (e.g. four-bar crank-rocker (Coleman et al., 2015) and gear box (Nguyen et al., 2016)) as an intermediate between actuators and wings, and instead use liquid amplified electrostatic forces at the wing hinge called ‘LAZA’ (liquid-amplified zipping actuator) to limit mass and energy loss (Helps et al., 2022).

In this general introduction, I discuss neuromuscular make-up, the energy transduction pathways spanning mechanical energy (mechanical work output) to the kinematic output (wing hinge movement and aerodynamic output) of the insect flight motor, and the aims of the upcoming chapters of this thesis. Any progress within these departments should provide further insight on phylogenetic relationships/gaps, and how they manoeuvre.

1.2 Power Requirements

The power requirements of flight arises the organisms size, which is closely related to metabolic rate, and its low density environment with air having a density approximately 800-fold lower than water (Biewener and Patek, 2018b, Niven and Scharlemann, 2005). Hovering insects must generate sufficient power (force $\times$ velocity) to meet the costs of induced power to maintain lift and overcome gravity, profile power to overcome drag on wings and overcome the inherent inefficiencies throughout the system. To some extent they must also meet the costs of inertial power to accelerate and decelerate wings during stroke reversal, if the recovery of elastic energy from the previous stroke is insufficient (Ellington and Lighthill, 1984b). When manoeuvring by non-hovering flight, the power to produce thrust and parasite power evoked by body drag are further additional costs.

1.3 Aerodynamics

Aerial locomotion's minimum cost of transport, (energy spent per unit distance travelled) is greater than terrestrial and aquatic locomotion but is the fastest method over a given distance when considering ecological hurdles such as a lake or an inclining landscape. Most insects have therefore greatly benefited from flight: by gaining access to otherwise difficult to reach sources of food, water, prospective mates, and agility to escape danger. Though these aerial abilities do not come easy, as wings must provide both lift (downward fluid acceleration) and thrust (backward fluid acceleration and adjustment of force vectors).

1.3.1 Conventional Aerodynamics

Before discussing how flapping insects provide weight support and overcome drag when experiencing unsteady aerodynamic effects, it is useful to understand how aerodynamic forces (lift, drag) are created when steady air flow passes a non-oscillating wing. Overall lifting flow is thought to be the outcome of a translational component (inviscid conditions) and a circulatory component (viscosity present) of air flow when the Kutta condition is satisfied (**Figure 1.1**) (Biewener and Patek, 2018b). The Kutta condition is when circulation around an airfoil (bound vortex) with a sharp trailing edge is sufficient enough so that the flow at the trailing edge (stagnation point) separates from the airfoil smoothly (Ellington and Lighthill, 1984a). When oncoming airflow first encounters the blunt

leading edge of an asymmetric airfoil (wing) it separates into two streams above and below its surface. The two streams flow at different velocities as airflow speeds up and stretches out when passing over the curved upper surface of the airfoil. This is the result of the stream above being accelerated downwards towards the trailing edge in part by the circulatory component of bound (vortex) circulation around the airfoil. By Bernoulli's principle, the high velocity region above the wing therefore has low pressure and the low velocity region below the wing has high pressure (Ellington and Lighthill, 1984a). It is with this pressure difference around the airfoil that enables the production of lift, a net upward force perpendicular to the oncoming airflow. Vorticity that is a source of induced drag is also developed along the wing's length (wing tip) when high pressure air from below moves and intercepts the low-pressure air above and is shed at the wings trailing edge (wing tip vortex).

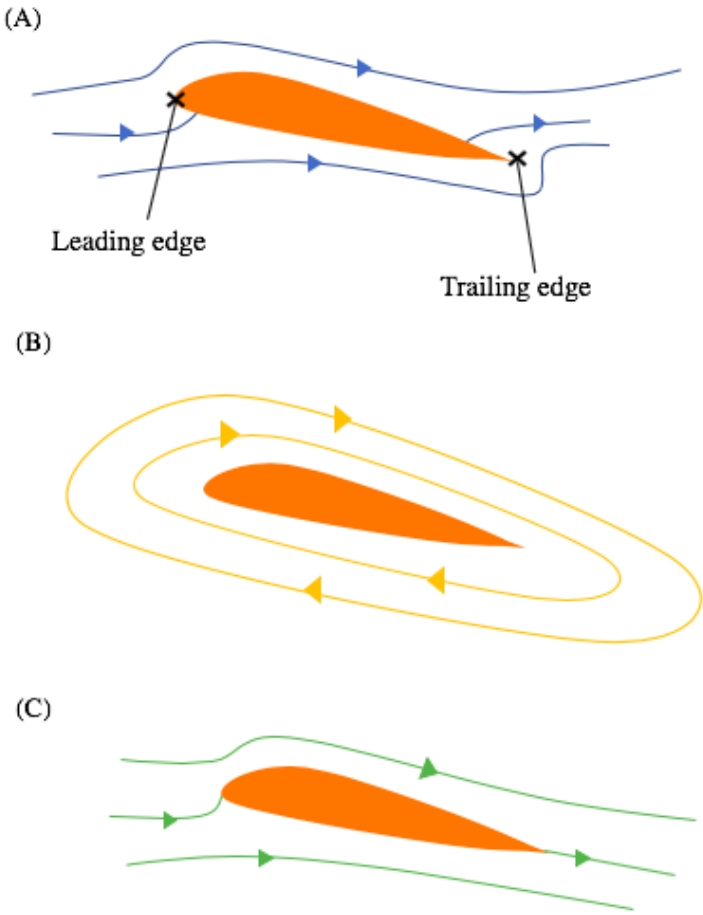

Figure 1.1 Kutta Condition

(A) Translational flow (blue) around an airfoil (orange) under inviscid (no viscosity) conditions. (B) Circulatory flow (yellow) around an airfoil when viscosity is present. (C) Overall lifting flow (green), outcome of translational and circulatory components when the Kutta condition is satisfied. Figure adapted from (Ellington and Lighthill, 1984a).

An asymmetric airfoil typically consists of a camber meaning that the upper surface is convex, and the surface below is concave. Cambered airfoil's encourage the pressure gradient described above, as the wings trailing edge is angled down and is therefore akin to a flat plate wing positioned at a high angle of attack (the angle the wing presents itself to oncoming flow). This means that

the subsequent lift production in a cambered airfoil remains possible at even low angles of attack (Liang and Li, 2018). To further increase lift, the angle of attack may be increased however, this also increases drag (force that acts parallel to the incoming air stream) and at a critical point will cause the wing to experience stall. Stall occurs when the attached flow on the upper surface (low pressure region) of the wing detaches causing a drop in lift (Laitone, 1997). Furthermore, on the wings surface there is a boundary layer where viscosity is zero and fluid molecules stick to its surface. When viscosity increases and the boundary layer is disturbed (turbulent flow), viscous drag develops as the velocity of the closely passing free stream flow increasingly slows down nearer to the wings surface (Videler, 1995). This occurs because more molecules of the passing fluid collide with those sticking on the wings surface (static), consequently causing them to slow down as kinetic energy between the two is transferred upon contact.

Equation 1.1 Reynolds number

$$Re = \frac{\rho V l}{\mu}$$

The thickness and status (laminar to turbulent) of a boundary layer can be portrayed within a dimensionless number called Reynolds number (*Re,* **Equation 1.1**) where ρ is fluid density, *V* is velocity of the fluid, *l* is length and μ is dynamic viscosity. *Re* may also be defined as the ratio between inertial force and vicious force, where an airfoil with a higher *Re* value is usually larger and the boundary

layer more turbulent. The *Re* of flying insects has been found to operate broadly between approximately 10 to 10^5 (Dudley, 2000a).

1.3.2 Unconventional Aerodynamics

Flying insects have thin cambered wings and stereotypically beat their wings in a reciprocal motion. Lift can be produced during the downstroke or both the upstroke and downstroke in some insects (**Figure 1.2**). In *Diptera*, at the end of each half stroke the wing rotates so that at the end of the downstroke, the wing supinates as the morphologically ventral side of the wing becomes aerodynamically dorsal. At the end of the upstroke the wing pronates so that the ventral side of the wing faces down.

Insects such as unusually proportioned honeybees with their large body mass when pollen loading (Feuerbacher et al., 2003), and minute fruit flies (Sun and Tang, 2002) use unsteady flow mechanisms when flapping. These boost aerodynamic force production beyond what is possible with steady-aerodynamics and attached flow (Taylor, 2012). Four separate unsteady aerodynamic mechanisms: (I) leading-edge vortex (LEV), (II) clap and fling, (III) rotational lift and (IV) wake recapture have been identified in insects over the years to increase lift (Biewener and Patek, 2018b).

(I) The LEV is a separating flow mechanism that develops along the span of the wing at high angles of attack, and is considered a common lift generation mechanism present in a large number of flying animals e.g., hummingbirds (Warrick et al., 2009) and bats (Muijres et al., 2008). Insects particularly benefit from LEV as they generally flap with high angles of attack, correlating to higher aerodynamic force production otherwise prone to stall (Ishihara et al., 2009). Once a flapping translating wing obeys the Kutta condition and the angle of attack increases, the flow on the upper surface separates from the wing and reattaches further down the chord (a straight line joining the leading edge and trailing edge) creating a low-pressure region (LEV) as shown in **Figure 1.3**. This occurs during pronation and the downstroke, and in some species additionally during supination and the upstroke (e.g., *Diptera* and *Lepidoptera*), which is thought to enhance lift force in the form of upward suction. As the LEV grows towards the trailing edge it usually becomes more unstable, eventually detaching from the wing that results in a drop in lift and increased drag. However, in insects the LEV is stabilised by the rotary motion of the wing, and is further shed at the end of each half-stroke (Ellington et al., 1996). To ensure lift throughout a wing beat, shedding of bound circulation and subsequent re-development of circulation must therefore occur during each half-stroke termed the Wagner effect (Biewener and Patek, 2018b). LEV works by providing a high lift coefficient or may just delay stall by allowing operation at higher angles of attack (Nabawy and Crowther, 2017). The lift (*L,* **Equation 1.2**) and drag (*D,* **Equation 1.3**) equation can be seen below, where air density ρ, speed U, surface area S, lift coefficient C_L or drag coefficient C_D are related. Both C_L and C_D can be calculated using computational fluid dynamics (CFD) or determined experimentally within a wind tunnel knowing wing area, velocity, and air density. Their typical relationship with angle of attack can be

seen in **Figure 1.4**. As the angle of attack increases, the C_L steadily increases and peaks when the angle of attack reaches 45°, the C_L then begins to drop > 45° as the C_D continues to increase and starts to plateau as airfoil begins to stall. The shape and strength of the LEV is also greatly influenced by *Re.* As *Re* increases in unsteady flow conditions, so does C_L, but profile power requirements increase. Whereas when *Re* decreases, boundary layers are more prone to detachment (Jones and Babinsky, 2010, Eldredge and Jones, 2019). When travelling long distances, using LEV as a primary lift generating mechanism would therefore be very expensive due to high drag. Desert locusts thus use more conventional mechanisms to travel up to hundreds of kilometres. Walker *et al.* (2009) described them to hold an almost constant angle of attack and linear twist distribution optimised for the best lift to drag ratio.

Equation 1.2 Lift equation

$$L = \frac{1}{2}\,\rho\,U^2\,S\,C_L$$

Equation 1.3 Drag equation

$$D = \frac{1}{2}\,\rho\,U^2\,S\,C_D$$

(II) Clap and fling was the first unsteady flow mechanism proposed by Weis-Fogh in 1973. Wings ‘clap’ together at the end of upstroke and ‘fling’ apart at the start of downstroke. As the wings peel apart leading edge first, air rushes into the low pressure ‘vacuum’ created between the wings. The effort required to re-accelerate the air therefore decreases as it joins the bound vortex, already around the wing starting to become established (Ellington and Lighthill, 1984a). (III) Meanwhile, pronation and supination around the spanwise axis is responsible for rotational lift. A positive angle of attack is maintained when translating to maintain the production of lift via LEV. The unsteady effects of this wing rotation are less well known at the extreme positive and negative angle of attacks to delay stall (Taylor, 2012). The effects are frequently described with the analogy of the Magnus effect on translating and rotating spheres (Walker, 2002). The boundary layer on the blunt surface contacts and pulls in surrounding fluid until eventually velocity on one side is higher than the other. If the flow velocity is higher on the top surface alike during a ball back spin, low pressure above the area pulls the sphere upwards (Dickinson et al., 1999). Dickinson *et al.* (1999) highlights the importance of the timing of rotation during steering manoeuvres. Verifying that if the wing flips early before reversing its direction (‘advanced rotation’) it produces the upward component of lift, and that if the wing flips late after direction reversion (‘delayed rotation’) a downward force is produced.

(IV) Lastly, wake recapture at stroke reversal is of particular importance in hovering and four winged insects where the hindwing is likely to encounter its own shed vorticity and re-intercept the shed vorticity of the forewing. Insects benefit from wing-wake interactions as the momentum of accelerated fluid shed

(induced velocity), interacts with the developing LEV on the wing of the next half stroke, decreasing the Wagner effect (Biewener and Patek, 2018b). Subtle time changes in wing rotation relative to translation in all four unsteady aerodynamic mechanisms aid asymmetric force production. This produces torques (force that tends to cause rotation) required for insects to perform their impressive range of flight manoeuvres.

Unsteady aerodynamic mechanisms continue to be discovered as Bomphrey et al. (2017) recently revealed a trailing edge vortex (TEV) and lift mediated rotational drag as additional lift mechanisms. These mechanisms remain exclusive to mosquitoes, possibly due to their slender high aspect ratio (AR, square of wingspan over wing area) wings, high wingbeat frequency (> 800 Hz versus ~ 200 Hz in *Drosophila* (Dickinson and Muijres, 2016)) and low stroke amplitudes (44 ^{o} in *Culex* mosquito (Bomphrey et al., 2017) versus 140 ^{o} in fruit fly (Fry et al., 2005)). TEV is described as a form of wake recapture during stroke reversal and differs from typical wake recapture as the wake first encounters the trailing edge. Meanwhile, rotational drag occurs at the end of each downstroke as stroke reversal begins. A concentrated negative pressure appears at the trailing edge as the wing rotates around the axis close to the leading edge, and strong forces normal to the posterior wing surface develop. Together they significantly reduce the requirement for lift generation acquired during the translation phase, critical in many flying animals.

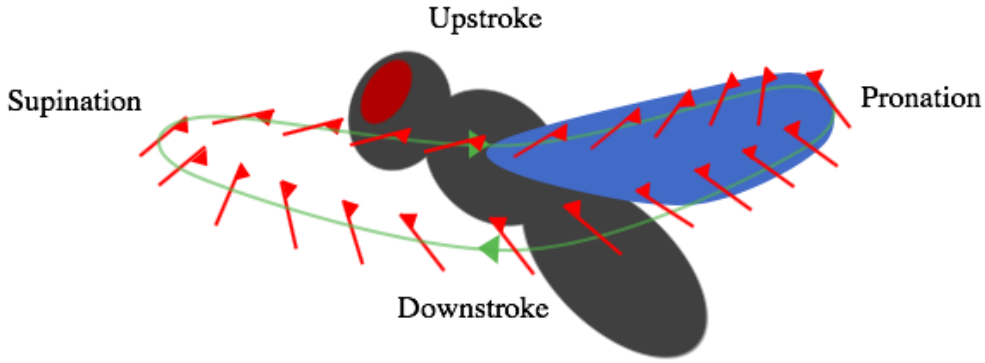

Figure 1.2 Insect wing kinematics

Following the wing path (green line) at the end of the upstroke, pronation of the wing (blue) occurs dorsally as the wing transitions to downstroke. At the end of downstroke, the wing supinates ventrally when transitioning to upstroke. Wing pitch (rotation around the wing's length) is illustrated by the direction of the red flag, and the red triangle at the wing's leading edge is on the wings morphologically dorsal side.

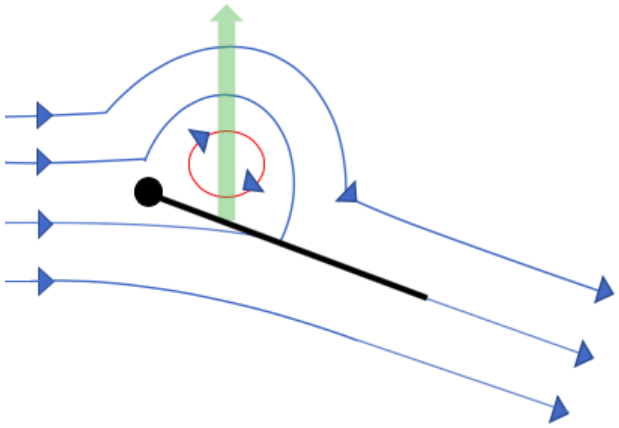

Figure 1.3 Leading edge vortex (LEV)

Oncoming flow, vorticity development and flow reattachment at the trailing edge (blue), low pressure region (red), insect wing with a high angle of attack (black) and lift (green arrow).

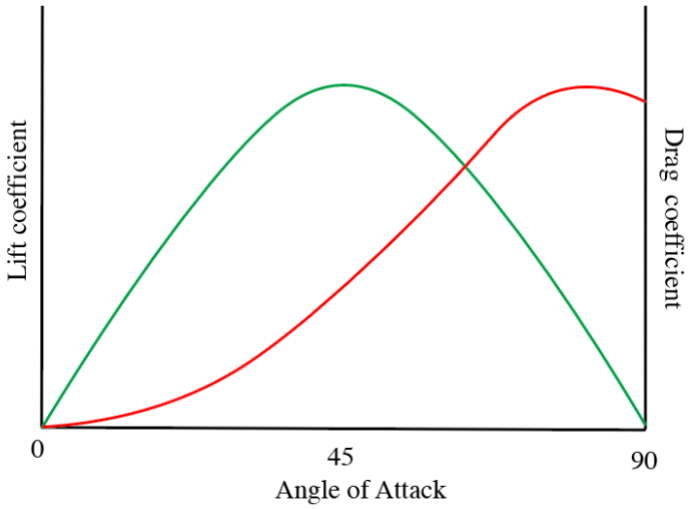

Figure 1.4 Lift coefficient (C_L)-angle of attack (green line) and drag coefficient (C_D)-angle of attack (red line) relationship

$\boldsymbol{C_L}$ increases, peaks when the angle of attack reaches 45° and then decreases > 45°. $\boldsymbol{C_D}$ steadily increases as the angle of attack increases and starts to plateau as the airfoil begins to stall.

1.4 Stable and Manoeuvring Flight

Returning to equilibrium once a manoeuvre has been performed, is vital when sustaining an intended flight path. However, it is more complex than it seems as the left- and right-wing operate symmetrically or asymmetrically to drive body rotation translation. Additional active (e.g., sensory feedback detailed in **Section 1.6**) and passive (e.g., body pitch and drag) mechanisms work in orchestra to improve efficiency of aerodynamic force production and flight stabilisation when flapping.

The classic behaviour of *Drosophila* performing stretches of straight flight and banked turns has been found to be like other flying animals (hawkmoths (Greeter and Hedrick, 2016), bats (Aldridge, 1987) and pigeons (Usherwood et al., 2011)), and remains relevant to helicopter analogies (Muijres et al., 2015). Banked turns are executed as follows, (I) the force vector perpendicular to the insects stroke plane is redirected via changes in wing stroke angle, deviation and wing pitch angle, causing the body to roll (as the outer wing generates more lift or inner wing has greater drag) and pitch up (compensating for drop in lift), (II) a counter-bank (counter-torque) is followed to arrest lateral body motion (sideslip) by making the force vector more vertical, (III) the body then undergoes yaw to its new direction and, finally (IV) aerodynamic force is generated symmetrically by increasing wingbeat frequency, stroke amplitude or deviation angle to accelerate, collectively increasing wing velocity (Dickinson and Muijres, 2016). Tammero and Dickinson (2002) observed a typical saccade in *Drosophila* to be ~ 90 º in under 100 ms (~ 20 wingbeats). Whereas Ristroph et al. (2013) perturbed the body pitch

of *Drosophila* by 20 º using a magnetic field over one wingbeat (4 ms). These insects then increased their stroke angle 12 ms post-perturbation and fully recovered by 60 ms (15 wingbeats) to pre-perturbation levels. Consistent with an escape banking manoeuvre where speed is prioritised over stability to get away from looming object, a visual to motor delay of 61 ± 21 ms and a ~ 20 ms (3 – 4 wingbeats) gap between an evasive bank and counter bank was reported in *Drosophila* (Muijres et al., 2014). Timescales for voluntary and involuntary flight saccades followed by stabilisation are therefore comparable, despite stabilisation from involuntary saccades requiring more directional control and input from sensory cues.

Insects have also been observed to perform pure yaw turns when hovering and foraging, even though slow in comparison to banked turns, and less favourable for insects employing LEVs as their primary lift generating mechanism (see below). Hovering is considered one of the most demanding forms of flight as all lift must be generated from the wings' own motion rather than air velocity (a u-shaped relationship between power requirements and air speed is typically seen). When hovering with LEV, overall flight efficiency significantly decreases as drag is high in line with the high angles of attack used when flapping. However, yaw turns is one example where passive stability alone or passive stability supplementing active means, works against unwanted body rotations. Fluid drag can substantially attenuate rotational velocity due to their small size. As the body yaws, velocity asymmetry between the wings even when beating symmetrically, also results in the outer wing generating a higher net torque to dampen rotation called flapping counter torque (FCT) (Hedrick et al., 2009, Karásek et al., 2018).

On the other hand, Dragonflies' long bodies due to lateral drag are just realigned parallel to incoming flow against fluctuations in yaw (Dudley, 2000c).

Increasing body drag (profile drag or parasitic drag) has been shown to increase stability and fine tune control e.g., via body deformation (Bustamante et al., 2022) and leg extension (Berthé and Lehmann, 2015). Several studies have zeroed in on abdomen deflection and has been shown to contribute to flight control and manoeuvrability in fruit flies (Zanker, 1988) and locusts (Dawson et al., 1997). Bustamante et al. (2022) restricted abdomen movement in hawkmoths and found them to perform poorer than controls, by tracking their flight paths whilst they stalked a moving flower and calculating path tortuosity (defined as the deviation of the flight path during treatment from the mean flight path or a straight flight path). Berthé and Lehmann (2015) described manoeuvring *Drosophila* hindleg extension to alter their moment of inertia (MOI) by a maximum of 6 % in all three body axis systems (yaw, pitch, and roll), suggesting only fine control against wing damage and atypical apparatus. This is significantly different to orchid bees flying at intermediate to high flight speeds (> 5.6 m/s induced high roll instability) that extend their hind legs (5.9 % of body weight) to increase total body drag by 30 % and increase their MOI by > 50 % (Combes and Dudley, 2009b). The position of an animal's centre of mass (COM) is a good indicator of its flight performance and is often centred about the wing hinge/halteres. As the COM is placed further backwards from the centre of pressure (point where lift and drag force are applied) of the wings, the body is more responsive to torques in the pitching plane that must then be offset by aerodynamically generated torques. Whereas a COM placed ahead of the centre of pressure enhances stability but reduces manoeuvrability (Ellington, 1984, Dudley, 2000b). Insects can also shift their

stroke average centre of pressure relative to their COM, to modify pitch torque via advancement or delay of wing rotations and distance flapped between wing rotations (Dickinson and Muijres, 2016).

Insects operate to minimise their reaction time and maximise the speed of which their kinematic output needs to change (response time). Their wingtip velocities move several orders higher than their body but remain as important rudders when flapping overall, thus highlighting that the isolation of wings during studies is good but should consider body alterations during flight as well.

1.5 Insect Muscle

Flight muscle contained within the thorax makes up a large proportion (up to 60 %) of an insect's body mass (Marden, 1989, Suarez, 2000, Buchwald and Dudley, 2010), and accounts for > 90 % of oxygen uptake during flight in honeybees (Niven and Scharlemann, 2005, Greenwalt, 1962, Rothe and Nachtigall, 1989). It is therefore widely accepted that the increase in metabolic rate (energy used per unit time) calculated during flight from rest is assumed to be entirely due to muscle activity, as other processes, even when combined such as protein synthesis and digestion become negligible (Weibel, 2002, Hulbert and Else, 2000).

Insect flight muscle has been categorised into two main groups: large power muscle involved in providing power indirectly to the wings as they deform the thorax, and small steering muscle directly involved in steering the wings at the wing hinge made up of multiple sclerites (sclerotised 'plates' of cuticle). In addition to this, power muscle may be asynchronous (e.g., in *Diptera*) meaning that they can contract multiple times with a single activation signal or synchronous (in lower species e.g., dragonflies , locusts and moths), meaning that can only contract in synchrony with afferent signals (Biewener and Patek, 2018b). While steering muscle is only synchronous to encourage sensitivity to neuronal input and control of kinematics. A combination of cytological differences enables these different responses to neuronal input, namely: (I) mitochondria and (II) sarcoplasmic

reticulum (SR) concentration, and (III) neurological innervation summarised in **Table 1.1.**

(I) During aerobic respiration mitochondria synthesises adenosine triphosphate (ATP), the universal currency of chemical energy. Availability of this molecule is an important rate limiting step in the cycling of myosin-actin cross bridges during contraction. Mitochondria concentration in asynchronous muscle is therefore high within their large volume of myofibrils (the contractile unit of muscle). For instance, mitochondria occupies 53 % of asynchronous muscle cell volume in bees (Iwamoto, 2011, Katti et al., 2022) versus just 23.5 ± 2.1 % (mean ± SEM) in locust synchronous fibres (Josephson et al., 2000a). (II) The SR acts as a Ca^{2+} reservoir vital to muscle activation (Ca^{2+} release) and relaxation (Ca^{2+} reuptake). SRs envelope myofibrils sparsely in asynchronous muscle (volume density 2 - 3 % in cicadas (Syme and Josephson, 2002, Gau et al., 2023, Wan et al., 2013)) allowing them to pack tighter together, but extensively in synchronous muscle (9.6 ± 0.5 % in locust synchronous fibres (Josephson et al., 2000a)). In extreme cases, to increase contraction frequency SR volume may undergo hypertrophy, surpassing the volume of neighbouring myofibrils (Josephson and Young, 1985). However, hypertrophy of this organelle increases its surface area and thus, decreases efficiency (total mechanical power: chemical input) by enabling a larger number of ATP-dependent Ca^{2+} membrane pumps to occupy its surface liable for up to 50 % of overall muscle activation costs (Josephson et al., 2001). (III) Finally, each power muscle is innervated by multiple motor neurons unlike steering muscles that are innervated by a single motor neuron with a large diameter and extensive terminal branching to amplify the speed of depolarisation

and modulate power (Ikeda and Koenig, 1988, King and Tanouye, 1983, Trimarchi and Schneiderman, 1994).

In summary, synchronous and asynchronous muscle represent the extremes of muscle design, trading off absolute power and fine control respectfully whilst being constrained by myofibrillar volume and allocation of this internal space. Synchronous muscle as steering muscle enables subtle but high-order changes to the mechanical properties of the wing hinge. Whereas synchronous muscle as power muscle limits wingbeat frequency, but may still drive fast contractions (but still lower than asynchronous) if cytologically specialised with greater control but at reduced powers. Lastly, asynchronous muscle as power muscle can operate at higher frequencies, generate higher powers and has been said to be more efficient than the latter (Josephson et al., 2001). They provide a baseline wingbeat that steering muscle then modulates.

Table 1.1 Cytological differences between asynchronous and synchronous flight muscle

Muscle Property	Asynchronous	Synchronous	Reference
Mitochondria content /ATP	High volume (++)	High volume (+)	(Chapman et al., 2013, Conley and Lindstedt, 2002, Katti et al., 2022)
SR/Ca^{2+}	Low volume	Relatively high volume	(Bullard et al., 2006, Chapman et al., 2013, Josephson and Young, 1985)
Motor Neurons	Each is innervated by multiple motor neurons	In steering muscles, each is innervated by a single motor neuron with a large diameter and extensive terminal branching. Otherwise in indirect, synchronous power muscle it is like asynchronous innervation	(Ikeda and Koenig, 1988, King and Tanouye, 1983, Trimarchi and Schneiderman, 1994)

1.5.1 Synchronous Muscle

Like mammalian skeletal muscle, synchronous muscle contracts in synchrony with neuron innervation (1:1). The function of synchronous steering muscle is to simultaneously attenuate and directly regulate the mechanical output of the substantially larger power muscles via changing the shape of the wing hinge (made up of multiple sclerites) as the wing itself is non-muscular (Miyan et al., 1985, Walker et al., 2014) (**Figure 1.5**). The dexterity of steering muscle when controlling the wing hinge and the resultant wing kinematics, is achieved by each muscle being innervated by a single motor neuron. Their large abundance amongst all flying insects, in comparison to the power muscles may also contribute to this. The blowfly for example, possess four pairs of asynchronous power muscle and 18 pairs of steering muscle that enable the wing hinge to move with three degrees of freedom (Dickinson and Tu, 1997, Mordoch et al., 2024). Moreover, synchronous muscle volume as previously mentioned, is largely occupied by mitochondria (~ 40 % in *Odonata* (Chapman et al., 2013)) and relatively high amounts of SR (typically up to 15 % muscle volume) in comparison to asynchronous muscle (SR 2 - 3 % (Syme and Josephson, 2002)), that enables the muscle to quickly react to cycles of excitation and relaxation (Chapman et al., 2013). For this reason, synchronous muscle has also been seen to operate impressively within the ranges of asynchronous muscle just over 500 Hz but at low power for cicada tymbal song production (Josephson and Young, 1985, Bennet-Clark and Daws, 1999).

Steering muscles can be further categorised according to the sclerites on to which they insert: the basalars (B1, B2, B3), first axillaries/pterales I (I1, I2), third axillaries/pterales III (III1, III2, III3, III4 but III2 missing in *Drosophila*) and fourth axillaries/posterior notal wing process (Hg1, Hg2, Hg3, Hg4) illustrated in **Figure 1.6** (Lindsay et al., 2017). Together they are responsible for the series of manoeuvres the animal can perform by controlling upstroke, downstroke, wing amplitude, pronation and supination (Wisser and Nachtigall, 1984, Hedenström, 2014). It is therefore important to remember that, when studying the individual steering muscles in isolation that they may have multiple functions and or particular roles in a group, thus making investigation of these muscles even more difficult. It is still unclear how these steering muscles carry out their function precisely, whilst only making up < 3 % of flight muscle mass (Walker et al., 2014). But it has been proposed that these muscles work as shock absorbers by performing negative work (absorbing work) when appropriate, and only passing on the kinetic energy to the wing hinge required for the desired flight manoeuvre. A study using a new time-resolved microtomography technique supported this, and further revealed an additional mode of oscillation for asymmetric power output, and some of the specific muscles that use this mode within blowflies. Some tendons buckle under compressive loading assisting high amplitude movements of the wing hinge (I1) whilst others operate by directly absorbing excess mechanical energy (B1) from the asynchronous muscle (Walker et al., 2014).

Some research has also been done to correlate neuromuscular spike rates, firing phase shifts and their combinatory kinematic and aerodynamic effect (Balint and

Dickinson, 2001, Balint and Dickinson, 2004). Tu and Dickinson (1996) were the first to uncover B1 and B2 steering activity in *Calliphora* where B1 fired with every wingbeat during pronation (upstroke to downstroke) to maintain a large stroke amplitude. Meanwhile, B2 only fired when stroke amplitude was already high and as a turning optomotor response. Supporting this behaviour, B1 on the contralateral side of the turn (outside) was also reported to advance its phase firing by 1 – 2 ms mid-upstroke, to increase protraction and stroke amplitude on the following downstroke (Dickinson and Tu, 1997, Heide and Götz, 1996). Conversely, B3 fires with every wingbeat after supination (downstroke to upstroke) and so possibly behaves like B1 but determines backward amplitude although is yet to be confirmed (Dixon et al., unpublished). Since then, III1 has been revealed to maybe work in conjunction with B2 to increase stroke amplitude and facilitate wing retraction, all basalare muscles and III2 - 4 define maximum forward amplitude, and I1 and Hg3 contraction decrease stroke amplitude (Balint and Dickinson, 2001). The function of outstanding Hg's remains a mystery but their organisation in *Drosophila* was more recently reported in Lindsay et al. (2017) via *in vivo* calcium imaging but at low resolution. The tegropleural, pleurosternal and tegrotrochanter are additional synchronous muscles near the wing hinge that are likely to further alter the resonant properties of the thorax (stiffness) and thus wingbeat frequency. Steering muscles thereby continue to challenge our ability to scrutinise their function, due to their small size, organisation, combinatory effect, and large amounts of compressed data in a small number of electromyography (EMG) spikes.

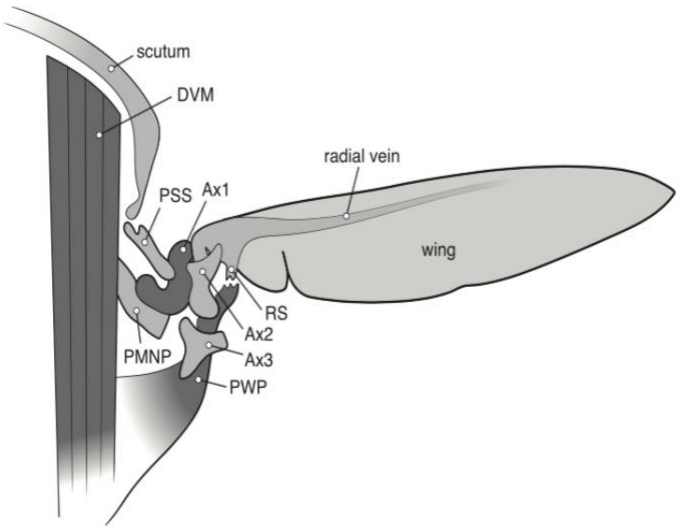

Figure 1.5 Illustration of the wing hinge

Axillary sclerites (Ax1 (pterales I), Ax2 (pterales III), Ax3 (posterior notal wing process)), pleural wing process (PWP), radical stop (RS), dorsal ventral muscle (DVM). Diagram amended from (Hedenström, 2014).

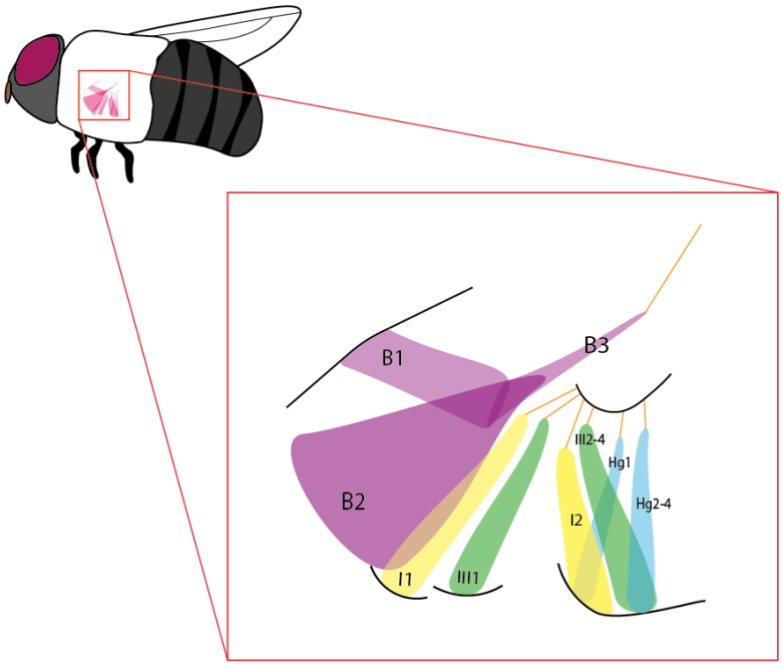

Figure 1.6 Parasagittal cross section of a general fly and its synchronous steering muscles

Steering muscle groups based on the sclerites to which they insert: basalars (purple), first axillaries (yellow), third axillaries (green) and fourth axillaries (blue).

1.5.2 Asynchronous Muscle

Asynchronous muscle is a key adaptation driven to achieve energetically efficient muscle, and has been suggested to have evolved independently up to 7 - 10 times from extant insect taxa to now be present amongst the orders: *Coleoptera*, *Hymenoptera*, *Diptera* and *Hempitera* (Misof et al., 2014, Syme and Josephson, 2002). This adaptation has allowed some insects to operate at wingbeat frequencies between 200 to 1000 Hz and to achieve a greater power output, due to their reduced volumes in SR enabling relatively higher myofibril volumes

(Biewener and Patek, 2018a). The asynchronous muscle of *Cotinus mutabilis* (beetle) for example averages 127 Wkg^{-1}, with a maximum value of 200 WKg^{-1} at 94 Hz (Josephson et al., 2000b). This differs greatly to the synchronous flight muscle of *Manduca sexta* (tobacco hawkmoth) with powers previously measured up to 90 Wkg^{-1} between 28 - 32 Hz (Biewener and Patek, 2018a, Stevenson and Josephson, 1990).

The dorsal longitudinal muscles (DLM) are the first power muscles encountered when making a dorsal ventral cut of the thorax (**Figure 1.7A**). During flight the DLM is responsible for wing depression during downstroke. As they contract, it shortens, compressing the thorax longitudinally and lengthening it dorsoventrally (**Figure 1.7B**). This then lengthens the dorsoventral power muscles (DVMs) situated behind the DLM triggering them to contract. The thorax then shortens dorsoventrally and expands longitudinally and laterally to elevate the wings during upstroke (**Figure 1.7B**) (Wisser and Nachtigall, 1984, Cao and Jin, 2020). Stretching the DLM then causes them to quickly contract again, and the cycle continues until stimulation ceases.

Several underlying cytological differences must be present to facilitate the response described above often referred to as delayed stretch activation-shortening deactivation. Fast contractions are possible as a single impulse here allows for multiple muscle twitches as sufficient amounts of calcium are maintained post-stimulation within depolarised motor neurons (Biewener and Patek, 2018b). Asynchronous muscle lacks neurological control so that

contractile proteins can dominate internal space. Mitochondria are large organelles that occupy asynchronous muscle volume at high concentrations. This is to supply ATP at a high rate, to match the high rate of utilisation, and to increase muscle stamina before subject to fatigue. Meanwhile low SR concentration allows for more room for sarcomeres to maximise power output potential per volume (mass specific power), and contributes to maintaining sarcoplasmic Ca^{2+} concentration, that facilitates the antagonist behaviour observed between DLM and DVM groups despite receiving slow neural input. Loya et al. (2022) looked at stretch activation and shortening deactivation independently in *Drosophila* and *Lethocerus* (giant water bug). During shortening deactivation tension decreased when normalised against isometric tension by 118 % and 97 % respectfully. Denoting that shortening deactivation allows muscle to quickly relax and minimise their resistance against repetitive lengthening (Loya et al., 2022). Casey et al. (2023) further revealed that thorax anisotropic elasticity may assist this as stiffness was ~ 3.8 times greater than in synchronous insects dorsoventrally.

Although there has been some progress over the years the molecular mechanism of stretch activation-shortening deactivation remains unclear. The Tn complex of some asynchronous muscle (e.g., in *Drosophila* and *Anopheles*) was found to have an additional Troponin H (TnH33 and TnH34) subunit and a TnC isoform (F1) with a single high affinity binding Ca^{2+} site at the C-terminal domain, resulting in a higher affinity for Ca^{2+} at low concentrations vital for stretch activation (Peckham et al., 1992, Qiu et al., 2003, Agianian et al., 2004). Perz-Edwards (2011) also explored the idea of myosin-troponin bridges as agents of mechanical signal transduction using x-ray diffraction. When stretched myosin-troponin

bridges seemed to tug tropomyosin away from actin that block the myosin binding sites and lead to subsequent force production even at low concentrations of Ca^{2+} (Linari et al., 2004). Evidence of sarcomere lattice compression during stretch (2.2 % compression from rest) that decreased the distance between myosin and actin by ~ 0.4 nm from controls, was also concluded as a passive response to stretch theoretically decreasing the time for cross bridges to form, cycle and reset (Perz-Edwards et al., 2011). The force-length relationship of this coupled event can be seen in **Figure 1.8** where force increases as the muscle is stretched (stretch activation) then decreases (shortening deactivation) as the muscle shortens quickly due to force-velocity effects. Similar events can be seen in mammalian cardiac muscle but is less pronounced and to a lower extent (Vemuri et al., 1999).

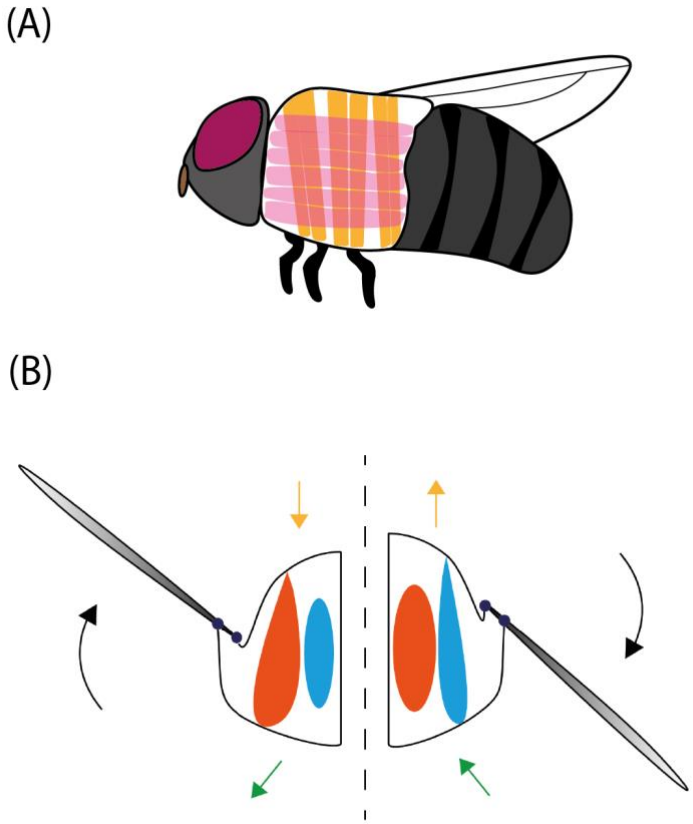

Figure 1.7 Organisation of indirect power muscle and its contraction outcomes

(A) Sagittal cross section of the thorax and organisation of its asynchronous (indirect power) flight muscles. Dorsal longitudinal muscle (DLM, pink), dorsoventral muscle (DVM, orange). (B) Transverse section of the thorax. (B left side) Upstroke occurs as the DVM contracts (red) and DLM relaxes (blue). (B right side) Downstroke occurs as the DLM contracts (red), and DVM relaxes (blue). For both (B left and right side) the yellow and green arrows indicate the direction of thorax deformation, black arrows show the direction of wing movement and black dots are the wing hinge.

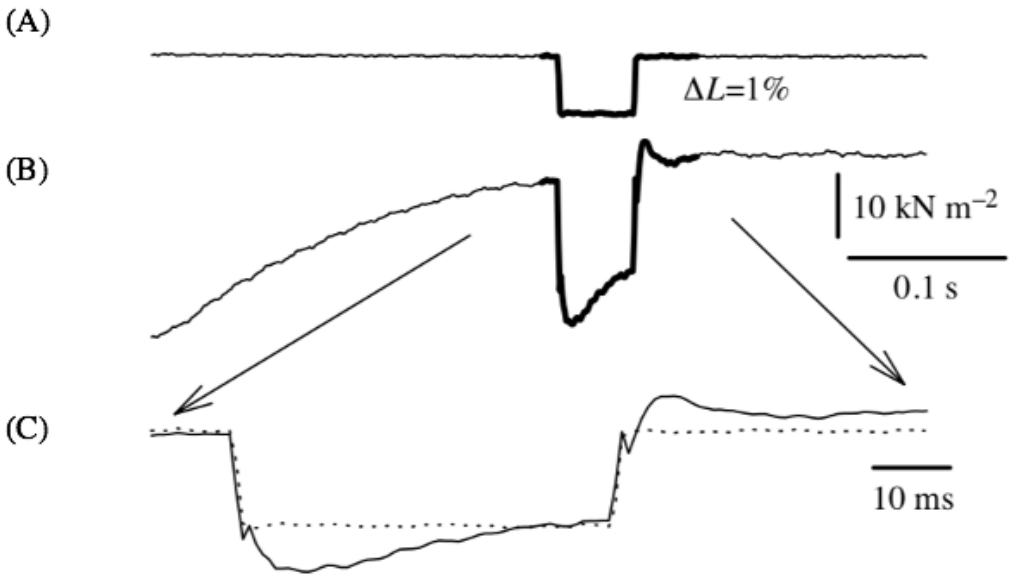

Figure 1.8 Force production during shortening deactivation and stretch activation following changes in length

(A) Step down length change (Δ*L*), (B) subsequent force production during isometric tetanus during the step-down length change, and (C) the bold regions of the length (dotted line) and force (plain line) trace in A and B enlarged and superimposed. After the asynchronous muscle is shortened force continues to decrease (shortening deactivation) and then steadily increases before returning to its resting length. As the muscle is returned to its resting length force increases and continues to increase (stretch activation) before coming to a plateau. Diagram from (Josephson and Ellington, 1997).

1.6 Sensory Input and Vision

To perceive their environment, insects have developed competent nervous systems and various sensors that vary in distribution and energy expenditure to guide their motor output. These qualities include widespread exteroceptors that deduce the environment (e.g., hair-like structures that project out from cuticle), and proprioceptors that monitor the body's position and movement (e.g., campaniform sensilla embedded in cuticle (Gnatzy et al., 1987) and halteres (Dickinson, 1999, Biewener and Patek, 2018c)). The abundance of hair-like projections that span their entire exoskeleton and their wings, have been shown to provide directional information when displaced by a physical object or by air current (Casas and Dangles, 2009, Barth and Holler, 1999, Steinmann et al., 2006). Campaniform sensilla are dome-shaped mechanoreceptors that respond to pressure and surrounding cuticular strain from underlying muscle activity (Biewener and Patek, 2018c). Proprioceptors thereby populate joint/muscle insertion (apodemes) points where movement occurs predominantly. In insect wings, proprioceptors provide sensory feedback on aerodynamic loading by being cleverly located at cross-veins in both deformable and rigid zones (Dickinson, 1990). Whereas, halteres are reduced hindwing, club-shaped organs located on the lateral surface of the thorax near the wing hinge, that detects body rotation (angular velocity) via Coriolis (inertial) forces as it moves linearly back and forth (Dickinson, 1999).

The importance of insect vision is emphasised by their large eye size (heavy) and dedicated brain regions. In dragonflies, the protocerebrum responsible for the

vast majority of visual processing makes up to 80 % of total brain volume (Dudley, 2000c). To collect this visual information, insects have compound eyes made up of repeating optical units called ommatidia. A single ommatidium is cylindrical and contains central photoreceptors (R-cells or retinula cells), surrounding pigment cells and lens secreting cells as organised in **Figure 1.9A and B** (Pichaud and Casares, 2022). Rhabdomeres are organelles within R-cells that act as light guides, composed of heavily folded apical membranes (microvilli) containing photopigment rhodopsin (Buschbeck and Friedrich, 2008). R-cells may contain one rhabdomere or more adjacent to one another, collectively known as rhabdoms with a central matrix. In true flies (*Diptera*), rhabdomeres are independent (open rhabdom), enabling spatial independency in a different space implying increased image sharpness and sensitivity (Pichaud and Casares, 2022, Land, 1997, Zelhof et al., 2006).

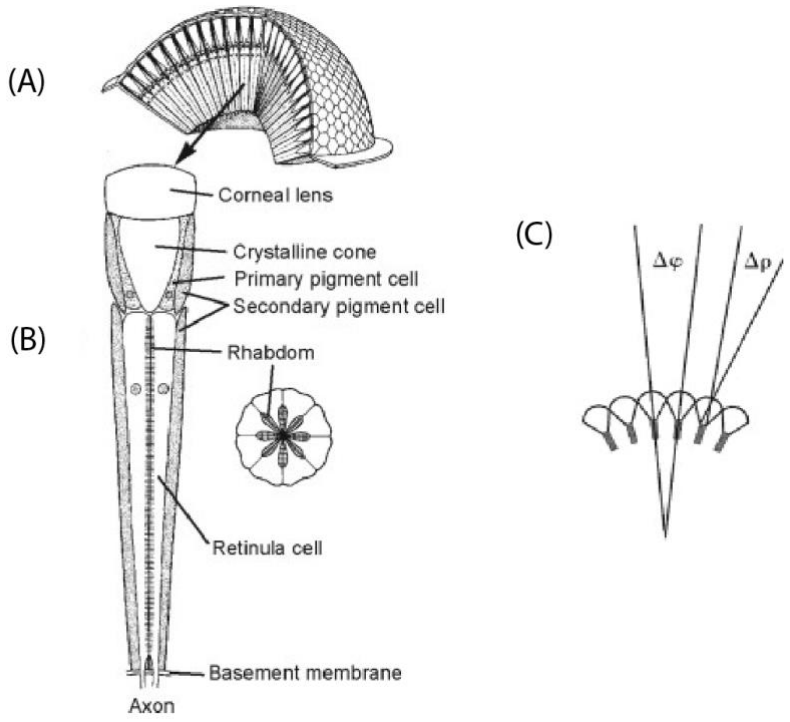

Figure 1.9 The compound eye, arrangement and structure of ommatidium, and defining interommatidial angle

(A) Compound eye, (B) cross section of an ommatidium and (C) the definition of interommatidial angle ($\Delta\varphi$) and rhabdom acceptance angle ($\Delta\rho$) (Land and Nilsson, 2002, Gullan and Cranston, 2004).

As a rule of thumb, the larger the compound eye the better the insect's vision because small eyes are limited by diffraction. However, overall eye size, curvature, focal length and rhabdomere width are variable across species and is responsible for the trade-off between spatial resolution and sensitivity (Gonzalez-Bellido et al., 2011). A compound eye may contain tens to thousands of ommatidia with varied arrangements (Beersma et al., 1977, Döring and Spaethe, 2009, Mound, 2009, Streinzer et al., 2013) and so, specialised bright (increased sensitivity) and acute (increased resolution) zones in some insects. The number and size of ommatidia determines the overall size and curvature of the eye, and thus greatly influences spatial resolution i.e., the larger the ommatidia lens the

flatter the eye will be. At this level the optical axis and interommatidial angle (angle between adjacent ommatidia's optical axis) is also determined (**Figure 1.9C**). The smaller the interommatidial angle the greater the sampling resolution but lower the sensitivity will be, as less light is collected and vice versa for large ommatidia if eye area remains constant. Gonzalez-Bellido et al. (2011) measured and compared the interommatidial angle of similar body and eye sized *Drosophila* (smallest 4.5 degrees) against *Coenosia* (killer fly, smallest 2.2 degrees) at various eye regions and found *Coenosia* to have 3 - 4-fold greater spatial resolution than *Drosophila* in line with their predatory lifestyle. This was only possible with their large number of ommatidia, narrow rhabdomeres and interommatidial angles, which meant reduced pixel size, reduced crosstalk between photoreceptors, and faster phototransduction reactions. *Coenosia* also had larger fontal lenses denoting a specialised acute or bright zone.

Other eye specialisations include some insects having close to 360-degree vision and varied colour perception. For instance, stalk-eyed flies as their names suggest, have eyes that protrude significantly from their heads on up to 1 cm stalks. Each eye has been found to have a 235 degree field of view in the horizontal plane and more than 70 % of ommatidia from each eye to be binocular (equating to 135 degree binocular overlap) (Burkhardt and de la Motte, 1983). Some insects can see extensively in colour, which is primarily determined by rhodopsin wavelength sensitivity (categorised as short-, middle- or long-wavelength). Kooi et al. (2021) usefully summarised photoreceptor spectral sensitivity for 221 species in 13 insect orders (Kooi et al., 2021). Studying honeybee colour and UV vision has also gained traction due to their wavelength specific behaviour when foraging, and using landmarks to locate their home even

in dim light (Vijayan et al., 2023, Giurfa et al., 1995). Lastly, some species e.g., dragonflies and grasshoppers have triplet ancient supplementary eyes called ocelli located on their dorsal head cuticle. They are believed to provide relatively poor, under focused data as single chambered eyes to help detect the horizon with good contrast (Simmons, 1982).

Wide-field motion sensitive afferent neurons called lobular plate tangential cells (LPTCs) are then responsible for relaying visual information to the lobular plate within the optic lobe (also consists of neuropiles, the lamina, medulla and lobular) for processing (Boergens et al., 2018). Here, pre-synaptic neurons T4 and T5 each have four subtypes that run parallel ON (luminance increase) and OFF (luminance decrease) pathways, encoding local motion in each cardinal direction (up, down, back to front, front to back) (Wei et al., 2020, Maisak et al., 2013). How the lobular plate processes this information is remains largely unknown due to its minute size, but elementary motion detection (how their neural network may calculate motion) algorithms have been modelled from behavioural experiments and the output of large LPTCs (Maisak et al., 2013).

External factors must also be considered such as ambient lighting required by receptors for a reliable signal and the motion of the presenting object/surroundings (a fast object is more likely to appear blurry). To investigate an insects optomotor response its critical flicker fusion frequency (CFF) must be determined. Flicker fusion frequency is frequency of which a flickering light can be perceived as continuous and is dependent on the individual, stimulus size, position and distance, ambient lighting and wavelength (Mankowska et al., 2021).

CFF values reported in literature by photoreceptor measurements are 240 Hz (Autrum and Hoffmann, 1960), 200 Hz (Cosens and LeBlanc, 1980) and 130 Hz (Meyer-Rochow, 1981) respectfully in the *Calliphora*, *Drosophila* and *Bombus*. Although recent behavioural studies have solved for significantly lower CFF values as low as 60 Hz, 70 Hz and 40 Hz for the same species respectfully (Dixon et al., unpublished).

1.7 Research Aims of this Thesis

Chapter 1 features fundamental topics related to the experimental chapters of this thesis. Flying insects must simultaneously generate and control aerodynamic forces to steer, whilst also correcting for instability from both extrinsic (e.g., a small gust of wind or ambient temperature change) and intrinsic (e.g., abnormal physiology) factors (**Section 1.3 to 1.6**). However, to accurately estimate their aerodynamic force production, researchers require in-depth kinematics that is difficult to capture in small bodied and high wingbeat frequency insects (**Section 1.3.2 and 6.3.5**). Detailed kinematics are also required to inform bio-inspired MAV development as described in **Section 1.1,** when aiming to achieve similar flight dexterity. The points raised above will be further addressed in the upcoming chapters. More specifically: efforts to improve and ease the kinematics acquisition of insects during free-flight in **Chapter 2**, reporting high-precision kinematics for future aerodynamic modelling and steps taken to correct abnormal physiology (leg loss) in **Chapter 3**, the effect of varying ambient temperature in **Chapter 4,** and kinematics of extreme flight manoeuvres for future MAV development in **Chapter 5**.

1.7.1 General Methods: A New and Flexible Insect Free-flight Lab

Insects perform incredible flight manoeuvres, and how they achieve this is something we have yet to learn a lot about. To gain insight, experimental setups

must therefore be able to acquire footage of appropriate spatiotemporal resolution (determined by insect wingbeat frequency, size and behaviour) and duration of insects during free-flight. Existing setups are challenged for example, by too few camera views (e.g., four cameras (Maya et al., 2023)) to avoid wing occlusions (e.g., by the insect's own legs), high computational power demands owed to trade-offs between operating equipment (e.g., frame rate and picture resolution), and the capacity to sample the kinematics of interspecific subjects without rebuilding (e.g., a larger insect needs a larger chamber to encourage natural flight and cameras positioned further away). Once data collection has been completed, downstream data processing is also often complex and or labour intensive, which further differentiates and complicates the reporting of kinematic parameters in literature (Provini et al., 2023).

In this methods chapter, I thus described a new and flexible free-flight laboratory that will be used to report high-precision kinematics of the insect species featured in my experimental chapters. The design of this setup aimed to address the challenges faced by existing setups mentioned above, to capture subtle changes in kinematics in unprecedented resolution (including wing torsion and bending) using ten high-speed cameras. To process footage, a comprehensive voxel carving package that was used to calculate wing and body kinematics quickly and automatically was also described. Thus, enabling the generation of large datasets with the same kinematic definitions (e.g., for deviation angle and axis systems, **Section 2.2.4**) within the research projects of this thesis.

1.7.2 High-precision Wing and Leg Kinematics of *Anopheles gambiae* during free-flight

Mosquitoes are morphologically and aerodynamically interesting with their narrow wings, high wingbeat frequencies (> 800 Hz), and long narrow limbs that spread once airborne (Somers et al., 2022, Aldersley and Cator, 2019). Recent work by Bomphrey et al. (2017) revealed that mosquitoes perform TEV and rotational drag during the rotational phase of flapping, but how they utilise these lift generating mechanisms when manoeuvring is still unknown (**Section 1.3.2**).

The aim of this chapter was to therefore generate a large database of high-precision *Anopheles* mosquito body and wing kinematics whilst encouraging flight manoeuvres over a range of ambient temperatures. It was also aimed to provide in-depth leg kinematics of intact subjects, and of those that had experienced leg loss using a complementary leg tracker MATLAB script for comparison. Thirdly, by supplementary hanging experiments to determine the COM position of *Anopheles,* the relationship between the body's MOI and total leg MOI could be assessed to provide insight on the importance of non-wing appendages on flight control and stability.

1.7.3 Kinematics of *Anopheles gambiae* with varying temperature

Mosquitoes thrive in warm climates and in the past, have been shown to increase their wingbeat frequency with ambient temperature (Villarreal et al., 2017). However, further investigation of the effect of temperature on time-varying parameters such as stroke angle and wing pitch needed to sufficiently describe the 3D motion of a wingbeat cannot be simply regressed.

Using the same dataset described in the previous experimental chapter, it was therefore first aimed to identify the relationships between varying ambient temperature and summary parameters such as wingbeat frequency, and the body kinematics (e.g., body pitch) of *Anopheles*. Fourier fitting (to summarise time-varying data) and principal component analysis (to create a set of independent parameters, and identify which were most important to describe data variation) of this dataset could then be used to create descriptor wingbeats that enable testing of the effect of temperature. By further validating the results of these data compression techniques via kinematic reconstruction, changes in other summary parameters such as stroke plane and stroke amplitude may also be predicted.

1.7.4 Body Kinematics and Operating Time Scales of *Coenosia attenuata*

Coenosia attenuata (killer fly) are small, sit and wait ambush predators that hunt prey of comparable body size (~ 4 mm (Fabian et al., 2018)) mid-air. During pursuit, this species has been reported to perform extremely high dive accelerations to intercept prey, whilst employing close range proportional navigation (the prey's location is monitored to maintain a constant line of sight (LoS) between the two) to minimise flight duration and distance (Rossoni et al., 2021).

Due to their flight agility and small size that make them ideal candidates for the high-speed camera experimental setup, it was therefore aimed to encourage pursuit behaviours/extreme manoeuvres in *Coenosia* by presenting two different configurations of artificial prey (but both black beads) to starved subjects. By thresholding sequences (e.g., by the minimum distance achieved between the black bead and fly), then calculating the rotation rate of *Coenosia* and LoS rotation rate between the artificial prey and *Coenosia* in footage, proportional navigation could be verified. Meanwhile, by reporting the wing kinematics, body kinematics (e.g., angular rate and angular acceleration) and the operating time scales observed, enable the comparison to other predatory insects and escaping insects of similar body size.

Chapter 2

General Methods: A New and Flexible Insect Free-flight Lab

2.1 Introduction

Insect flight involves incredibly fast rotations, and translations of their wing appendages. Researchers therefore require high-speed imaging techniques in order to perceive their movements, and typically from two or more camera views to obtain their 3-dimensional (3D) kinematics with photogrammetry. This digitisation technique was initially developed to make architectural measurements in the 1800s, and uses triangulation where 2-dimensional (2D) images are mathematically intersected from common landmarks (lines of sight) to calculate 3D points (Aber et al., 2010, Matthews, 2008, Albertz, 2001). Since then, it has been made clear that photogrammetry is a valuable tool that has been adapted to extract detail on flying insects as well as other dynamic organisms. For instance, the 3D kinematics of tethered locusts and free flying hoverflies have been reported to explore wing surface topography (Walker et al., 2009), fruit flies to capture the kinematics of rapid manoeuvres for a dynamically scaled robotic wing (Fry et al., 2003), western flower thrips for flying and landing behaviour for trap design (Lopez-Reyes et al., 2023) and many more. Although, it is important to note that the standard of kinematic data amongst literature may vary significantly in resolution due to several experimental and analytical factors that come into play (see below).

When measuring the 3D kinematics of insect flight, challenges typically arise from the experimental setup, which then largely determines sequence quality and influences downstream data analysis. High-speed cameras are expensive, and more than one is necessary for multiple camera views to minimise wing occlusions from other body parts (e.g., legs or elytra) or the environment. Maya et al. (2023) recently explored and discussed pose estimation or wing visibility of four experimental setups with three or four cameras configurations. A hybrid camera configuration with three pyramidal orthogonal cameras and one vertical camera provided the highest *Drosophila* flight model visibility. However, it was admitted that the setup would experience difficulty with long legged species such as mosquitoes that require more camera views (Maya et al., 2023). Bomphrey et al. (2017) resolved this issue with eight camera views to survey the free-flight kinematics of *Culex* mosquitoes but with small recording resolution (384 $\times$ 352 pixels) and small sample size (N = 12 to 15 individuals and N = 425 wingbeats over 15 sequences). Experimental setups are thus highly personalised for the level of kinematic detail required to answer the question in mind and the species of interest, as insects are diverse in body size and behaviour. To obtain footage of similar spatial and temporal resolution, and duration of bumblebees (*Bombus terrestris* workers body length ~ 14 - 18 mm, wing length ~ 9 - 13 mm, wingbeat frequency 150 - 200 Hz (Kardum Hjort et al., 2023, Josephson and Ellington, 1997, Mountcastle and Combes, 2013)) and biting midges (*Culicoides spp*. body length 2 – 3 mm, wing length 0.9 - 1.3 mm, wingbeat frequency > 1000 Hz (Blackwell, 2008, Morag et al., 2013, Belton, 1986) for example, requires significant changes in the size of the flight chamber to encourage natural flight, camera proximity and camera settings (e.g. frame rate).

Once high-speed footage had been acquired, data processing/tracking methods also differed substantially amongst literature. Sequences are often short as tracking is labour intensive if manually done frame by frame (Lyu et al., 2020) or is likely to be computationally expensive if automated using landmark tracking on large insects (Walker et al., 2008), model based optimisation (a 3D model is constructed and projected onto the image planes) (Muijres et al., 2017, Fontaine et al., 2009) or visual hull reconstruction (also called voxel carving) where common pixels that form the silhouettes of the insect in all camera views are retained in the final 3D shape of volumetric pixels (voxel) (Perez et al., 2012, Walker et al., 2012). Further diversion arises from the varying definitions of kinematic parameters and axis systems that make it difficult to compare kinematics between literature (Provini et al., 2023). Ribak et al. (2017) and Bomphrey et al. (2017) for instance, describe similar wing kinematic parameters with names, angle of incidence and wing pitch angle (Ribak et al., 2017, Bomphrey et al., 2017).

The aim of this chapter thus addresses the issues forementioned with current experimental setups (i.e., few camera views, quality of footage, experimental setup flexibly and laborious data processing pathways), by describing a new insect free-flight lab and pipeline to extract high-precision 3D kinematics. This setup was used throughout the experimental chapters of my thesis, but with species dependent adjustments that will be detailed later to avoid repetition where the same framework is used. Footage obtained was of unprecedented resolution using ten high-speed cameras to maximise coverage of the insect. High-speed cameras and additional components such as additional stereo trigger cameras and far-red backlights were able to be easily repositioned, and optically

clear free-flight arena/chamber replaced for a variety of insect species. High quality footage was then run through a quick and completely automated voxel-carving software package, to calculate high-precision 3D body, wing (including wing torsion and bending) and leg (*Anopheles* only, **Section 3.2.2**) kinematics. With this setup, I started creating a large database and outlined a new standard of insect flight 3D kinematics that will better our understanding of this diverse class. Kinematics extracted here may for example be fed into studies of insect flight control and aerodynamic modelling. Finally, in this chapter I define kinematic parameters and their axis systems to be used throughout this thesis. Utilising the same experimental framework, data processing pathways, and definitions of kinematic parameter avoids differences owed to inter-laboratory differences, and thus minimising uncertainty when comparing across different insect species.

2.2 Insect Free-flight Lab

In this section, the general setup of the insect free-flight lab pictured in **Figures 2.1 and 2.2** is described. The foundations of these experiments were designed and built by Simon Walker (S.W, University of Leeds) to obtain footage and kinematics of insect flight in unprecedented resolution. High-speed cameras operated on rails for ease of distance adjustment between insect species, to achieve wing length to be approximately 70 – 80 pixels, and studio gear heads for angle adjustment (Manfrotto 400, UK). Cameras were further supported by two 1.2 and 1.4 m scaffold rings fabricated by Barnshaw Section Benders Ltd, West Midlands and linear scaffold supports by Scaffolding Direct, Wirral. To provide additional stability, heavy-duty magnets (MB175B, THORLABS) were used throughout the system: under each light-emitting diode (LED) which provided backlighting, and aluminium struts (RS PRO, UK) suspending the free flight arena. The platform placed under the centre of the camera rig, was a 1 mm thick mid-steel sheet (a magnetic metal) bolted on to medium-density fibreboard that enabled easy adjustment of these heavy-duty magnets. During experiments, care was also taken to not touch the rig, for instance, leaning on the scaffold rings during data collection to avoid the introduction of oscillations.

All insects were filmed between 20 - 23 °C and ~ 20 - 65 % humidity (Thermo-hygrometer, Testo 608-H1 and RS PRO RS42 Thermometer) unless stated otherwise. A pooter or falcon tube was used to transfer individuals from their housing to the free-flight arena and for weighing.

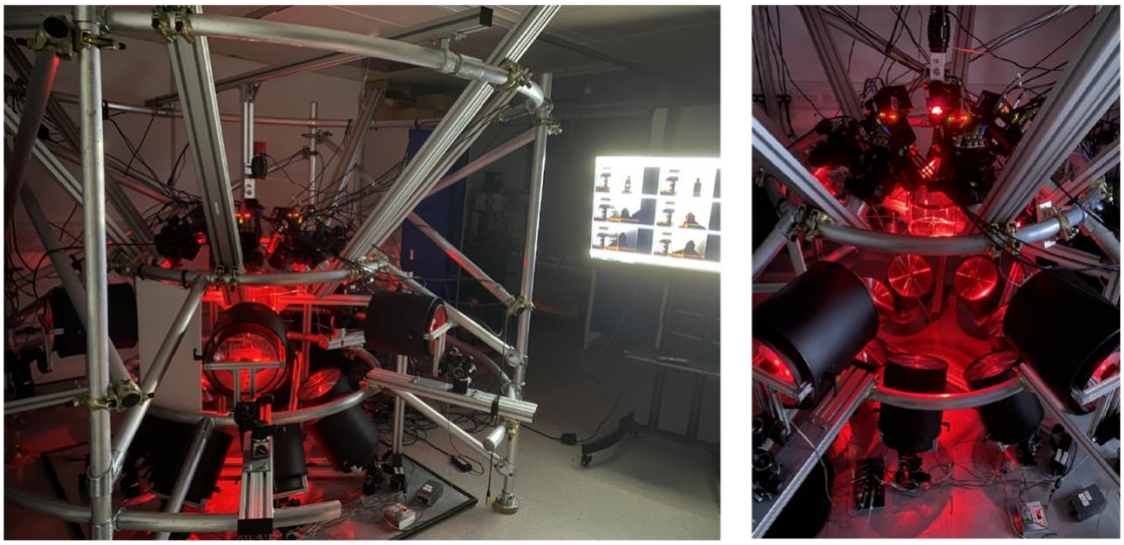

Figure 2.1 High-speed camera rig used to capture insect flight

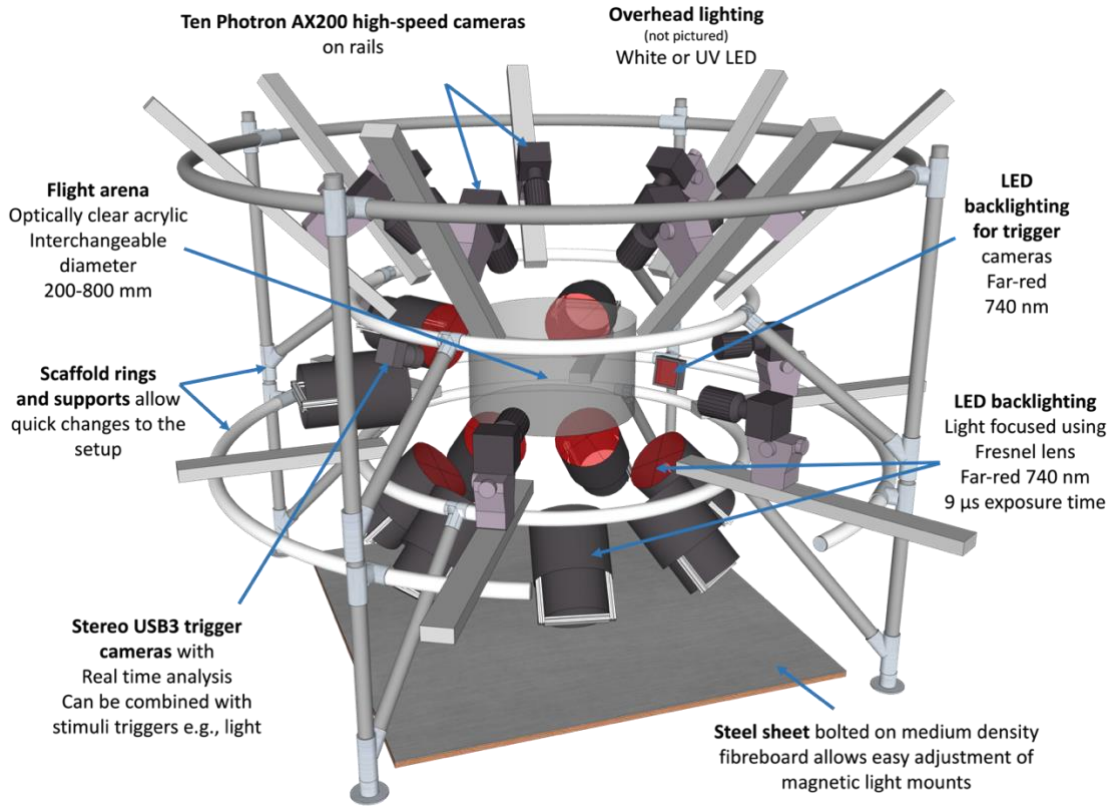

Figure 2.2 3D rendering of the free flight arena and surrounding camera rig

Insects were placed and encouraged to fly within the centre of the free flight arena. When passing through the common recording volume of the high-speed cameras, they were activated to start recording by USB-3 trigger cameras with live background subtraction and thresholding adjusted for each species.

2.2.1 High-speed Videography / Kinematic Acquisition

To maximise the coverage of insects during take-off and free-flight, ten high-speed cameras (FASTCAM Mini AX200, Photron Ltd) with 150 mm f/2.8 macro lenses (Dragonfly, irix) were used for filming. Three cameras were positioned horizontally (~ 0 °) and seven pointed vertically down (~ 50 – 55 °) to face the centre of the free flight arena (**Figure 2.2)**. Three of the high-speed cameras were further assigned specific roles: (I) one horizontal camera (0° using a BOSCH GLM 80 Professional Spirit Level) acted as a master camera vital for camera calibration and defining the lab coordinate system, and two slave cameras were responsible for (II) manual triggering and (III) output to the LED driver for LED-camera pulse synchronisation using BNC connectors. When starting up, high-speed cameras were left to warm up for a minimum of ten minutes before software (Photron FASTCAM Viewer 4 (PFV4), Version 4.0.5) auto-calibration to remove banding artefacts generated from intrinsic heat.

Positioned opposite each high-speed camera was a far-red LED (LZ1 Series 5W LED Emitter Module, LedEngin Inc., USA), acrylic LED diffuser, and 10.4” diameter, 8” focal length Aspheric Fresnel lens (Edmund Optics, UK) on a geared tripod head (Manfrotto 410, UK). Far-red light paths were then aligned and focused directly into each camera lens to provide a bright and uniform background (consistently between 170 and 255 RGB) ideal for silhouetting insects and background subtraction (**Section 2.2.3**). To aid this, cameras were also set to operate with a 9 μs exposure time to minimise motion blur based on the insects typical wingbeat frequency. The far-red LEDs were controlled by a

custom-built LED driver with pulse width modulation (PWM) to strobe them for maximum brightness, and to match the high-speed camera sensor absorption frequencies with a peak wavelength of 740 nm, and a cut off frequency of 675 nm. This is outside the visible spectrum of most insects with an upper limit of 600 nm (Briscoe and Chittka, 2001, Bernard and Stavenga, 1979). Insects were provided a white LED (Mounted MWWHLP1, Thorlabs) to see and encourage flight. The white LED was fitted with a 650 – 1050 nm adjustable collimation adapter lens (SM2F32-B, Thorlabs) and 1200 mA Max Drive current T-Cube LED Driver (LEDD1B, Thorlabs) to be able to vary its intensity from above.

Stereo USB 3.0 monochrome industrial cameras (Basler acA720 – 520 um and Pylon Viewer Version 7.4.0 (Basler AG, Germany)), each fitted with a 90 mm f/2.8 Tamron SP Di macro lens (Tamron, Japan), and Nikon G-mount to C-mount camera lens adapter (Nikon, USA) on a tripod micro ball head (Manfrotto 492, UK), operated as triggers cameras for the high-speed cameras to start recording when insects entered their region of interest (ROI). Trigger cameras ran alongside Bonsai software (Version 2.8.1.4300, Bonsai Foundation UK) for real-time background subtraction and motion segmentation/thresholding at 250 fps (Multicomp PRO MP750510 Arb Waveform Generator) and shutter speed 1/500 second. These were then focused onto custom built far-red panel lights fitted with a diffuser for backlighting. All footage was captured in PFV4 and saved as uncompressed 12-bit files to retain image detail. Accompanying cihx text files containing camera and sequence details was also saved for each video.

Multiple flight arenas were available with inner sections between 200 and 800 mm in diameter, and were selected depending on the size of the insect and the volume required to encourage natural flight (**Table 2.1**). Each consisted of two optically clear cast 1 mm thick acrylic discs (Simply Plastics, UK), 250-micron acetate walls (Diacel, Japan), two aluminium custom-made rings with 10 mm thick black foam tape boarders (RS PRO, UK), and two aluminium vertical strut supports (Rexroth, Bosch) to form a cylinder camber. However, the 200 mm flight arena's rings and vertical struts were 3D printed in tough white polylactide (Shapr3D Version 5.4 and printed with the Ultimaker S7 Pro Series) and epoxied (Araldite Rapid, USA) together for increased rigidity. Arena height, orientation and elevation was determined by its centre and the position of opaque objects that made up the flight arena e.g., aluminium rings, so that they did not obstruct camera views (approx. arena diameter to height ratio 0.65 : 1.0). To ensure a common field of view, a calibration object with a 30G ½" 0.3 x 13mm micro-lance needle tip was placed in the centre of the flight arena. All cameras were then aligned and focused onto the tip of the needle; with the high-speed cameras this was further done at low aperture (setting Q) to maximise the depth of field but fully opened (setting A) for data collection.

At the end of experiments, subjects were collected, anesthetised by placing them in - 20 °C for five to ten minutes, and then quickly weighed using a AX26 DeltaRange Microbalance (readability 0.2×10^{-5} g, Metter Toledo, UK) to minimise the effects of desiccation.

Table 2.1 Table summarising species-specific camera and flight arena parameters

Species	Wingbeat Frequency (Hz)	Approx. Wing Length (mm)	Arena Diameter (mm)	Recording Diameter (mm)	Recording Frequency (fps)	Recording Resolution (px)
Anopheles gambiae	600 - 800	3	200	31	12,000	768 × 720
Coenosia attenuata	300	3	200	40	6,400	1024 × 1024

2.2.2 Camera Calibration

At the start and end of each data collection day, high-speed cameras set at 250 fps, shutter speed 1/250 and with the same resolution used to record insect footage was used to take ~ 100 synchronised images of a manually held calibration grid at random positions, rotations, and translations. Here, four separate far-red LEDs (with the same wavelength as backlights) fitted with lenses (LE1-M, LEDiL, USA) to reduce divergence were used to provide front illumination and maximise the contrast of the calibration grid. This calibration device consisted of an adjustable handle (MSWC 360 º swivel post clamp and MS3R/M optical posts, Thorlabs, USA) and flat, square 0.5 mm thick piece of white acrylic, with a grid of matt black open and closed circular dots (14 by 14) pasted on its surface (**Figure 2.3**). Grid spacing options were made available between 0.5 and 4 mm, and dot diameter differed proportionally with steps in recording diameter, meaning the smallest insect species recorded required the

0.5 mm dot spaced calibration grid. This was done in preparation for camera calibration in a custom MATLAB graphic user interface (GUI) as detailed in (Walker et al., 2009). Here, a bundle adjustment technique was used to estimate the spatial coordinates of the circular dot calibration grid, camera parameters and to calculate pixel error of individual data points. Calibration images were retaken if pixel error was greater than one pixel. This photogrammetric technique was useful as it does not require prior information on camera position and orientation except the master camera. Collinearity equations for each camera were solved simultaneously with constraint equations fashioned from known dimension constraints taken from the calibration images to include grid spacing, translation and orientation permitted by the open circles in one corner. Solving accuracy increases with more camera views (Walker et al., 2009).

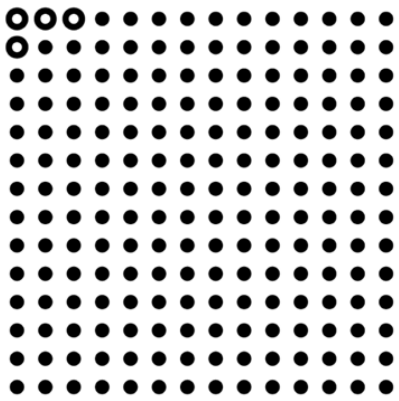

Figure 2.3 Camera calibration grid

14 by 14 calibration grid consisting of four open left-hand side circles and closed circles. Images of the calibration grid were taken in all ten camera views at random orientations to achieve pixel errors less than one. Not to scale.

2.2.3 Video Processing and Kinematic Reconstruction

Following camera calibration, insect footage was digitised to obtain wing and body kinematic parameters using a custom MATLAB script written by S.W, University of Leeds as follows and as summarised in **Figure 2.4**. Background images were first created by stacking the images of each sequence and taking the brightest pixel to build a new image. Where physical obstruction was consistent for instance, when my hand or the insect flew directly towards a high-speed camera, the background was substituted with one from the same camera from a previous recording, or the camera footage (a copy) was deleted moving forward to leave footage from the remaining nine cameras. For image cropping, a generic MATLAB blob detection tool was used on four out of the ten cameras that minimise reprojected pixel error and the assumption that it is unlikely that objects would obstruct multiple cameras. Cropped images were then saved as binary images, segregating the body and wings (**Figure 2.5**). Only then the tracker could be run, employing a voxel carving method (also known as hull reconstruction) to reconstruct the body, wingtip (stroke angle and deviation angle), and wing outline (getting leading and trailing edge for wing pitch, wing twist and spanwise bending) respectfully (**Figure 2.6** and **2.7**). Kinematics were filtered and corrected with each processing step described above (from measuring body kinematics onwards in **Figure 2.4**) to avoid accumulating tracking error. Use of the Parallel toolbox on MATLAB enabled multiple frames to be processed simultaneously. The same tracker was used for all insect species recorded although, some parameters for example, morphological operations

(e.g., erode and dilate) and frequencies used for filtering between tracker steps was tailored and commented out accordingly.

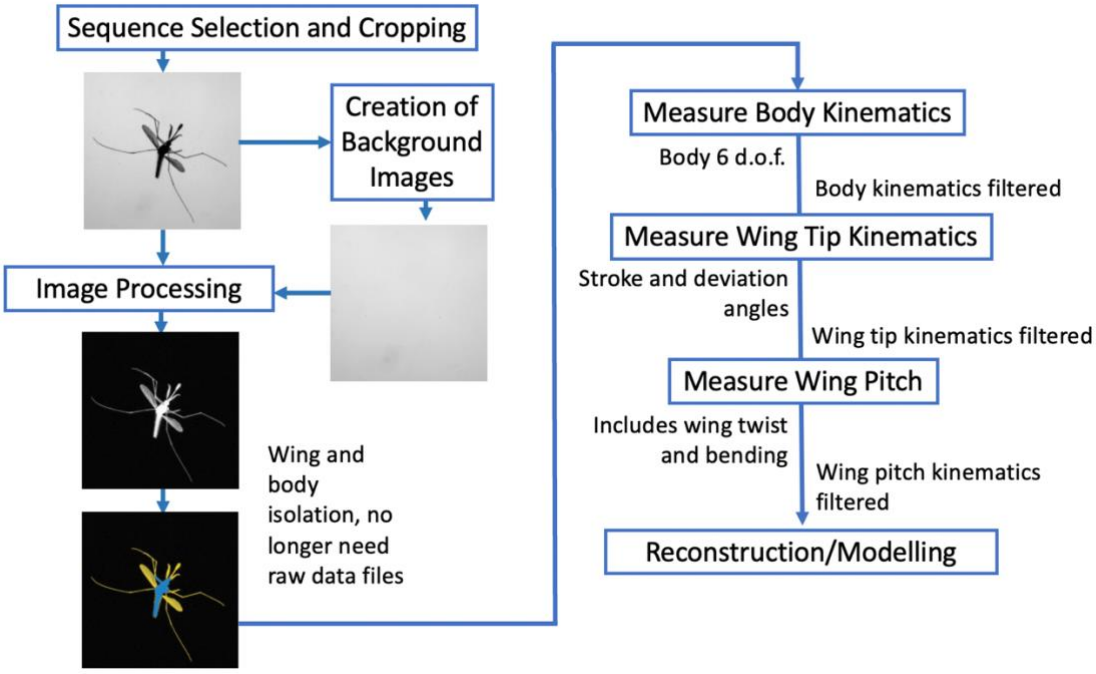

Figure 2.4 Flowchart of data processing pipeline to get insect wing and body kinematics

Degrees of freedom (d.o.f).

Figure 2.5 Cropped images of the same mosquito flying in all ten camera views

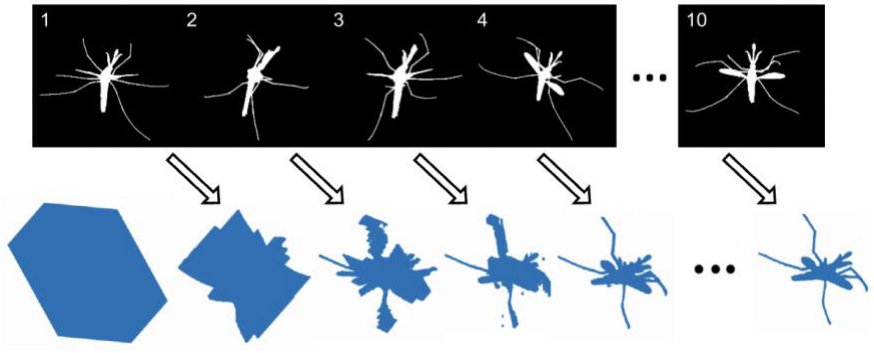

Figure 2.6 Voxel carving method

A block of voxels is carved with each camera view. The final product after ten cameras, is a 3D shape largely resembling the insect recorded.

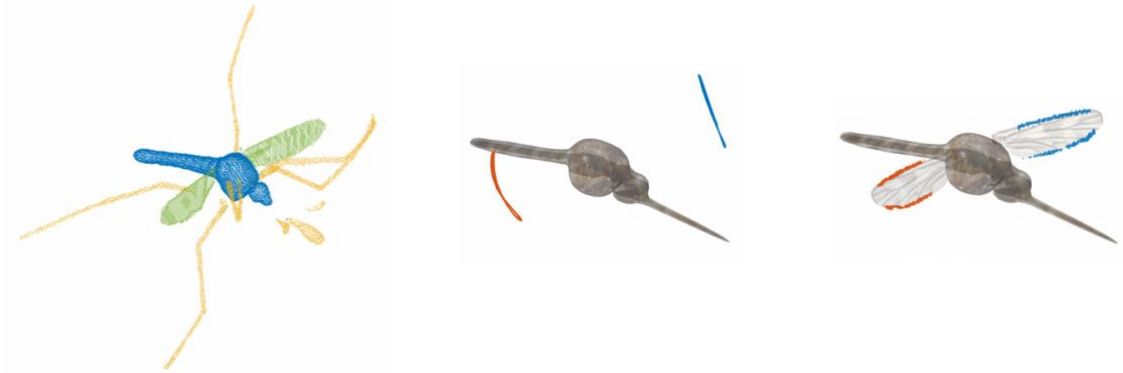

Figure 2.7 Visualising data processing steps

From left to right, body segmentation result from voxel carving, tracked wing tips (left wing orange, right wing blue) and voxel outlines of the wing's leading and trailing edge (left wing orange, right wing blue).

2.2.4 Defining Kinematic Parameters

All body and wing kinematics follow the same format as described in (Walker and Taylor, 2021). Body kinematics were defined using a right-handed body-fixed axis system {X_b, Y_b, Z_b} where its origin was fixed about the centre of body volume (voxels) as shown in **Figure 2.8**. The X_b axis pointed anteriorly, extending beyond the body's major axis, the Y_b axis was positioned to the side, parallel to a line joining the wing hinges and the Z_b axis pointed down. The body axis was measured in a fixed laboratory coordinate system {X, Y, Z} (not illustrated), and the outcome of torques (from variable symmetric and asymmetric forces generated by the wings) was described by a series of Euler rotations/angles: yaw (Ψ, z-axis of rotation), pitch (θ, y-axis of rotation) and roll (ϕ, x-axis of rotation) needed to go from the lab-fixed axis system to the body-fixed axis system.

For wing kinematics, I used the right-handed body-axis axis system {X_R, Y_R, Z_R} for the right wing and the left-handed body-axis axis system {X_L, Y_L, Z_L} for the left wing where their origins were located at their respective wing base (**Figure 2.8**). The spanwise rotational axis is defined as a line originating from the wing base to the wingtip. Wingtip kinematics, stroke angle (φ) and deviation angle (θ) are the azimuth of the spanwise rotational axis from the wingtip and wing elevation respectfully. The stroke plane is defined for each wingbeat from a line drawn between the wingtip at the start of upstroke and downstroke (at stroke reversal). Wing pitch angle (ω) is the angle between the wings anatomically ventral side perpendicular to the Y_R axis and the X_RY_R plane, once the positions

of stroke angle (Z_R axis) and deviation angle (X_R axis) have been subtracted (Walker and Taylor, 2021).

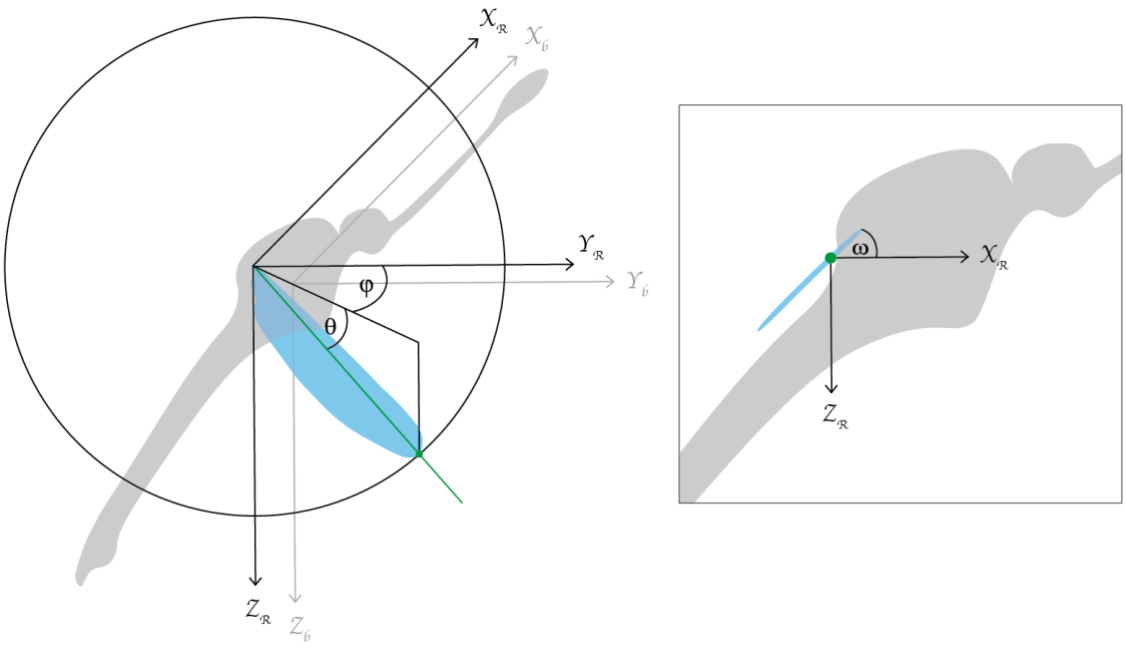

Figure 2.8 Wing kinematic parameters

Stroke angle (φ, left), deviation angle (θ, left), wing pitch angle (ω, right). The body axis system {X_b, Y_b, Z_b} with the grey arrows is centred about the bodies centre of voxels. The right wingtip kinematics are defined by the right-handed axis system {X_R, Y_R, Z_R} with the black arrows originating from the right-wing hinge, and left wingtip kinematics by the left-handed axis system {X_L, Y_L, Z_L} originating from the left-wing hinge (not shown). The green dot is the wingtip located on the apex of the wing (blue) and is used to define the spanwise rotational axis (green line). Figure adapted from (Walker and Taylor, 2021).

Wing twist (**Equation 2.1**) is a regression modelled with a pitch angle offset (zero x-coordinate and fitted y-coordinate) and linear twist gradient (degrees per unit length) component, by first calculating a local pitch angle along the wings radial coordinate (*r*).

Equation 2.1 Calculation of wing twist

$$\widehat{\omega}(r) = \omega_0 + \omega_r r$$

Spanwise bending (**Equation 2.2**) is proportional to the wing (i.e., 0.1 means 10 % of wing length) and is calculated using a modified sine function below,

Equation 2.2 Calculation of spanwise bending

$$\mathrm{A}\sin \pi\, r$$

where A is amplitude of the wingtip and radius (r) is 0 to 1.

Chapter 3

High-precision Wing and Leg Kinematics of *Anopheles gambiae* during free-flight

3.1 Introduction

Mosquitoes are major vectors of disease (e.g., Zika, Dengue and Malaria) and thus, methods to limit their populations have become a popular research topic. Management strategies dominate the reproductive stage for example, by releasing sterile males (Bouyer et al., 2020), odour-baiting females (Fillinger et al., 2023), and the development of acoustic lures (Johnson et al., 2018). The latter utilises the fundamentals of mosquito courtship behaviour at dusk, which involves the detection of female flight tones (by-product of wing movement) followed by a highly orchestrated dance (Somers et al., 2022, Aldersley and Cator, 2019). To show compatibility, some species synchronise their wingbeat frequencies to match females in close proximity (e.g., *T.brevipalpis*) whilst others undergo harmonic convergence (Arthur et al., 2014, Gibson and Russell, 2006, Pennetier et al., 2010). Males therefore operate over a greater range of wingbeat frequencies than females, that has been speculated be a measure of fitness before copulation (League et al., 2021).

It is unclear if there is a biomechanical (e.g. for power muscle contraction efficiency) or aerodynamic advantage when performing flight with higher wingbeat frequencies. For the reason that, it is certainly expensive to do so at

their small size due to high inertial power requirements and wing loading (Kim et al., 2021). Bomphrey et al. (2017) provided some insight, as they reported two novel aerodynamic techniques during the rotational phase of flapping flight termed trailing edge vortex (TEV) and rotational drag. However, we still have no knowledge on how they utilise these techniques when manoeuvring with their high aspect ratio wings (*AR* = 4.2, versus *AR* = 2.5 in *Drosophila* despite operating at similar scales (Ray et al., 2016)). The TEV is a form of wake recapture during supination and pronation, where the wake first intercepts the trailing edge to generate a negative pressure region above before shedding. Whereas during rotational drag, the wings' rotational axis migrates from the leading to the trailing edge mid-rotation to maintain the production of positive lift, normal to the posterior wings surface at the end of downstroke as supination begins. As a result, the importance of lift generation during the translation phase (that is usually LEV dominated) of stroke cycles is unconventionally shifted to the rotational phase, allowing for just two chord lengths travelled between stroke reversals (Bomphrey et al., 2017).

Mosquitoes also have long narrow limbs that enable them to take-off and land on hosts undetected, whilst also being up to three times heavier after a blood meal (van Veen et al., 2020). When taking off, limbs are first slowly extended to minimise peak leg force (ground reaction force 0.02 mN over 26.3 ms) so that it is under the mechanoreceptor threshold of hosts (0.07 mN in mice (Li et al., 2011)). The wings are then flapped to produce the remaining 61 % of total push-off force (Muijres et al., 2017). Smooth surfaces that are likely to cause slippage and affect downstream aerodynamic force production are also overcome by mosquitoes, by raising and striking the ground with their rearmost legs to produce

near identical vertical body velocities as normal push-offs (Smith et al., 2018). Once the mosquito is airborne their legs then spread (Liu and Sun, 2019). This leg behaviour has been observed similarly in *Drosophila* (Berthé and Lehmann, 2015) and *Euglossa* (orchid bee) (Combes and Dudley, 2009b), to act as useful rudders by increasing their profile drag to increase stability and fine tune control. Nonetheless, detail on insect leg kinematics during flight remains minimal in literature only describing leg retraction and extension in the rare instances (Combes and Dudley, 2009b, Berthé and Lehmann, 2015).

Mosquitoes continue to push our technical ability to observe insect flight aptitude, with their high wingbeat frequencies, small high aspect ratio wings, and long antennae and legs that may also obstruct camera views. The primary aim of this experimental chapter, was to therefore investigate how *Anopheles gambiae* alter their kinematics during natural free-flight. The experimental setup and data processing pathways used (described in **Section 2.2**) enabled me to generate a large database of high-precision wing and body free-flight kinematics including: wingtip angles, mid-wing pitch, wing twist gradient, spanwise bending, and body roll through the stroke. Leg kinematics defined as swing (stroke like angle), elevation (deviation like angle) and tilt (pitch like angle), were also acquired from fully intact and damaged mosquitoes that had experienced leg loss, by using a supplementary skeletonization image processing technique preceding voxel carving. By obtaining these measurements, how relevant mosquito legs are to flight stability (typically indicated as a substantial proportion of body moment of inertia (MOI)), and the effect of leg loss (e.g., the adjustment of their remaining leg kinematics) could be investigated. To facilitate this, additional morphological measurements of the body's centre of mass (COM) and leg radius, was used to

calculate the body and leg MOI for comparison. Results described here will help illuminate the complementary roles of (non-wing) appendages in other insect species, and could be used to develop the most advanced population management techniques, and estimations of aerodynamic force production to date.

3.2 Methods

3.2.1 Insect Care

G3 *Anopheles gambiae* (mosquito) were kindly provided by the Albert Lab, University College London (UCL) Ear Institute. Recordings only took place 2 - 5 days post-eclosion due to reductions in fitness post-transit. Mosquitoes of the same sex were housed in groups of 5 - 10 in 360 ml BugDorms (MegaView Science Company, Taiwan), with cut up cotton rolls saturated in a 1:10 sugar and distilled water mix. BugDorms were then placed in two 30 × 30 × 30 cm mesh cages for extra security when handling, then again into two black opaque boxes with fitted white LED strips (colour temperature 5500 - 7000 K, RS PRO, UK) inside. LED strips were fixed to a 05:00 to 17:00 (in one) and 07:00 to 19:00 (the other) ON OFF cycle using a digital timer switch (230 V ac, RS PRO, UK) to simulate day and night. Humidity was maintained between 70 - 80 % using a 4-litre GEEKEN humidifier and Inkbird 1HC-200 dual humidistat controller. While temperature in housing was maintained between 25 - 28 °C using FIPASEN heating mats and a Inkbird ITC-308 temperature controller. Mosquitoes were left to acclimatise for several hours before filming in the evening or the next day. Short acclimation times were only possible as it aligned with those used at the UCL Ear Institute with overnight shipment.

3.2.2 Tailored Kinematics Acquisition

To ensure a large window for data collection each day, mosquito cages operated on different day night cycles. Recordings were collected between 19.4 ° C and 35.2 ° C and were only attempted two hours before each box and its LED were set to turn-off (i.e., 15:00 - 19:00), and within 30-minutes of each BugDorm being left in the dark (see below) to sample within swarm times. This is when male mosquitoes have been observed to be most active as part of courtship behaviour whilst female mosquito behaviour remains the same (Somers et al., 2022). All experiments were therefore performed in the dark, but within an approximate 4 - 16 lux (Light Meter LT300, EXTECH INSTRUMENTS, USA) environment inside the free flight arena with calibration (for the user to see the insect), trigger and backlight far-red LEDs on, and with blackout curtains surrounding the camera rig.

High-speed cameras as detailed in General Methods (**Section 2.2.1**) were positioned so that mean wing length (approximately 3 mm) of *A.gambiae* supplied was ~ 80 pixels long during experimental setup. All high-speed cameras were then set to operate at 12,000 fps, shutter speed 1/frame second, 768 × 720-pixel resolution and with a common field of view (diameter) of 31 mm (~ 10 wing lengths) in the centre of a 200 mm diameter free flight arena. To induce manoeuvres in mosquitoes one at a time, an additional small, directional white LED (MP000435, MULTICOMP PRO, USA) was added to the Bonsai workflow (Version 2.8.1.4300, Bonsai Foundation UK) to turn on for one second upon individuals entering the trigger cameras ROI. The small white LED was thread through a 5 mm hole, in the centre of the flight arena’s acrylic top disc and

suspended immediately above the recording volume so that it did not obstruct any camera views.

Forward and backward filtering was performed on the tracked body and wingtip kinematics (**Section 2.2.3**) using a 3rd order low pass Butterworth filter, with a cut-off frequency of 180 Hz and 2400 Hz for the body and wingtips respectfully. Whereas a 5th order low pass Butterworth filter with a cut-off frequency of 3000 Hz was used on wing twist. These values were selected to remove jitter from the wings on the centre of voxels and be below the limits of what I would expect oscillations to occur at when flapping to avoid the removal of any underlying signal. For definitions of wing kinematic parameters please refer to General Methods in **Section 2.2.4**.

For leg kinematics, if all existing limbs were within the field of view in six or more high-speed cameras, a supplementary leg tracker after voxel carving was used every 10 frames. The number of legs present was quickly monitored using the pixel parameters of each sequence, which was only possible as legs were much longer than the wings. If leg view became obscured or out of frame during a sequence no data was recorded for these frames. Each recorded limb then underwent skeletonization (erosion and dilation) until a single line of pixels was produced for each frame and leg coordinates averaged for each sequence. Limbs were therefore treated as a non-drying object where the limb could only rotate around its base. Each leg was then manually scored as a fore-, mid-, or hind-limb, as it was challenging to automate the differentiation between ipsilateral limbs.

The right leg axis system {X_{Rleg} Y_{Rleg}, Z_{Rleg}} was defined with respect to a right-handed axis system (parallel to the body axis system) where X_{Rleg} originated from the leg base (0,0) pointing forward, Y_{Rleg} axis out to the side and Z_{Rleg} axis points down as illustrated in **Figure 3.1**. This remained true for the left leg axis system {X_{Lleg} Y_{Lleg}, Z_{Lleg}} but mirrored using a left-handed axis system (not shown). Swing was defined as a stroke like angle, describing rotation in the vertical axis (yaw), elevation was a deviation like angle describing rotation in the front to back axis (roll), and tilt was pitch like angle describing twist in the Y_{Rleg} (side to side axis, pitch) once swing and elevation position have been subtracted. Limbs were labelled according to **Figure 3.2** where L1 – 3 were used to describe left legs and R1 - 3 for right legs for the fore- (L1 and R1), mid- (L2 and R2) and hind-legs (L3 and R3) respectfully.

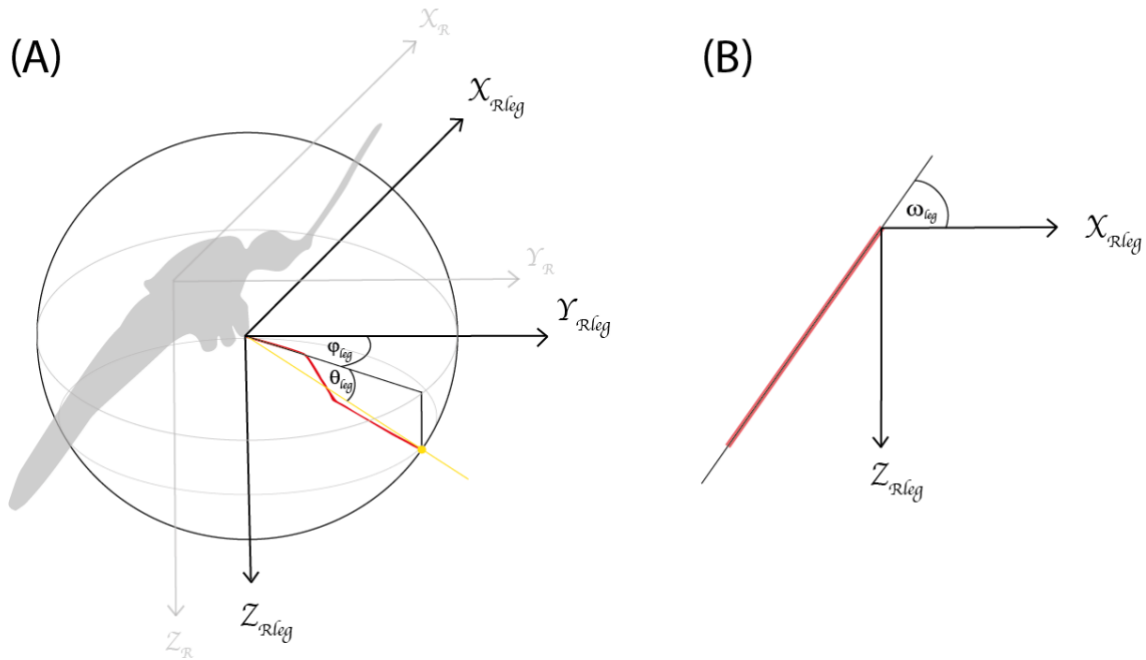

Figure 3.1 Defining leg parameters

(A) Swing (φ_{leg}, stroke like angle), (A) elevation (θ_{leg}, deviation like angle) and (B) tilt (ω_{leg}, pitch like angle). Right leg axis system {X_{Rleg} Y_{Rleg}, Z_{Rleg}} with reference

to the right-handed axis system. Body axis system {X_R Y_R, Z_R} in grey. Mosquito only features one leg (red) for illustration purposes. Figure adapted from (Walker and Taylor, 2021).

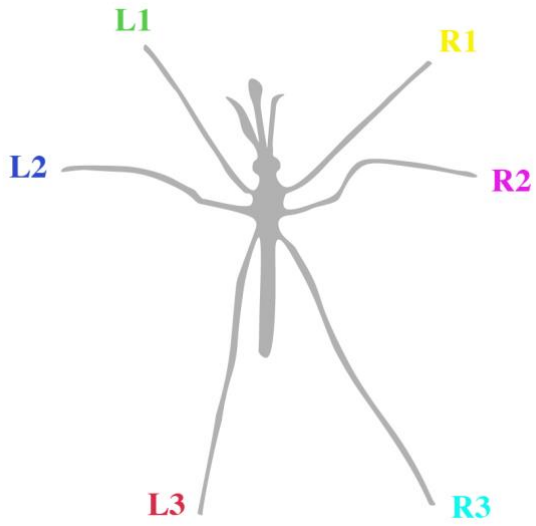

Figure 3.2 Mosquito leg key

L1 (green), L2 (blue) and L3 (red) were left legs and R1 (yellow), R2 (magenta) and R3 (cyan) were right legs. Wings have been excluded for transparency.

3.2.3 Mosquito Metrics

Body length and wing length of recorded individuals were automatically quantified in the fly tracker script. To compensate for leg loss and leg MOI calculations, grouped leg mass (AX26 DeltaRange Microbalance (readability 0.2 $\times$ 10^{-5} g, Metter Toledo, UK)) to work out averages for fore-, mid- and hind-limb mass were further recorded. This was done quicky after detachment to minimise the effects of desiccation and subtracted from the estimated body mass.

Leg segment lengths (femur, tibia, and tarsus) were acquired by detaching fore-, mid- and hind-limbs (10 each) from 30 different mosquitoes of mixed sex, imaging them with a 1 mm stage micrometre (Leica S8 APO, Leica Microsystems Ltd) one at a time, and determining their segment lengths and segment radius (taken from the mid-point of leg segments) using ImageJ (Version 1.52q, Wayne Rasband NIH).

3.2.3.1 Hanging Experiments for Centre of Mass

To calculate the COM, a U-shaped rig fashioned from profiled aluminium struts (RS PRO, UK) and corner connectors was used (Bosch-Rexroth, Germany). Black braided silk (SP103, Surgical Specialties, USA) was then clamped across the U-shape (bridge) and a plumb line with 15 mm washer hung in line with gravity. A self-clamping crossover tweezer (stainless steel N5, 0.1 x 0.06 mm tip, Dumont HP, USA) was then hung parallel to the plumb line, used to clamp on to the tip of a subject's leg, and left to stabilise (**Figure 3.3A**). Images of the mosquito body (in the sagittal plane) from multiple leg hanging points, were then taken using a Nikon D70 camera with a Nikon F mount (Nikon, Japan), 60 mm f/2.8 2X Ultra-macro LAOWA lens (0023745, LAOWA), Lumecube (5600 K, LC-PANEL 112, USA) to provide front lighting, and a white foamboard backdrop.

Once all images had been taken, a MATLAB script was used to calculate the COM by clicking on the proboscis base, scutellum, abdomen end, wing base, haltere base, hanging point, and the top and bottom of the plumb line. A line was

then drawn between the proboscis base, scutellum and abdomen end for detail on body orientation and scaling of individuals (**Figure 3.3B**). All image coordinates were then rotated, translated, scaled, and overlayed to estimate the position of the COM where lines from the hanging point in line with gravity intercepted on the mosquito's body.

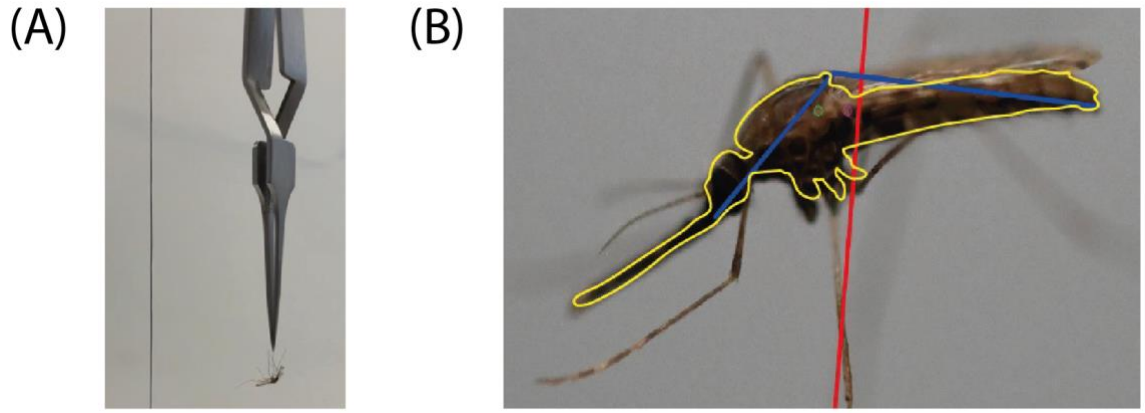

Figure 3.3 Hanging experimental setup to calculate mosquito centre of mass

(A) Hanging experimental setup and (B) mosquito image taken in the sagittal plane, haltere base (red circle), wing base (green circle), line drawn joining the proboscis base, scutellum and abdomen end (blue), hanging point in line with gravity (red line) and body outline (yellow). The location of the centre of mass, is the interception point of red lines when clicked images are overlayed (not pictured).

3.2.3.2 Calculating Moment of Inertia

3.2.3.2.1 Body Moment of Inertia

To determine the body's MOI in line with the parallel axis theorem, a mosquito mesh model was constructed from photos taken under microscope (Leica S8 APO, Leica Microsystems Ltd) and scaled for each individual (**Figure 3.4A**). Each model was then segmented into a series of ellipsoids from the proboscis base to the tip of the abdomen (**Figure 3.4B**). The volume of each ellipsoid, total volume of the body, and mass of each ellipsoid assuming uniform density was then estimated respectfully. Only then, the MOI of each ellipsoid ($I_{ellipsoid}$) and the total MOI of the body (I_{body}) about the body's roll axis could be calculated using **Equation 3.1** and **Equation 3.2** where,

Equation 3.1 Moment of inertia of an ellipsoid about its own axis

$$I_{ellipsoid} = \frac{1}{5}m(a^2 + b^2)$$

Equation 3.2 Total body moment of inertia

$$I_{body} = \sum_i (I_{ellipsoid_i} + (m_i {d^2}_i))$$

m is the mass of the ellipsoid, $\boldsymbol{a}$ is the ellipsoid's semi-major axis, $\boldsymbol{b}$ is the ellipsoid's semi-minor axis, $\boldsymbol{d}$ is the distance between the ellipsoid's centre and the location of COM of the mosquito, and $\boldsymbol{i}$ is the $\boldsymbol{i}$-th ellipsoid.

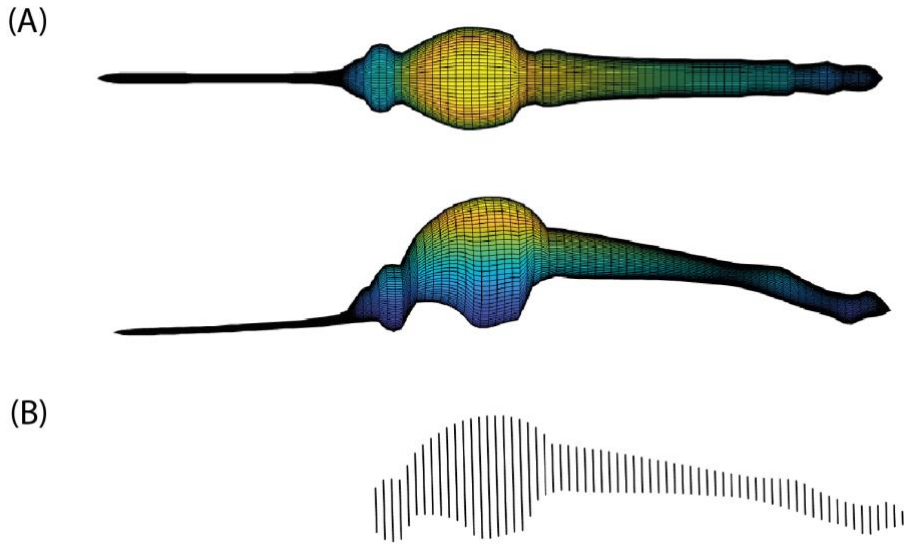

Figure 3.4 Mosquito mesh model used to calculate the body's moment of inertia

(A) Dorsal and lateral view of the mosquito model. (B) Equatorial circumference (widest circular section) of each ellipsoid.

3.2.3.2.2 Leg Moment of Inertia

To calculate and sum the MOI of mosquito legs, leg lengths were divided into three segments (femur, tibia, and tarsus) using the ratios determined for the fore-, mid- and hindlimbs independently (**Section 3.3.1.1** and **Figure 3.5A - B**). The volume of each leg segment was then estimated as a cylinder to estimate leg

segment mass assuming constant density. Each leg segment mass was then divided to make up a total of 100 parts (point mass) for all three segments to calculate the leg MOI as solid spheres (I_{sphere}, **Equation 3.3**) as illustrated in **Figure 3.5C,** and total leg MOI (I_{legs}, **Equation 3.4**) about the body's roll axis.

Equation 3.3 Moment of inertia of a solid sphere about its own axis

$$I_{sphere} = \frac{2}{5}mr^2$$

Equation 3.4 Total leg moment of inertia

$$I_{legs} = \sum_i (I_{sphere_i} + (m_i d^2{}_i))$$

m is the mass of the sphere (point mass which can be from any leg section (femur, tarsus, or tibia) of the fore-, mid- or hind-limbs), r is the radius of the leg section (from images, **Table 3.1**), d is the distance between the sphere's centre and the location of COM of the mosquito, and i is the i-th leg part (out of 100 for each leg, **Figure 3.5C**).

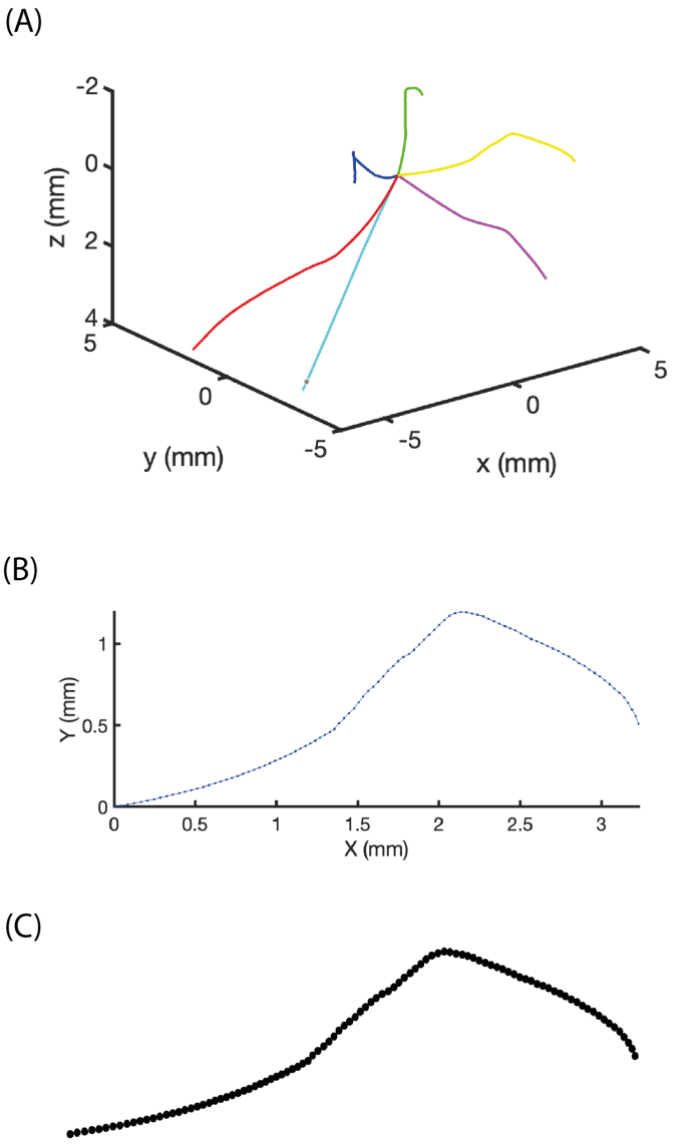

Figure 3.5 Calculating the moment of inertia of mosquito leg's

(A) Example of mosquito tracked leg positions and typical leg posture during flight. (B) Example forelimb tracked as 100 points. (C) 100-point masses to be modelled as spheres for leg moment of inertia calculations. Not to scale.

3.2.4 Statistical Analysis

For wing kinematics (e.g., stroke angle), all minimum and maximum values (local minima and maxima) for each wingbeat was checked for normality using a Kolmogorov-Smirnov test (suitable for large sample size). Significance was then determined between male and female wing kinematic parameters using a non-parametric Mann-Whitney *U* test that does not assume a normal distribution.

For leg kinematics, normality was also tested using a Kolmogorov-Smirnov test. A non-parametric Kruskal-Wallis *H* test (0.05 alpha) was then used to test the significance between three or more categories for each leg kinematic parameter. To correct for multiple comparisons, a post-hoc Dunn's multiple comparison hypothesis test was used to calculate adjusted *P*-values. This was done by multiplying uncorrected *P*-values by the number of groups, thus making it more difficult for *P*-values to be significant. If this product was greater than one, the adjusted *P*-value has been shown as > 0.9999. If only comparing two categories, a Mann-Whitney *U* test (two tailed for non-directional change) was used. Significance was concluded if $P \leq 0.05$.

For body roll and leg loss, the mean body roll of each sequence was calculated then grouped according to the number of uneven or even ipsilateral legs loss (between left and right sides). Normality of all groups was then tested using a Kolmogorov-Smirnov test, and significance determined between groups of uneven ipsilateral leg loss and the group with an equal number of left and right legs lost using a Mann-Whitney *U* test.

3.3 Results

The results in this chapter have been divided into three subsections: (1) mosquito metrics (including COM and MOI), (2) high-precision wing kinematics and (3) leg kinematics. I would also like to note here, that as I was interested in the upper limits of mosquito flight (e.g., highest wingbeat frequencies and lowest stroke amplitudes), I sampled within swarm times at dusk however, males did not swarm as antennae remained retracted during recordings. Nonetheless, male mosquitoes generally flew at higher wingbeat frequencies than the females and covered wingbeat frequencies previously observed during swarming flight (Pantoja-Sánchez et al., 2019, Cator et al., 2010, Garcia Castillo et al., 2021).

An overview of summary parameters can be seen in **Figure 3.6,** where I included 12,578 wingbeats extracted from 195 sequences (*N* = 137 males and *N* = 58 females sequences), with a mean sequence length of 1,179 frames (99 ms) from 129 free-flying individuals (*N* = 90 males and *N* = 39 females). The highest wingbeat frequency recorded was 1,015 Hz and lowest stroke amplitude averaged from both wings was 12.9 º (see Appendix **Figure 0.1** for reductions in stroke amplitude alongside wingbeat frequency and vertical acceleration over wingbeats for this sequence). Wingbeat frequency varied greatly in this dataset but variation was due to differences between individuals rather than within individuals regardless of sex. Whereas, stroke amplitude displayed a broader range within individuals but with some greater exceptions owed to more dramatic manoeuvres e.g., quick descents where weight support is less important. The

effect of varying ambient temperature on body and wing kinematics will be addressed in **Chapter 4**.

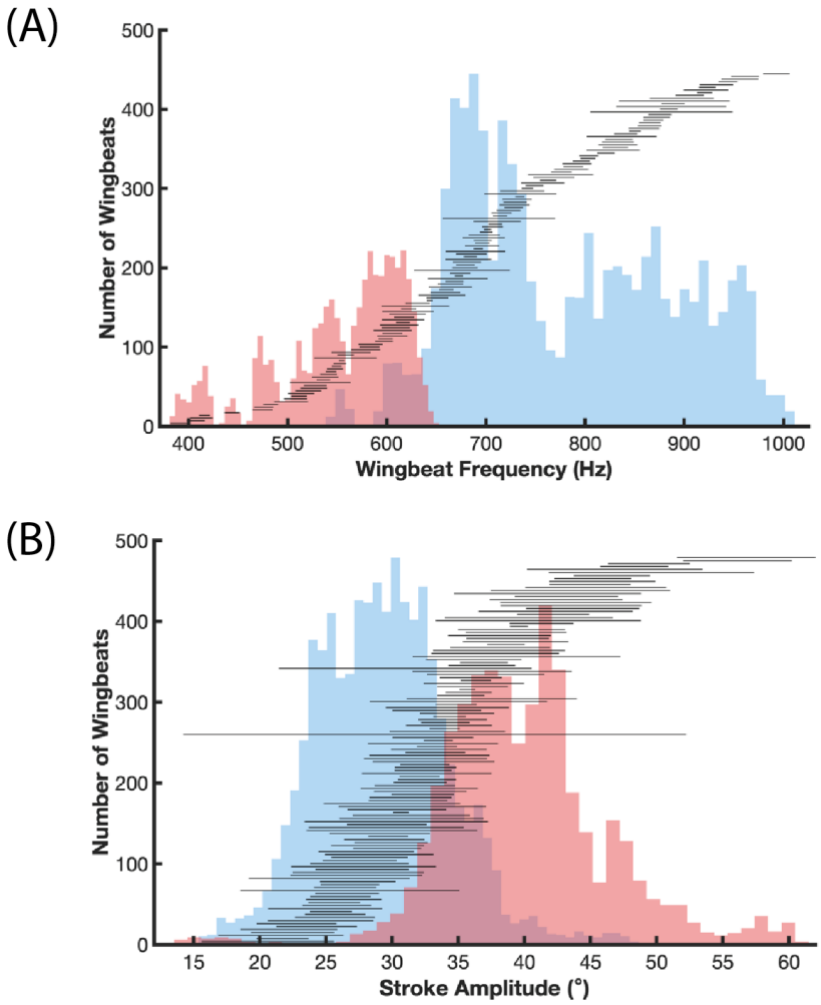

Figure 3.6 Histogram of summary kinematic parameters

(A) Wingbeat frequency and (B) stroke amplitude histogram. Blue is males, red is females, and the black horizontal lines represent individuals ranked according to their mean (*N* = 8,073 male wingbeats and *N* = 4,505 female wingbeats).

3.3.1 Mosquito Metrics

3.3.1.1 Wing, Body and Legs

Body length and wing length positively correlated with one another in males (N = 90, R^2 = 0.781 and P < 0.001) and females (N = 39, R^2 = 0.663 and P < 0.001) (**Figure 3.7 and Table 3.1**). Whereas, wing length and wingbeat frequency poorly correlated in both males (R^2 = 0.0295 and P = 0.108) and females (R^2 = 0.0193 and P = 0.392) (**Figure 3.8**).

Limb mass, whole limb length, and leg segment lengths and radii measurements are summarised in **Table 3.1**. Leg mass made up to 5 – 6 % of body mass as fore-, mid- and hind-limb mass was $1.038 \times 10^{-5} \pm 2.118 \times 10^{-6}$ g (N = 60 legs, mean ± SD), $8.25 \times 10^{-6} \pm 1.52 \times 10^{-6}$ g (N = 53 legs) and $7.49 \times 10^{-6} \pm 6.15 \times 10^{-7}$ (N = 53 legs) respectfully. While, fore-, mid- and hind-limb length was 5.352 ± 0.168mm , 6.473 ± 0.156 mm and 7.760 ± 0.644 mm respectfully (N = 10 each). Meanwhile, the ratio between the femur, tibia and tarsus was also found to be 0.26 : 0.33 : 0.41, 0.27 : 0.29 : 0.44, and 0.23 : 0.25 : 0.53 for the fore-, mid- and hind-limb respectfully. Tarsus length of the hind-limb was therefore particularly notable, as it was approximately two times greater than its femur and tibia length.

In total N = 6 individuals of mixed sex from multiple hanging points were used to calculate the COM. The COM was positioned 37 ± 6 % (mean ± SD) along the

bodies length from the proboscis base (nose), at the thorax and abdomen junction as illustrated in **Figure 3.9**.

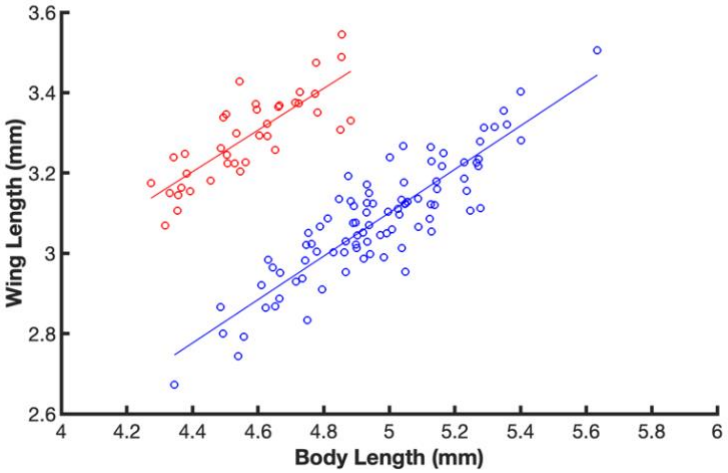

Figure 3.7 Mosquito body length and wing length

Males in blue and females in red. Equation of the linear trendline was y = 0.54x + 0.4 for the males (N = 90, R^2 = 0.781 and P < 0.001) and y = 0.52x + 0.92 for the females (N = 39, R^2 = 0.663 and P < 0.001).

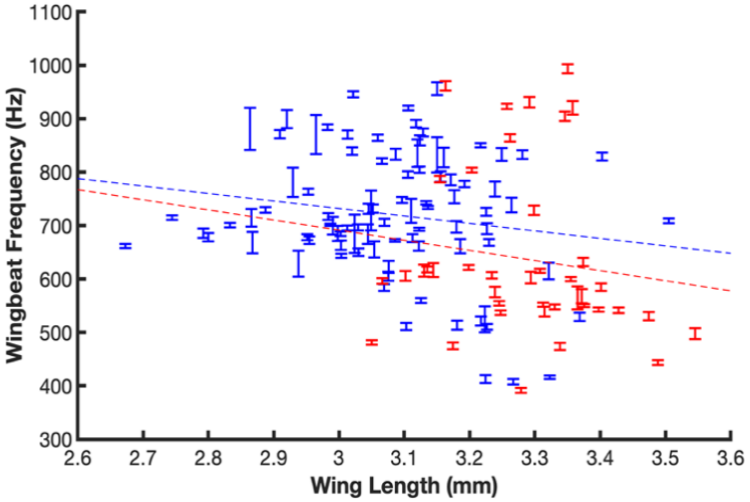

Figure 3.8 Wing length versus wingbeat frequency

Males in blue (N = 90, R^2 = 0.0295 and P = 0.108) and females in red (N = 39, R^2 = 0.0193 and P = 0.392). Vertical bars denote the mean and standard deviation of each mosquito recorded.

Table 3.1 Mosquito morphological parameters: body, wings, and legs

Parameter	Male	Female
Body Length (mm)	4.96 ± 0.25	4.57 ± 0.17
Wing Length (mm)	3.08 ± 0.14	3.30 ± 0.11

Parameter	Length (mm)	Radius (mm)	Mass (g)
Forelimb	5.352 ± 0.168	-	$1.038 \times 10^{-5} \pm 2.118 \times 10^{-6}$
Femur	1.388 ± 0.025	0.0458 ± 0.0081	2.693×10^{-6} *
Tibia	1.760 ± 0.108	0.0317 ± 0.0052	3.415×10^{-6} *
Tarsus	2.204 ± 0.191	0.0186 ± 0.0041	4.276×10^{-6} *
Midlimb	6.473 ± 0.156	-	$8.25 \times 10^{-6} \pm 1.52 \times 10^{-6}$
Femur	1.729 ± 0.0169	0.0378 ± 0.0069	2.202×10^{-6} *
Tibia	1.872 ± 0.0772	0.0235 ± 0.0040	2.385×10^{-6} *
Tarsus	2.872 ± 0.138	0.0196 ± 0.0040	3.658×10^{-6} *
Hindlimb	7.760 ± 0.644	-	$7.49 \times 10^{-6} \pm 6.15 \times 10^{-7}$
Femur	1.757 ± 0.0819	0.0316 ± 0.0044	1.696×10^{-6} *
Tibia	1.905 ± 0.0997	0.0183 ± 0.0035	1.839×10^{-6} *
Tarsus	4.097 ± 0.529	0.0171 ± 0.0034	3.955×10^{-6} *

Values are in the format of mean $\pm$ SD. * estimated.

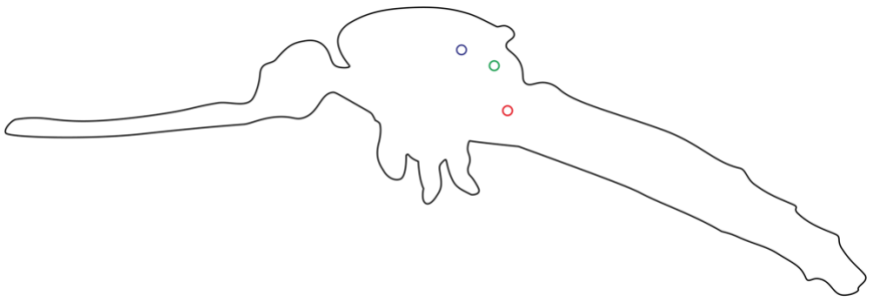

Figure 3.9 Mosquito centre of mass position

Wing base (blue), haltere base (green) and centre of mass (red).

3.3.1.2 Body and Leg Moment of Inertia

Table 3.2 summarises the MOI results of all mosquito bodies and legs from subjects with all six legs present (intact mosquitoes in *N* = 103 sequences). The total leg MOI for subjects with all six legs, was found to be ~ 55 % of total body MOI in the roll axis for both male and female mosquitoes. The ratio of which the fore-, mid- and fore-limbs contributed to the total MOI of the legs was 0.28 : 0.46 : 0.26 respectfully. Meanwhile, the MOI of leg segments (femur, tibia and tarsus) approximately contributed to the whole leg by 0.61 : 0.29 : 0.1, 0.60 : 0.23 : 0.16, and 0.61 : 0.21 : 0.18 for the fore-, mid- and hind-limb respectfully.

Table 3.2 Moment of inertia mosquito body and leg results

Parameter	Male	Female
Body MOI in roll axis ($kg \cdot m^2$)	$8.954 \times 10^{-13} \pm 1.739 \times 10^{-13}$	$6.560 \times 10^{-13} \pm 1.091 \times 10^{-13}$

Parameter	Moment of Inertia ($kg \cdot m^2$)
All 6 legs	$4.277 \times 10^{-13} \pm 7.576 \times 10^{-14}$
Forelimb	$5.996 \times 10^{-14} \pm 1.524 \times 10^{-14}$
Femur	$2.178 \times 10^{-19} \pm 1.445 \times 10^{-34}$
Tibia	$1.043 \times 10^{-19} \pm 1.204 \times 10^{-33}$
Tarsus	$3.592 \times 10^{-20} \pm 1.174 \times 10^{-33}$
Midlimb	$9.928 \times 10^{-14} \pm 1.664 \times 10^{-14}$
Femur	$1.178 \times 10^{-19} \pm 3.636 \times 10^{-33}$
Tibia	$4.554 \times 10^{-20} \pm 1.806 \times 10^{-35}$
Tarsus	$3.168 \times 10^{-20} \pm 4.574 \times 10^{-34}$
Hindlimb	$5.593 \times 10^{-14} \pm 3.300 \times 10^{-14}$
Femur	$7.480 \times 10^{-20} \pm 8.668 \times 10^{-34}$
Tibia	$2.509 \times 10^{-20} \pm 2.558 \times 10^{-34}$
Tarsus	$2.190 \times 10^{-20} \pm 8.968 \times 10^{-34}$

Moment of inertia (MOI). Values are in the format of mean ± SD.

3.3.2 High-precision Wing Kinematics

Wingtip (stroke angle and deviation angle) and mid-wing pitch kinematics over time were stereotypical to what I would expect in a reciprocal wingbeat (**Figure 3.10A - C**). That is directional changes when flapping and morphological flipping during stroke reversal (ventrally when transitioning to the upstroke and dorsally to downstroke). Stroke angle and deviation angle had near sinusoidal traces as were defined relative to the body plane. A negative mid-wing pitch angle (taken from mid-way along the wing length) was the result of the axis system used rather than a negative aerodynamic angle of attack. As an angle of attack, is further dependent on the vector of the wing and surrounding air movement. Mid-wing pitch angle was approximately symmetrical on the upstroke and downstroke (inverted) as expected as the wing must quickly bound between wingtip position extremes when flapping (**Figure 3.10C**). A subtle recoil can also be seen at the end of each stroke reversal likely owed to elastic components (Ishihara and Horie, 2017). Absolute high mid-wing pitch angles were not sustained in the middle of each half stroke. Wing twist gradient and spanwise bending have a similar peak and trough pattern which remains the same for each wingbeat through the stroke (**Figure 3.10D** and **E**). As the wing twists, it bends in the spanwise direction and vice versa (untwists). Local maximum and minimum values for all kinematic parameters (per wingbeat) described above were significantly different between the males and females ($P < 0.001$).

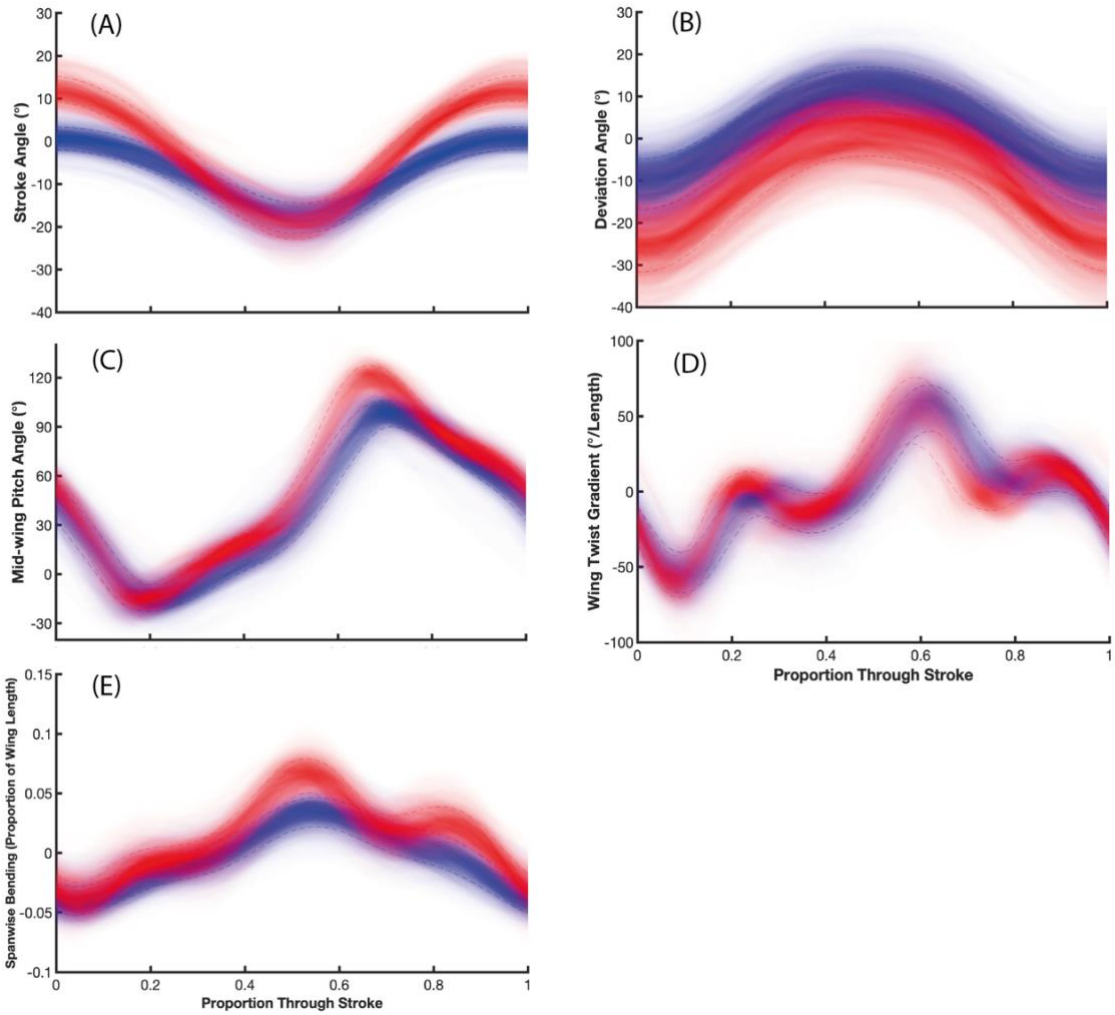

Figure 3.10 Frequency density plots of wing kinematics

(A) Stroke angle, (B) deviation angle, (C) mid-wing pitch angle, (D) wing twist gradient and (E) spanwise bending proportion through the stroke for *N* = 25,156 wingbeats (sum of left and right wings, *N* = 16,146 male wingbeats and *N* = 9,010 female wingbeats). Male (blue) and female (red). Dotted lines are ± 1 standard deviation of the mean.

3.3.3 Leg Kinematics

To remain undetected by prey, mosquitoes have long narrow limbs to minimise surface contact area, whilst maximising their contact time, and minimising their ground reaction force when landing or taking off from surfaces (Muijres et al., 2017). It is therefore common for mosquitoes to experience leg loss when being handled (e.g., with a pooter or during transit) and taking off from textured or adhesive surfaces such as those statically charged (e.g., the flight arena). That being said, mosquito leg loss is thus also likely to occur in nature, as frequently reported amongst other insect species due to injury, lack of energetic reserves and predation (Escalante and Elias, 2021, Maginnis, 2006). In this results section, I thereby report standard leg kinematics from mosquitoes with all limbs intact first before reporting the leg kinematics of mosquitoes that had experienced leg loss.

3.3.3.1 Standard Leg Kinematics

The typical leg posture of mosquitoes can be seen in **Figure 3.11A,** where the forelimbs were positioned anteriorly, midlimbs laterally, and hindlimbs posteriorly. For all leg kinematics (swing, elevation and tilt), the interquartile range of limbs on the contralateral sides of one another (e.g., L2 and R2) were generally positioned similarly (**Figure 3.11B - D**). Meanwhile, forelimb (L1 and R1) swing and elevation angle operated at generally tighter ranges than the mid- and hindlimbs. For the remaining leg kinematics, the variation in maximum and minimum values may be owed to more significant manoeuvres of intact

individuals. However, the large range in tilt angle (**Figure 3.11D**) was due to a tracking issue when elevation angle approached zero, as elevation angle can be positive or negative. Statistical analysis of tilt angle was therefore excluded from here on as tilt results cannot be easily compared, and was justified as leg tip position is only determined by swing and elevation of the leg.

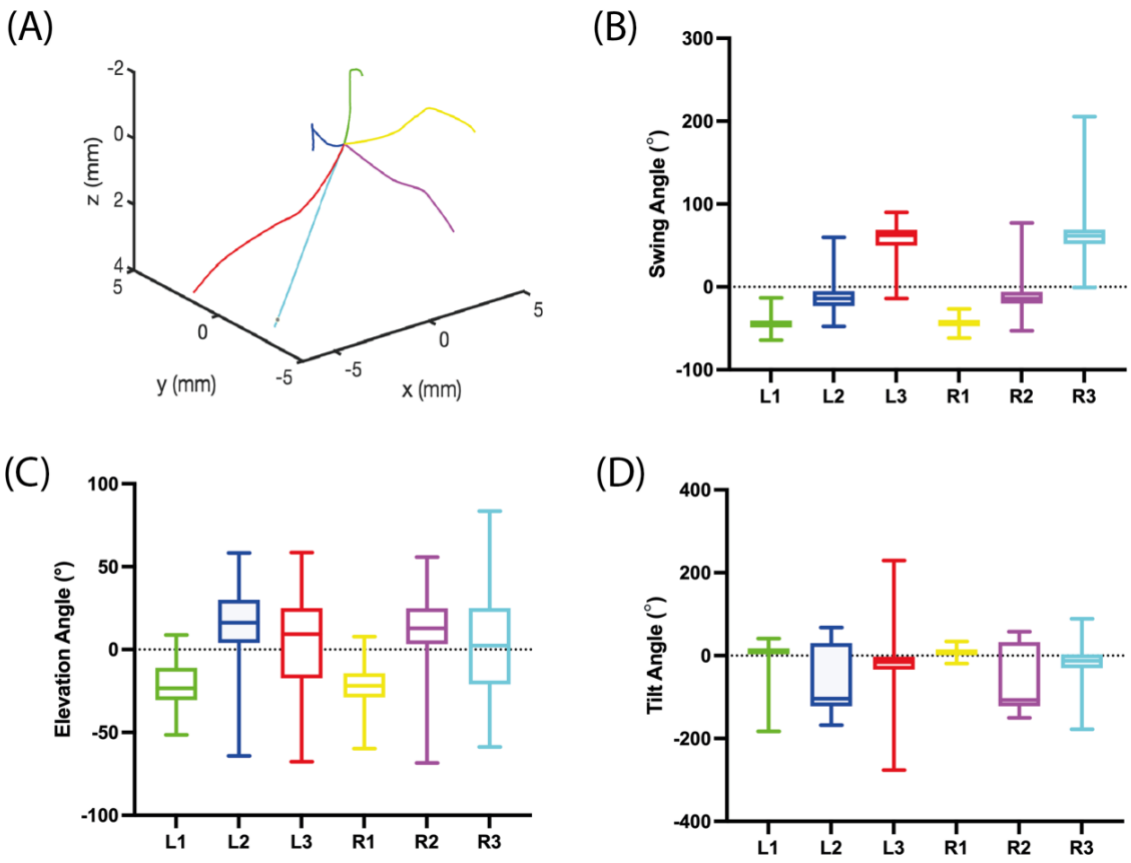

Figure 3.11 Summary of standard mosquito leg kinematics

(A) Typical posture of mosquitoes' legs. Forelimbs were positioned anteriorly (in green and yellow), midlimbs laterally (blue and magenta), and hindlimbs posteriorly (red and cyan). Boxplots displaying (B) swing angle, (C) elevation angle and (D) tilt angle of all legs in intact mosquitoes. For all figure parts, L1 (green), L2 (blue), and L3 (red) are left legs and R1 (yellow), R2 (magenta) and R3 (cyan) are right legs.

3.3.3.2 Effect of Leg Loss

Out of the 129 mosquitoes recorded, 89 experienced leg loss at varying degrees (89 out of total 195 sequences recorded). In these sequences featuring leg loss, L1 was absent for 1.7 %, L2 for 5 %, L3 for 35.8 %, R1 for 10.8 %, R2 for 8.3 % and R3 for 38.3 % (**Figure 3.12)**. This was then identified as nine balanced combinations (conditions) described in **Table 3.3**. The hindlimbs (one or both only) were therefore the most frequently lost making up 66 % of sequences (59 sequences) featuring any leg loss. I thereby focused on the leg kinematics of the fully intact (have all six legs, Group 9) and those with compromised hindlimbs only (Group 2 and 4) during free-flight, as they were most biologically relevant. Limb detachment in the hindlimb position was most likely to occur as they are the most tapered and have been identified to be the last to leave the surface when taking off (Smith et al., 2018). Sequences were treated independently as leg loss was progressive for some individuals where more than one flight sequence was obtained. In total, no leg kinematics were obtained from just three sequences (out of the 195) as complete legs were out of view in more than six high-speed cameras. All leg kinematics (swing, elevation and tilt) when normalised by wingbeat, remained relatively stable through the stroke but were likely positioned soon after take-off for optimum stability which was not captured in footage.

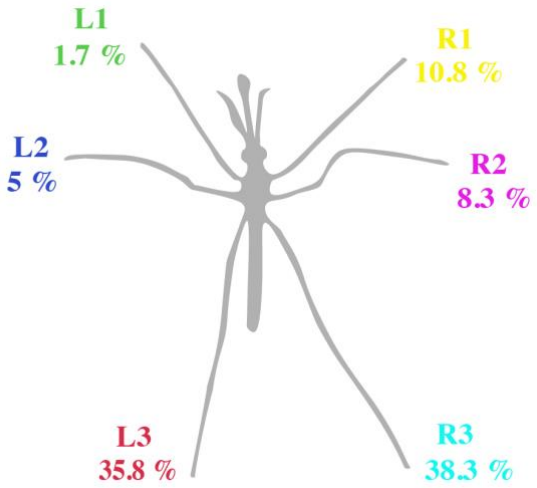

Figure 3.12 Percentage of leg loss

Percentage of limb loss out of the 89 sequences featuring limb damage (e.g., 1.7 % of the 89 sequences experienced L1 limb loss).

Table 3.3 Mosquito leg loss combinations

Group	Limb Missing	Sequences
1	L1, L3 and R3	3
2	L3 or R3	39
3	L3 R2 or L2 R3	7
4	L3 and R3	20
5	L2, L3 and R2	1
6	R1 and R2	2
7	L1 or R1	13
8	L2 or R2	4
9	No limbs missing	103

L1 – 3 are left legs and R1 - 3 are right legs. Fore-limbs (L1 and R1), mid-limbs (L2 and R2), and hind-limbs (L3 and R3).

To investigate the effect of hindlimb leg loss on the remaining leg kinematics, a Kruskal-Wallis test was conducted to determine if there was a significant effect amongst the three unique leg combinations between the same legs present. All results can be seen in **Table 3.4** and **3.5,** and depicted in boxplot **Figures 3.13** and **3.14.**

Swing angle and elevation angle was significantly different for all legs amongst the groups via Kruskal-Wallis (dof = 3, $P < 0.0001$, see **Table 3.4 and 3.5** for all H values). A subsequent Dunn's procedure with Bonferroni correction then confirmed this, for instance swing angle of Group 9's (subjects will all six limbs present) L1 was significantly different to Group 2's (L3 or R3 missing) L1 ($P < 0.0001$), and to Group 4's (L3 and R3 missing) L1 swing angle ($P < 0.0001$). Likewise, Group 2's L1 and Group 4's L1 swing angle was significantly different ($P < 0.0001$). Similar results were obtained between all comparisons including Mann-Whitney U test results ($P < 0.0001$ but $P = 0.0011$ for Groups 2 and 9 R3 elevation angle comparison) with a few exceptions outlined below in elevation angle.

Overall, limb loss affected the swing angle of remaining limbs the most. Group 4 with no hindlimbs increased their forelimb elevation angles ($P < 0.0001$), meanwhile those with only one missing hindlimb compared to those fully intact did not ($P = 0.5055$). Additionally, Group 4's L2 and R1 elevation angle was not significantly different from their fully intact counterparts ($P = 0.625$ and $P = 0.875$ respectfully).

In summary, when one hindlimb was missing, the ipsilateral mid-leg tended to increase its swing angle by ~ 10 ° and elevation angle by ~ 3 ° which may help compensate for the imbalance. Whereas when both hindlimbs were missing, ipsilateral midlimbs tended to increase their swing angle by ~ 23 °. When one hindlimb was missing, the remaining hindlimb increased its swing angle by ~ 10 ° and decreased its elevation angle by ~ 4 °. Meanwhile, if one or both hindlimbs were missing, swing angle of the forelimbs in both groups increased similarly by ~ 2 °.

Table 3.4 Kruskal-Wallis test results for leg swing angle

	Swing Angle					
Leg	L1	L2	L3	R1	R2	R3
H	919.8	3019	-	108.2	1591	-
dof	3	3	2	3	3	2
P-value	< 0.0001	< 0.0001	< 0.0001	< 0.0001	< 0.0001	< 0.0001

Comparisons	Mean rank diff.	Significance	Adjusted *P* Value
L1_GP9 vs. L1_GP2	-1164	****	<0.0001
L1_GP9 vs. L1_GP4	-2416	****	<0.0001
L1_GP2 vs. L1_GP4	-1251	****	<0.0001
L2_GP9 vs. L2_GP2	-1979	****	<0.0001
L2_GP9 vs. L2_GP4	-4513	****	<0.0001
L2_GP2 vs. L2_GP4	-2534	****	<0.0001
L3_GP2 vs. L3_GP9	-	****	<0.0001
R1_GP9 vs. R1_GP2	-465.9	****	<0.0001
R1_GP9 vs. R1_GP4	-772.7	****	<0.0001
R1_GP2 vs. R1_GP4	-306.8	**	0.0037
R2_GP9 vs. R2_GP2	-1948	****	<0.0001
R2_GP9 vs. R2_GP4	-3118	****	<0.0001
R2_GP2 vs. R2_GP4	-1170	****	<0.0001
R3_GP2 vs. R3_GP9	-	****	<0.0001

Degrees of freedom (dof), no significance (ns) $P > 0.05$, * $P \leq 0.05$, ** $P \leq 0.01$, *** $P \leq 0.001$ and **** $P \leq 0.0001$.

Table 3.5 Kruskal-Wallis test results for leg elevation angle

	Elevation Angle					
Leg	L1	L2	L3	R1	R2	R3
H	225.5	9814	-	19.86	100.6	-
dof	3	3	2	3	3	2
P-value	< 0.0001	< 0.0001	< 0.0001	< 0.0001	< 0.0001	0.0011

Comparisons	Mean rank diff.	Significance	Adjusted *P* Value
L1_GP9 vs. L1_GP2	-95.73	ns	0.5055
L1_GP9 vs. L1_GP4	-1263	****	<0.0001
L1_GP2 vs. L1_GP4	-1167	****	<0.0001
L2_GP9 vs. L2_GP2	-256.2	***	0.0005
L2_GP9 vs. L2_GP4	109.3	ns	0.625
L2_GP2 vs. L2_GP4	365.5	***	0.0006
L3_GP2 vs. L3_GP9	-	****	<0.0001
R1_GP9 vs. R1_GP2	271.4	***	0.0002
R1_GP9 vs. R1_GP4	-88.3	ns	0.872
R1_GP2 vs. R1_GP4	-359.7	***	0.0004
R2_GP9 vs. R2_GP2	-274	****	<0.0001
R2_GP9 vs. R2_GP4	-955.3	****	<0.0001
R2_GP2 vs. R2_GP4	-681.3	****	<0.0001
R3_GP2 vs. R3_GP9	-	**	0.0011

No significance (ns) $P > 0.05$, * $P \leq 0.05$, ** $P \leq 0.01$, *** $P \leq 0.001$ and **** $P \leq 0.0001$.

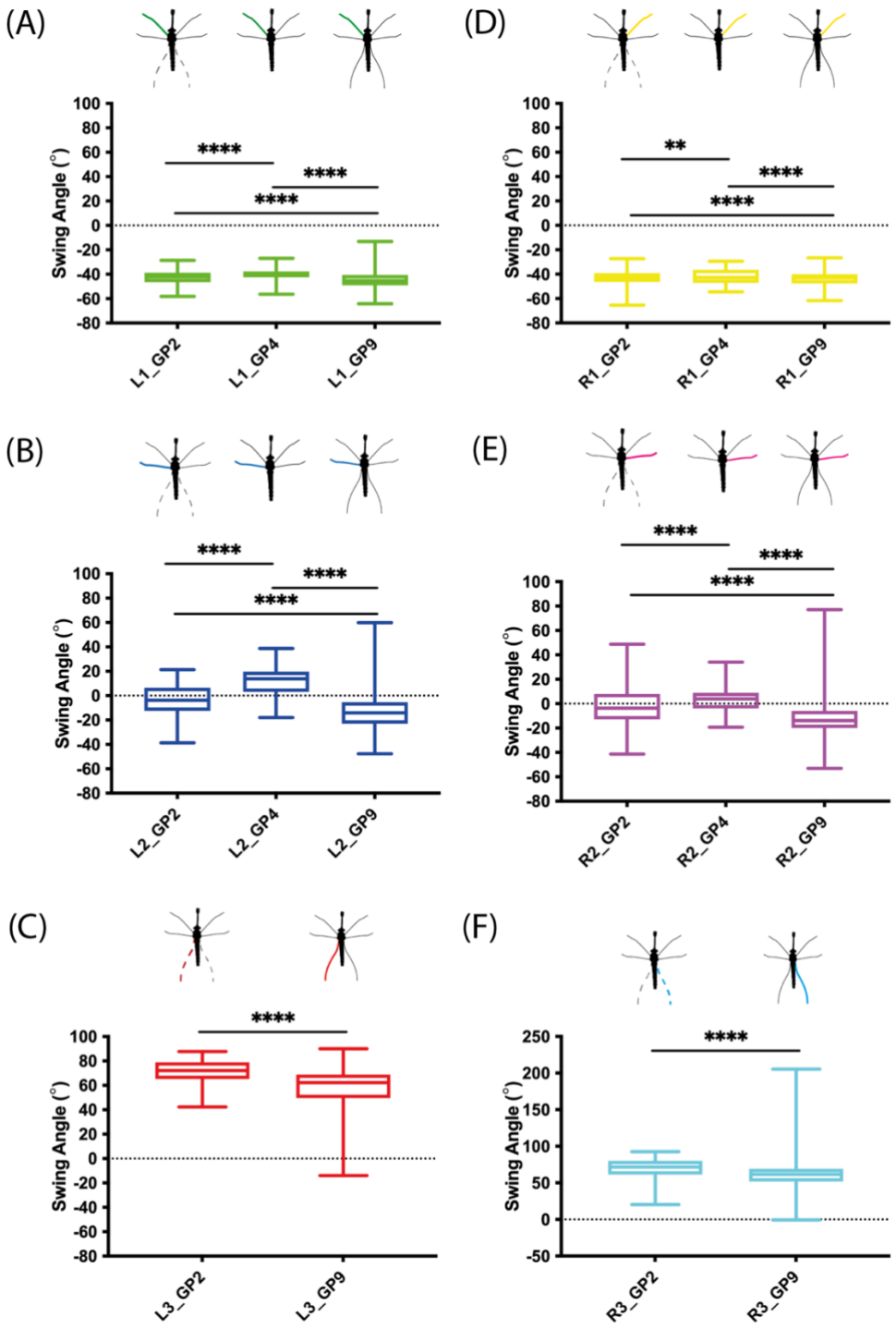

Figure 3.13 Swing angle box plots

Swing angle multiple comparisons between Groups 2, 4 and 9 for all legs present. (A) L1 comparisons in green, (B) L2 comparisons in blue, (C) L3 comparisons in red, (D) R1 comparisons in yellow, (E) R2 comparisons in magenta and (F) R3 comparisons in cyan. Mosquito schematics above each boxplot further indicate which group is being compared. No significance (ns) $P > 0.05$, * $P \leq 0.05$, ** $P \leq 0.01$, *** $P \leq 0.001$ and **** $P \leq 0.0001$.

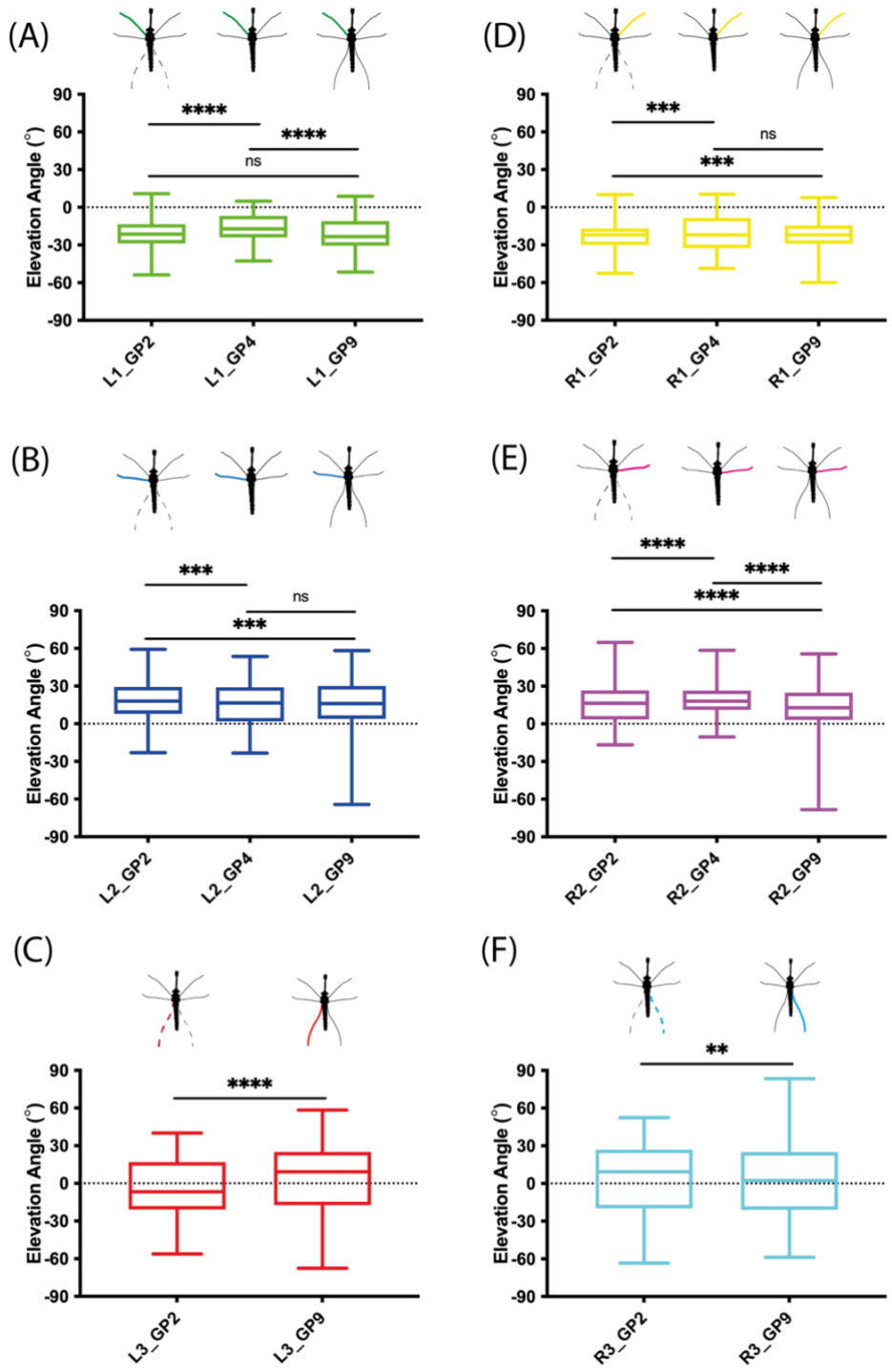

Figure 3.14 Elevation angle box plots

Elevation angle multiple comparisons between Groups 2, 4 and 9 for all legs present. (A) L1 comparisons in green, (B) L2 comparisons in blue, (C) L3 comparisons in red, (D) R1 comparisons in yellow, (E) R2 comparisons in magenta and (F) R3 comparisons in cyan. Mosquito schematics above each boxplot further indicate which group is being compared. No significance (ns) $P > 0.05$, * $P \leq 0.05$, ** $P \leq 0.01$, *** $P \leq 0.001$ and **** $P \leq 0.0001$.

To test the effect of uneven ipsilateral leg loss (between left and right body sides) on body roll, average body roll of sequences was calculated then grouped according to the number of uneven ipsilateral legs lost, and significance tested using a non-parametric Mann-Whitney *U* test (**Figure 3.15**). All comparisons between groups with two left limbs more than the right side ($N = 4$, $P = 0.565$), with one left limb more than the right side ($N = 34$, $P = 0.104$), with one right limb more than the left side ($N = 25$, $P = 0.657$) and with two right limbs more than the left side ($N = 2$, $P = 0.681$), against the group with an equal number of left and right legs ($N = 127$ mosquitoes with all six limbs) were not significant.

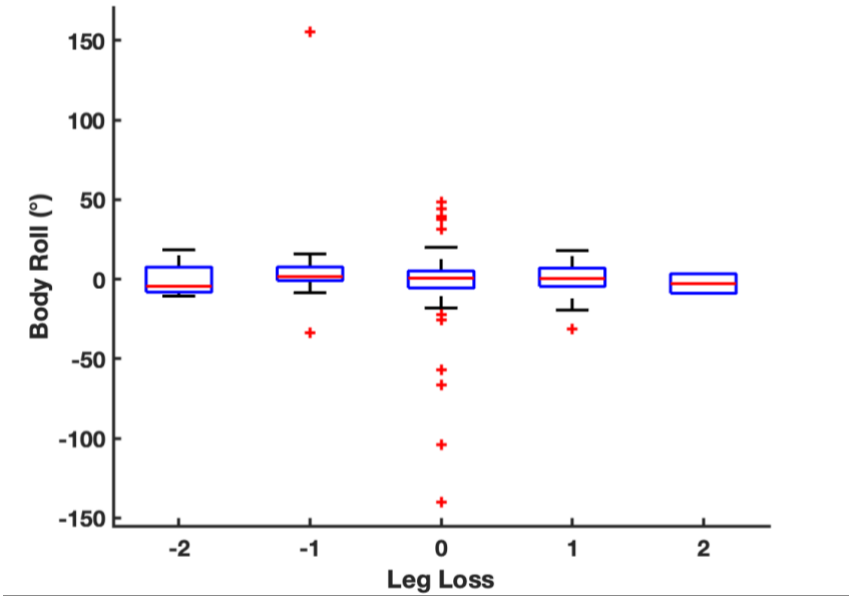

Figure 3.15 Effect of leg loss on body roll

In the x-axis, negative numbered leg loss groups (-2 and -1 (*N* = 4 and *N* = 34 sequences respectfully)) denote a greater number of left legs present and positive leg loss groups (1 and 2 (*N* = 25 and *N* = 2 sequences respectfully)) denote a greater number of right legs present. For example, a mosquito with 1 right leg and 2 left legs will be categorised in -1 (1 – 2 = -1). Leg loss group 0 (*N* = 127 sequences) signifies an equal number of left and right legs present in the mosquito. In the y-axis, body roll is the mean body roll for a given sequence (*N* = 192 total sequences). Box plot whiskers are 5 – 95 percentiles and red plus signs are outliers.

3.4 Discussion

Mosquitoes are morphologically and aerodynamically interesting, with their high aspect ratio wings, high wingbeat frequencies, and shallow stroke amplitudes which enable them to use TEV that remains exclusive to them, and rotational drag to generate the majority of their lift force (Bomphrey et al., 2017). The characteristics described above thereby make it difficult for researchers, as it highlights the limitations of experimental setups, for instance their ability to record long sequences, trade-offs between image resolution and frame rate, limited number of camera views, and computational power. Although imaging techniques have advanced in recent years, surprisingly little is known on how they perform impressive flight manoeuvres from a kinematic and aerodynamic perspective. Thus, the aim of this study was to generate a large database of high-precision wing and body kinematics of *Anopheles* during free-flight, using a ten high-speed camera rig and the subsequent footage subject to a quick and automated high-precision kinematic acquisition technique. To complement this, leg kinematics that have previously been shown to fine-tune flight performance, and actions taken when compensating for leg loss were also reported for the first time in such detail.

3.4.1 Mosquito Metrics

Body length scaled with wing length in all mosquitoes alike in most flying insects (Grimaldi and Engel, 2005). This relationship would have remained true if included sex specific morphological features such as males having bushed antennae and a longer proboscis (Sallum et al., 2020, Wheelwright et al., 2021). However for both sexes, features beyond the proboscis base (nose) were not included in analysis as: they were positioned densely in one area making it difficult to voxel carve accurately, were not useful for calculating the COM as warped following anaesthesia (nose to thorax is better as it is more of a straight line), and may have introduced complications in getting body roll in the automated tracker where rotation was calculated by assuming an enclosed triangle within the body. Furthermore, the mass of these features were unlikely to considerably contribute to overall body mass as the antennae (only covered in thin hairs for acoustic sensitivity), maxillary palps and proboscis (hollow tube) are long narrow features (Dixon and Vondra, 2022, Wheelwright et al., 2021).

Conversely, the poor relationship between wing length and wingbeat frequency was unexpected (Tercel et al., 2018). Longer wings typically equate to heavier bodies that require greater forces for weight support, which may be accomplished by the insect flapping faster or possessing larger surface area wings (Kim et al., 2021, Miller, 1977). One possible explanation, could be the varying ambient temperature during data collection, that will also be addressed in the next experimental chapter of this thesis (Sotavalta, 1952, Villarreal et al., 2017). Underlying direct asynchronous flight muscle may operate at different

temperature dependent optimums or natural contraction frequencies, but this is yet to be verified in mosquitoes. However, it has been described in literature that some insects require additional time to warm up their flight muscles, particularly in cold environments before taking off. Large flight muscles within the thorax (**Section 1.5**) are able to collectively contract to generate heat, momentarily de-coupling themselves from the wing movement they usually drive (Heinrich, 1974). Western honeybees for instance, have a peak warm up rate of 9.3 °C per minute and maintained a 32.5 °C thoracic temperature during flight within a 22 °C environment (Heinrich, 1979, Stone and Willmer, 1989). Whilst swarming honey bees only took off after their thoraxes reached a minimum of 35 °C (Seeley et al., 2003). This idea has been further observed in invertebrate and vertebrate synchronous muscle as molecular mechanisms are more malleable and receptive to stimulation (Olberding and Deban, 2017, Josephson and Young, 1985). Josephson and Young (1985) found that the normal operating frequency (550 Hz) of the synchronous tymbal muscle in cicada was only achieved between 40 and 45 °C whilst the ambient temperature during singing was 28 - 35 °C.

The position of ones COM could be telling of its flight agility, and may be defined as the point of which mass in all directions is balanced. The COM of insects is typically centred around the wing hinge for sensitivity to aerodynamic torques generated by the wings or haltere base for registering body rotation. For instance, the COM of droneflies overlays its haltere base whereas the COM in blowflies is above the wing base and haltere base (Huntley et al., unpublished). The position of the mosquito's COM was therefore unsurprising between the thorax and abdomen but may be a further reflection of their anatomically long abdomens and

feeding habits, where females can double or triple their body mass after a blood meal and need to depart from game undetected (van Veen et al., 2020).

To complement calculations of the MOI, body sections may have been cut up and weighed independently however, this was deemed unsuitable as small insects are prone to crushing and dehydration (Mellanby and Haldane, 1934). The MOI of the body and legs relative to the centre of mass was therefore estimated using an insect model similarly to (Hedrick and Daniel, 2006, Mountcastle et al., 2015) but from microscope images that were then scaled. Mosquito legs were also modelled as a series of spheres to reduce complications with modelling the limbs around the bodies roll axis as three cylinders to represent the femur, tibia, and tarsus at different positions and orientations. The total MOI of mosquito legs was considerably high being ~ 55 % of the body's MOI around its roll axis. This was a similar result reported for orchid bees, where hind leg extension increased their MOI in the roll axis by more than 50 % (tucked 3.65×10^{-10} kg·m^2 versus extended 5.60×10^{-10} kg·m^2), thus indicating that limbs may play a large role in flight stability across many different insect species (Combes and Dudley, 2009a).

3.4.2 Wing Kinematics

A large number of publications describe insect wing and body kinematics however, these predominantly only report stroke, deviation and wing pitch angle do not fully enclose wing torsion. Wing twist gradient and spanwise bending only

previously applied to hoverflies and locusts in Walker et al (2009) and subsequent papers, are relatively new wing kinematic parameters to help capture deformation. The description of any large differences between wing twist from root to tip and spanwise bending are thus likely to be important aerodynamically when modelling and comparing flight efficiency amongst different insect species (Walker et al., 2008). Previous studies were likely unable to calculate these parameters due to limited spatiotemporal resolution, and video processing techniques which were two of the fundamental objectives when developing the ten high-speed free-flight arena camera rig (**Section 2.2**). Walker et al. (2019) was also the first to incorporate wing twist into an updated blade element model for stroke averaged forces. Although applying blade element theory (BET) to mosquito wing kinematics is prone to over or underestimate force production, due to BET quasi-steady state assumptions (time history is assumed unimportant) and dominating rotational phases. Incorporating these mosquito kinematics into a computational fluid dynamic (CFD) model would thus be more appropriate.

Wing twist gradient and spanwise bending peaked several times through the stroke denoting a persistent change in behaviour. This is likely to be the passive outcome of the shift in rotational axis along the wing from the leading to trailing edge utilised in rotational drag and of great importance in mosquitoes when bounding between stroke reversals at high wingbeat frequencies, however, this is yet to be fully understood. If assuming a flat plate wing in *Anopheles*, alike in previous studies featuring *Drosophila* wings (e.g., (Faruque and Sean Humbert, 2010, Fry et al., 2005)) that operate at similar scales, may thereby produce inaccurate findings. It should also be noted that spanwise bending and chordwise camber are different for reason that chordwise camber requires knowledge and

incorporation of detail on wing veins and junctions (topographic measurements) that restrain flexion along the wing (Walker et al., 2009).

Mid-wing pitch (wing pitch at mid-wing length) was plotted as it were likely to encase the most kinematic detail required for rotational and brief LEVs force production about its chord, and experience the greatest added mass effect (Walker and Taylor, 2021). Sustaining high (absolute) mid-wing pitch angle was not prioritised as expected, presenting as transient peak during stroke reversal during middle of each half stroke, unlike other species that rely on LEV (where wing pitch follows a ‘W’ shape with greater recoil after stroke reversal (Dickinson and Muijres, 2016)). Further investigation of the mosquito wing hinge and steering muscle properties used to achieve such fast rotations and little recoil would be interesting, but could prove difficult *in vivo* due to its operating speed alone.

The highest wingbeat frequency was 1,015 Hz from a male mosquito (recorded at 35.2 °C and 20.7 % humidity) and the lowest stroke amplitude observed was 12.9 ° from a female sequence (recorded at 30.9 °C and 31.9 % humidity). This low stroke amplitude was further verified by checking raw footage where the female mosquito was seen to quickly descend following stimuli, thereby requiring less weight support. Furthermore, this low stroke amplitude (12.9 °) was notably lower than the smallest stroke amplitude reported to date in the *Culex* mosquito at 44 ° (fruit fly 140 ° and hawkmoth 116 ° (Bomphrey et al., 2017)). Acquiring more extreme manoeuvres may have been achieved by using a mechanical swatter similarly to Cribellier et al. (2022). However, subtracting artefacts

introduced by air flow produced by the swatter that may have gusted the mosquito away was not controlled for in (Cribellier et al., 2022).

3.4.3 Leg Kinematics

In this study I showed that intact mosquitoes generally position their left and right limbs similarly, whilst mosquitoes experiencing hindlimb lost significantly adjusted their remaining leg kinematics. This was consistently significantly different for all kinematic parameters between hindlimbs and for all swing angles of all legs. Mosquito midlimbs (L2 and R2) were also identified to contribute to approximately half the total MOI of limbs, and may therefore have the greatest effect/influence on adjustments made to the total leg MOI when experiencing leg loss. Though, to what extent the kinematic adjustments made of remaining limbs effect on MOI, and contribution to flight stability is still unclear.

A lower MOI on one side of an insect's body that has not been compensated for means it requires a lower torque to accelerate about the body's rotational axis, favouring manoeuvrability in the same roll direction and overall flight efficiency if the flight behaviour is repetitive. It therefore makes sense that insects would choose energetically cheaper techniques of stabilisation in the axes where possible rather than expensive ones i.e., actively changing wing kinematics for corrective torques. On the other hand, deliberately increasing a leg's moment of inertia can improve stability when subject to turbulence. In the past, mosquitoes

have been found to spread their legs alike in bumblebees to increase their MOI to reduce disturbances by 11 % when hovering (Liu and Sun, 2019, Combes and Dudley, 2009b). The relationship between mosquito leg and body MOI in this study were comparable to those previously reported in orchid bees (> 50 % (Combes and Dudley, 2009b)). Although this was considerably higher than the ~ 6 % increase previously reported in *Drosophila* (with hindlimb extension), that is likely to be explained by anatomical differences such as body size and leg position (Berthé and Lehmann, 2015).

Finally, the non-significant result between the body roll and groups of ipsilateral leg loss may denote that damaged mosquitoes with an uneven number of ipsilateral limbs were able to adjust their kinematics to effectively manage their body roll, or differences were too small to measure.

3.5 Conclusion

The outcomes of this current study provide a new standard for kinematics acquisition and highlights the importance of non-wing appendages in insect flight stability. Kinematics were acquired using a new high-speed camera rig that enabled and accelerated to my knowledge, the generation of the second largest database of high-precision insect free-flight kinematics to date; by addressing challenges faced in previous experimental designs. For instance, automating the previously laborious and time-consuming task of tracking wing tip positions frame by frame. The improved specifications of recorded sequences further permitted the definition of additional and relatively new descriptors of 3D wing motion, wing torsion and wing bending (Walker et al., 2009, Walker and Taylor, 2021). The lowest stroke amplitude observed was notably smaller than any flying insect in literature, likely due to manoeuvre variation/aerodynamic force demand and environmental factors such as ambient temperature which is further discussed in **Chapter 4**. Wingtip and wing pitch parameters were also significantly different between male and females, likely due to a combination of factors e.g., morphological differences and feeding habits. Finally, in-depth leg kinematics defined as swing and elevation angle were reported for the first time within a flying insect, damaged individuals were shown to adjust their leg kinematics in response to leg loss, and the leg moment of inertia of intact subjects was found to contribute largely to flight stability in the roll axis. The findings of this chapter therefore continue to incite interest in what is occurring aerodynamically during manoeuvres, and how this is achieved mechanically in *Anopheles*. As well as encourages future studies to consider, include or at least recognise the effect or importance of non-wing appendages during flight.

Chapter 4

Kinematics of *Anopheles gambiae* with Varying Temperature

4.1 Introduction

Behavioural differences in insects have been observed with changes in ambient temperature. For instance, in foraging bumblebees, the greatest wingbeat frequencies were reported at the lowest recording temperatures (~ 245 Hz at 14 °C and ~ 210 Hz at 24.5 °C (Unwin and Corbet, 1984)). Meanwhile, in rice leafroller, wingbeat frequency generally increased with temperature (Huang et al., 2013). This variability is owed to several factors such as, neuron activity (e.g., faster conduction speeds at warmer temperatures in honeybees, winter moths, and locusts (Esch, 1988, Xu and Robertson, 1994)) and adjustment of oxygen consumption to facilitate flight muscle contraction (Stevenson and Josephson, 1990). Mosquitoes are major vectors of disease that thrive in warm climates, and have also been observed to alter their flight behaviour with changes in ambient temperature. Villarreal et al. (2017) for example, reported the wingbeat frequency of female *Aedes aegypti* to increase by 8 - 13 Hz / °C from 18, 24, 28 and 31 °C experiments. While a ~ 25 Hz / °C increase in males between 22 °C and 28 °C had been previously seen in *Anopheles gambiae* (Georgiades et al., unpublished).

However, when wanting to test the effect of temperature against time-varying parameters needed to describe a single wingbeat (e.g., stroke angle), these

cannot be simply regressed, and summary parameters such as, wingbeat frequency and stroke amplitude are insufficient to describe the 3D motion of the wing. In addition to this, datasets with large amounts of data, spatial size and number of individuals as exemplified in the previous chapter can be difficult to handle. Methods to compress data but not oversimplify or ignore numerous parameters are thus continuously being challenged and refined. However, one approach to tackle the issues forementioned, is to use Fourier coefficients, that summarises time-varying data into summary parameters for each wingbeat (i.e. independent numbers for each wingbeat) while compacting data up to 1000 % (Skejø et al., 2021). In simple terms, Fourier coefficients are calculated by fitting a Fourier series to data, which is a sum of sine and cosines ideal for repetitive data such as the reciprocal motion of a wingbeat (Walker and Taylor, 2021) and running (Skejø et al., 2021, Jackson, 1979). Although, one must be careful with Fourier fitting as the considerable number of parameters to describe a wingbeat remain, and wing parameters are not independent (e.g., stroke angle and deviation angle are likely to be correlated as increase with stroke amplitude) which may lead to the overfitting of data. Principal component analysis (PCA) may therefore be used to create a set of independent parameters that are orthogonal to one another and highlight parameters which are most important to describe the variation in data. In more detail, this is a powerful analytic tool used in biomechanics that enables non-directional regressions (normal regressions only look at residuals in the y-axis) ideal for three dimensional coordinate data (Brandon et al., 2013, Witte et al., 2009, Jolliffe and Cadima, 2016). PCA has several outputs that are useful such as, principal component (PC) latent that explains variation of data captured, and PC scores (kinematics in a different axis system defined by PC) that can be regressed, and significance noted against

independent variables such as temperature. Riskin et al. (2008) was the first to apply PCA to 17 wing kinematic markers (or 20 joint angles) on short-nosed fruit bats. Where 95 % of variation was explained in the first 16 principal components (PCs) whilst quantifying the wings dimensional complexity and highlighting grouped correlations of wing joint motion. This then inspired Nagesh et al. (2019) to apply PCA to the Fourier fitted wing kinematics of 25,541 hoverfly wingbeats. More than 99 % of wingbeat variation was captured by a minimum of 20 PCs for time period components (cycle oscillations in a non-linear system) and only 2 PCs for time linear components that enable different cycle limits as are rarely coherent in kinematics (Nagesh et al., 2019).

In this study, I thereby focussed on the relationship between temperature (from 19.4 to 35.2 °C) and wing kinematics of free-flying *Anopheles gambiae.* Exploration within the same dataset previously reported in **Chapter 3,** revealed wingbeat frequency to significantly increase with temperature but plateaued at different temperatures for males (32.2 °C) and females (28.6 °C). Prior to this plateau region, as temperature increased, an ~ 1.5 ratio between male (29.9 Hz increase /°C) and female (20.9 Hz increase /°C) wingbeat frequency was observed. Meanwhile, wing speed for both sexes remained consistent as temperature increased. Data then underwent Fourier fitting, PCA, and sequence reconstruction to define wingbeat kinematics (including wingtip angle and wing twist) at specified temperatures. To further report, a minimum of 7, 16 and 7 PCs for wingtip, wing pitch and spanwise bending respectfully, were required to capture > 99 % of variation in 12,578 wingbeats. Detail here may provide insight on how mosquitoes behave independently, in line with global warming, and possibly in swarms (part of their courtship behaviour) as wingbeat frequencies

observed here overlapped with ranges of swarming wingbeat frequencies previously reported in literature (Somers et al., 2022, Garcia Castillo et al., 2021, Cator et al., 2011). As well as, provide compressed kinematic data for the most accurate aerodynamic modelling and force estimations to date.

4.2 Methods

The same dataset described in **Chapter 3** was used in the current study, but will be briefly described here for completeness. *Anopheles* were provided by the Albert Lab at UCL, and subject to free-flight experiments using a ten high-speed camera setup (12,000 fps aimed for approx. 15 - 20 frames per wingbeat), and stimuli to encourage manoeuvres (**Section 3.2.2**). During recordings ambient temperature varied between 19.4 and 35.2 °C, 20.2 – 64 % humidity, and air density 1.132 - 1.141 kg/m^3. Footage was then run through a fly tracker to acquire high-precision wing (namely, stroke angle, deviation angle, mid-wing pitch angle, wing twist gradient and spanwise bending) and body kinematics (**Section 2.2.3**). In total, 12,578 wingbeats were captured in 195 sequences (137 male and 58 female sequences) from 91 male and 38 female subjects. Body length varied between 4.35 – 5.63 mm (4.96 ± 0.25 mm, mean ± SD) for the male mosquitoes and 4.27 – 4.88 mm (4.57 ± 0.170 mm) for the female mosquitoes (**Figure 3.7**).

The original MATLAB code for Fourier and PCA analysis was written by Simon Walker (S.W), University of Leeds. All running of code, further analysis and figure generation was done by Rachel Tran (R.T), University of Leeds unless stated otherwise.

4.2.1 Fourier Analysis

To compress data, normalised body and wing kinematics were run through a Fourier fitting MATLAB script using periodic regression. The order of Fourier series applied to each body and wing kinematic variable was tailored to give the best fit with previous knowledge on insect parameters (e.g., wingbeat frequency, body size and filter frequencies used). A first-order harmonic was applied to body kinematics (yaw, pitch, roll and X, Y, Z lab coordinates), third-harmonic to wingtip kinematics (stroke angle and deviation angle) and spanwise bending, and filth-harmonic to wing pitch parameters, wing twist constant and wing twist gradient on both the left and right wings. The Fourier output was a $2n + 2$ vector for each wingbeat, determined by the nth order of harmonics used (weighing of sine and cosine), time linear variable and constant offset in preparation for PCA later on. The general equation for Fourier series fitting (**Equation 4.1**) applied to each kinematic parameter can be seen below where,

Equation 4.1 Equation for Fourier series fitting

$$f(\varphi) = K_0(\varphi) + K_1 + \sum_{i=1}^{n} [K_{2i}\cos(i\varphi) + K_{2i}\sin(i\varphi)],$$

$f(\varphi)$ can be any of the eleven kinematic parameters, and for the left and right wing if wing parameters. K_0 is a time linear variable of 101 equally spaced points between zero and one that allows for shifting in the y-axis as real wingbeats do not start and end at exactly the same place, K_1 is a constant offset that is the mean value of $f(\varphi)$ through the stroke, *n* is the order of harmonic selected (e.g., *n* = 3 for wingtip kinematics and spanwise bending, *n* = 5 for wing pitch kinematics) and K_2 … K_{2n} are Fourier coefficients of the *n*th order (Nagesh et al., 2019).

The Fourier output of each wingbeat (**Equation 4.2**) was therefore 24 (4 × 6, including time linear components) predictors (numerical coefficients) for the body, and (8 + 8 + 8 + 12 + 12) × 2 for the left and right wings (96 in total). Both were compiled in the format seen below where,

Equation 4.2 Format of Fourier output per wingbeat

$$K_A^{\varphi} = \left[K_0^{\varphi}, K_1^{\varphi}, \ldots K_{2n,}^{\varphi}\right]^T$$

K_A^{φ} is all linear and time periodic coefficients of any kinematic variable for one wingbeat and *T* is transpose. For each sequence, each kinematic variable was compacted into a matrices,

Equation 4.3 Format of Fourier output per sequence

$$X^{\varphi} = \begin{bmatrix} 1K_0^{\varphi} & 2K_0^{\varphi} & 3K_0^{\varphi} \\ 1K_{1,}^{\varphi} & 2K_{1,}^{\varphi} & 3K_{1,}^{\varphi} \\ \dots & \dots & \dots \\ 1K_{2n,}^{\varphi} & 2K_{2n,}^{\varphi} & 3K_{2n,}^{\varphi} \end{bmatrix},$$

where each column is a wingbeat and rows are its time linear and time period components (Nagesh et al., 2019) (**Equation 4.3**). An example plot of normalised kinematic parameters, and a Fourier fit of stroke angle and wing twist gradient can be seen in **Figure 4.1**.

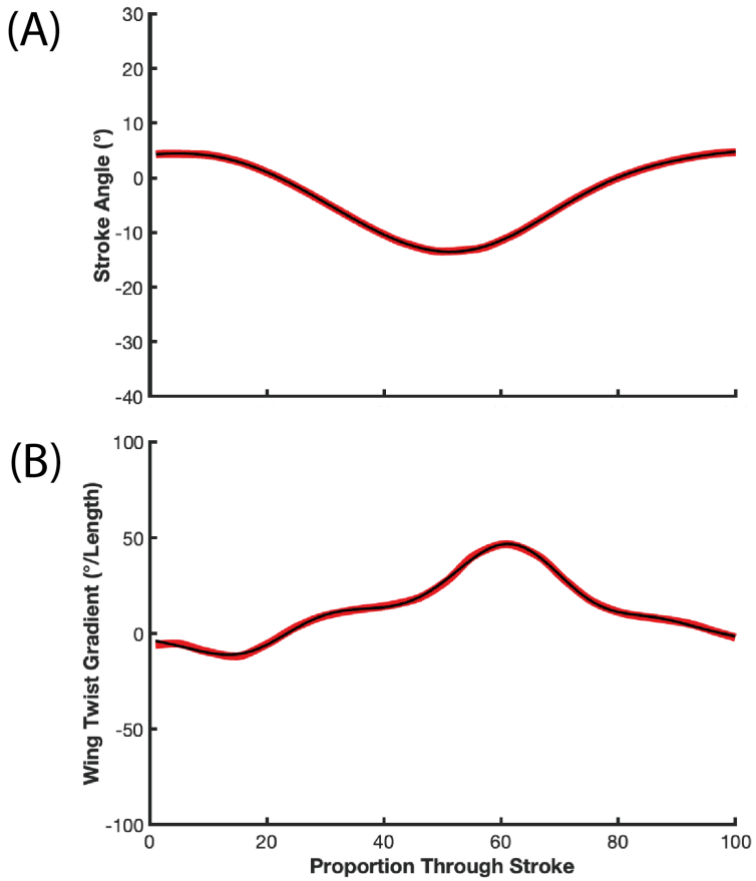

Figure 4.1 Example plots of normalised kinematic data (red) against a Fourier series fit (black)

A randomly selected (A) stroke angle fitted with a 3rd order harmonic and (B) wing twist gradient fitted with a 5th order harmonic Fourier series.

4.2.2 Principal Component Analysis and Sequence Reconstruction

The time linear components of Fourier data was first excluded in preparation for PCA. This was done so that wingbeats created could start and end at the same point in anticipation for further study on aerodynamic modelling (**Section 6.3.5**). Each sex and kinematic parameter in Fourier form whilst summing the left and

right wings was then processed independently to ensure uniform weighting's, as parameters had different units and range (e.g., wingtip angles in degrees and spanwise bending as a proportion of wing length). PCA of wing parameters revealed the coefficients of each PC (*C,* **Equation 4.4**) as a *m-by-m* matrix where each column contained the coefficients of PC ordered in ascending order of variance captured, and PC scores (*S,* **Equation 4.4**) ordered as a *u-by-m* matrix where *u* is the number of observations and *m* is individual PCs.

Equation 4.4 Principal component decomposition matrix

$$\hat{X} = SC^T$$

In **Equation 4.4**, the hat notation (^) of *X* further denotes matrix centring by subtracting the mean of columns to normalise the weighting of variables without the removal of underlying data (Riskin et al., 2008).

To validate results, PC scores were then used to reconstruct the wing kinematics of individual mosquitoes. The PC scores of wingbeats were first grouped if there was more than one recording from the same insect. This was acceptable as multiple recordings from the same individual were only taken immediately one after another, and only occurred at the same temperature (130 sequences from 107 individuals) or very close ambient temperatures (65 sequences from 22 individuals with a range of 0.08 – 0.56 °C between sequences from the same individual) to prevent pseudo replication and to ensure equal weighing's between subjects.

To ensure kinematic reconstructions reflected the limits of mosquito flight performance, plateau regions observed at the higher recording temperatures with wingbeat frequency for male and female mosquitoes (**Figure 4.2**) were identified as follows. The mean wingbeat frequency of each sequence was first calculated before being sorted according to its recording temperature. The minimum and maximum recording temperature (mean temperature was used if more than one sequence was captured for one mosquito) was then identified to generate a linearly spaced range with 0.01 equal spacing e.g., 21.86 (lowest recording temperature), 21.87 … 35.19 (highest recording temperature) for males. A loop was next run in MATLAB that performed linear regressions on the sorted mean wingbeat frequencies and their recording temperatures that were less than or equal to the temperature range defined above. This subsequently enabled predicted wingbeat frequencies and the sum of errors squared (between sorted and predicted wingbeat frequencies) to be calculated for all sequences. The index of the minimum sum of error squares was then located to fit plateaus across the remaining temperatures. This same technique was used to identify the start of any plateaus in other summary kinematic parameters (e.g., stroke amplitude, **Figure 4.3A**).

Equation 4.5 Equation for kinematic reconstruction

$$\hat{X} = (RP)^T + m$$

Only PC coefficients (*P*) and PC scores (*R*) that significantly correlated with temperature (within the specified range) via false discovery rate at a 5 % level (FDR, (Benjamini and Hochberg, 1995, Walker et al., 2012)), were selected to reconstruct wingbeat kinematics by reverse matrix multiplication and re-centring the data by adding back the mean (m) (**Equation 4.5**). The number of harmonics previously used to compress the data was then identified by the number of columns of means previously subtracted. Predictors for each corresponding harmonic was then created and multiplied by $\hat{X}$ to reconstruct kinematic parameters.

4.3 Results

4.3.1 Wing Kinematics and Temperature

To an extent, wingbeat frequency was shown to significantly increase with temperature in both males (R^2 = 0.737, P < 0.001) and females (R^2 = 0.542, P < 0.001) (**Figure 4.2A)**, sustaining a ratio between 1.34 to 1.57 (1.46 ± 0.06, mean ± SD) between the two. Wingbeat frequency increased by 29.9 Hz/°C between 22 – 32 °C in males (y = 29.86x – 28.34) and 20.9 Hz/°C between 22 – 28 °C in females (y = 20.91x – 9.76). However, no statistical changes in wingbeat frequency beyond 32.22 °C for the males and 28.64 °C for the females occurred. A similar relationship was found when wingbeat frequency was normalised by wing length (male R^2 = 0.627 and P < 0.001, female R^2 = 0.441 and P < 0.001) and temperature to account for differences in mosquito size (**Figure 4.2B**). Although, the origin of plateau regions for both sexes experienced a slight shift to 31.03 °C and 28.67 °C for the males and females respectfully.

In support of the findings above, stroke amplitude also decreased with temperature (male R^2 = 0.416 and P < 0.001, female R^2 = 0.390 and P < 0.001) but plateaued at 32.62 °C for the males and 27.55 °C for the females (**Figure 4.3A**). Lastly, wing speed remained constant for male mosquitos (R^2 = 0.0082, P = 0.291), meanwhile wing speed slightly increased with temperature in females (R^2 = 0.0909, P = 0.0214) (**Figure 4.3B**).

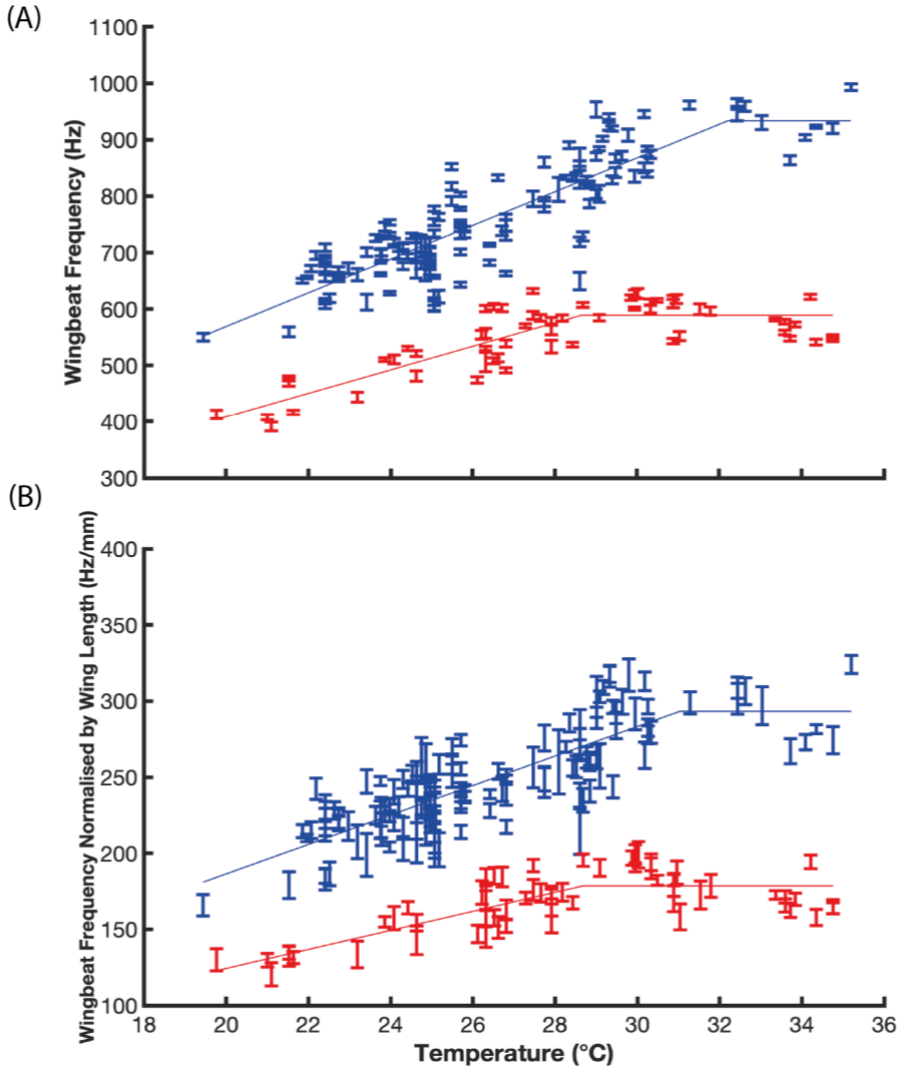

Figure 4.2 (A) Wingbeat frequency and (B) wingbeat frequency normalised by wing length with varying temperature in male (blue) and female (red) mosquitoes

(A) Wingbeat frequency significantly increased with temperature up to 32.22 °C in males (R^2 = 0.737 and P < 0.001) and 28.64 °C in females (R^2 = 0.542 and P < 0.001). (B) Wingbeat frequency normalised by wing length significantly increased with temperature in both males (R^2 = 0.627 and P < 0.001) and females (R^2 = 0.441 and P < 0.001) up to 31.03 °C and 28.67 °C respectfully. Vertical bars denote the mean and one standard deviation of each mosquito recorded.

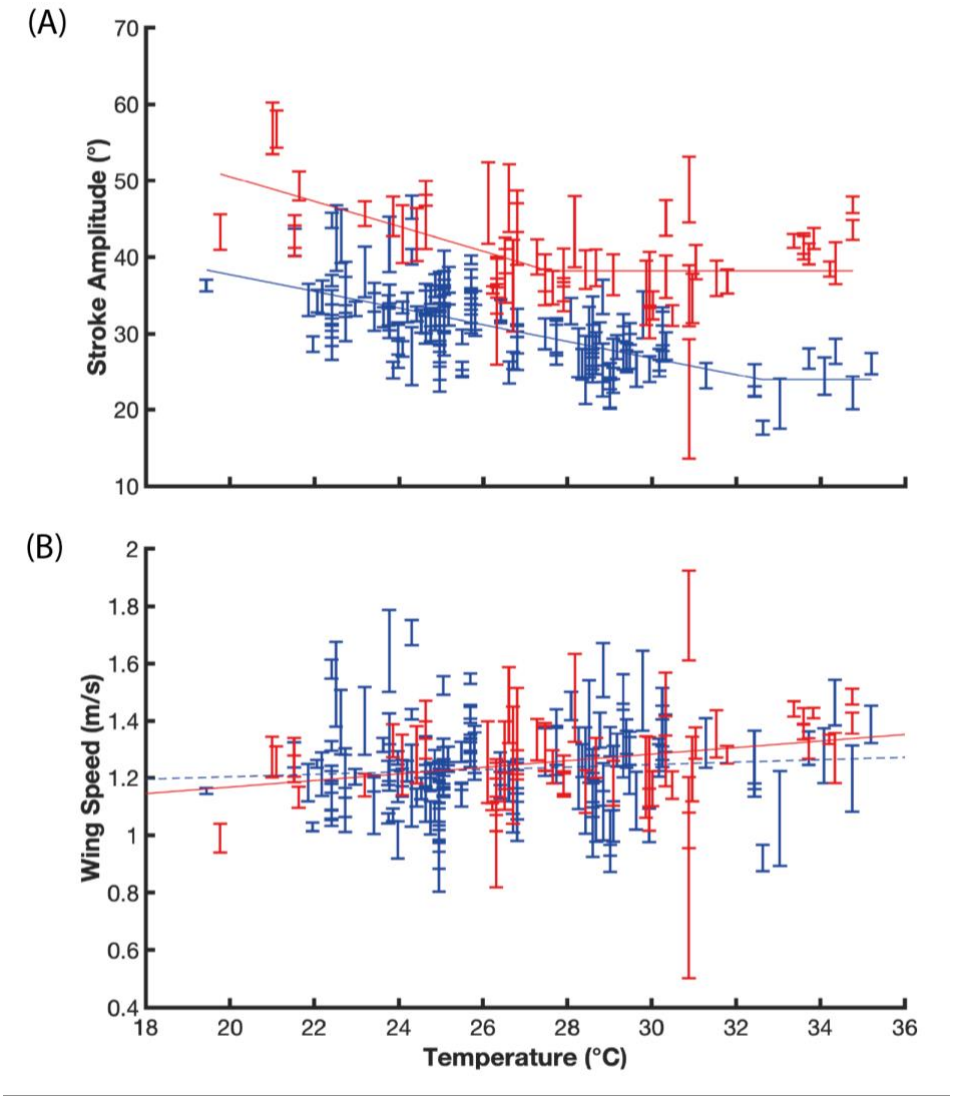

Figure 4.3 (A) Stroke amplitude and (B) wing speed with varying temperature in male (blue) and female (red) mosquitoes

(A) Stroke amplitude significantly decreased with temperature up to 32.62 °C in males (R^2 = 0.416 and P < 0.001) and 27.55 °C in females (R^2 = 0.214 and P < 0.001). (B) Wing speed with temperature was not statistically different in amongst males (R^2 = 0.0082 and P = 0.291). Meanwhile, wing speed in females weakly correlated with temperature R^2 = 0.0909 and P = 0.0214). Vertical bars denote the mean and one standard deviation of each mosquito recorded.

4.3.2 Body Kinematics and Temperature

Prior to the PCA of Fourier fitted wing kinematics and reconstruction of sequences, the significance between body kinematics (e.g., body acceleration, vertical velocity, body pitch in the lab axis system) for all sequences and temperature was determined to test for PCA suitability (e.g., to check if wingbeat frequency increased because subjects were flying faster). Only then, PCA ensued if overall body kinematics did not significantly correlate with varying temperatures to create descriptor wingbeats.

Vertical velocity (male R^2 = 0.0067 and P = 0.343, female R^2 = 0.0283 and P = 0.207, **Figure 4.4B**), total body acceleration (male R^2 = 0.0015 and P = 0.657, female R^2 = 0.0126 and P = 0.401, **Figure 4.4C**) and male body pitch (R^2 = 7.34 $\times$ 10^{-4} and P = 0.753, **Figure 4.4A**), did not significantly correlate with temperature. However, a weak correlation was found between female body pitch with temperature where R^2 = 0.102 and P = 0.0144 (**Figure 4.4A**).

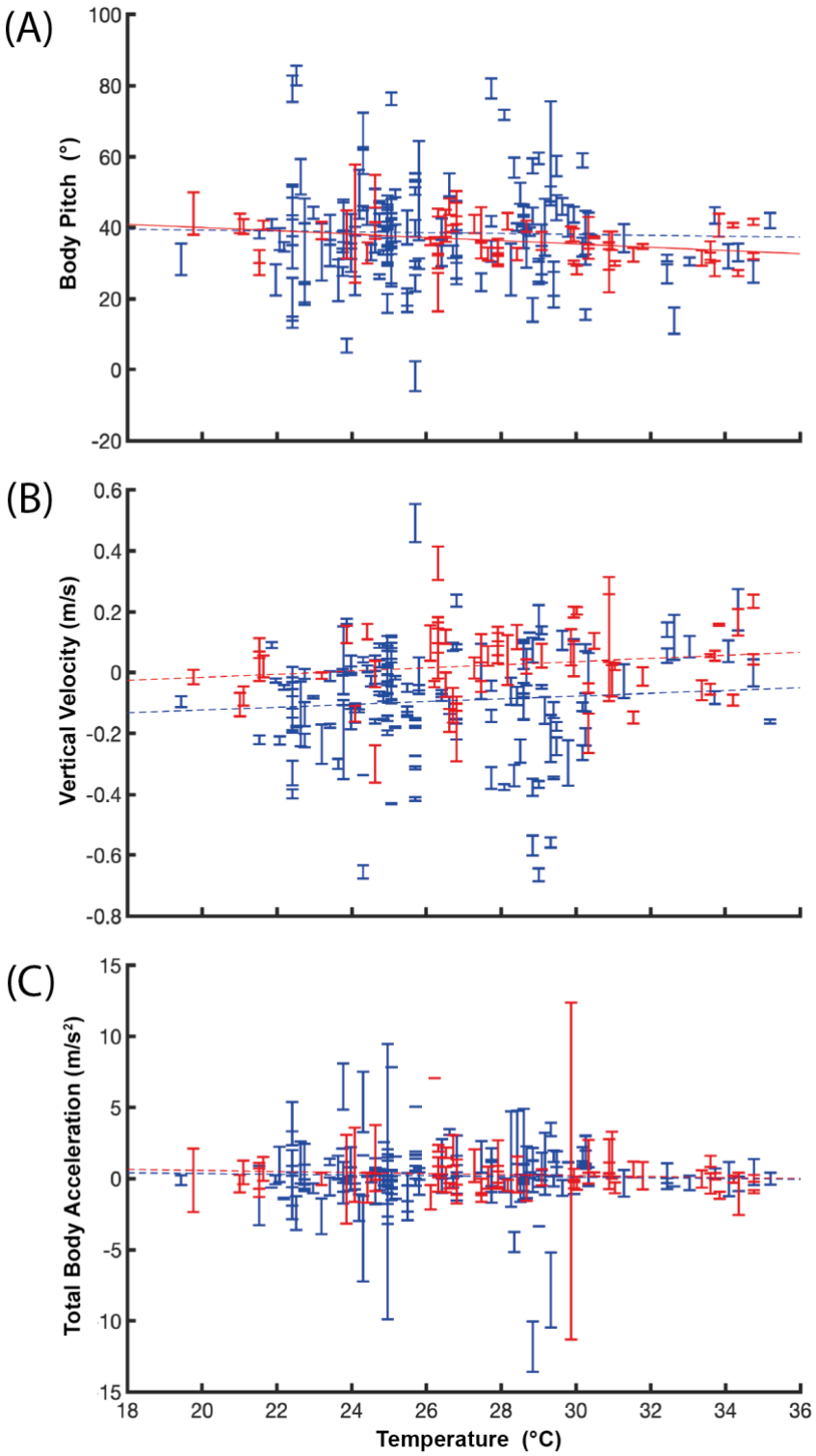

Figure 4.4 Body kinematics with varying temperature

(A) Body pitch, (B) vertical velocity and (C) total body acceleration. Males are coloured in blue and females in red. Vertical bars denote the mean and one standard deviation of each mosquito recorded. (A) Body pitch weakly correlated with temperature in the female mosquitoes (R^2 = 0.102 and P = 0.0144) but not in the males ($R^2 = 7.34 \times 10^{-4}$ and P = 0.753). (B) Vertical velocity did not correlate with temperature for both males (R^2 = 0.0067 and P = 0.343) and females (R^2 = 0.0283 and P = 0.207). (C) Total body acceleration did not correlate with temperature for both males (R^2 = 0.0015 and P = 0.657) and females (R^2 = 0.0126 and P = 0.401).

4.3.3 Principal Component Analysis

PCA was successfully used to compact a large dataset into a series of vectors (PC scores) and matrices (PC coefficients) for each wingbeat within a sequence and its kinematic parameters (left and right wing). PC scores for each sequence were contained within a N-by-14, N-by-22 and N-by-7 matrix where N is number of wingbeats for wingtip parameters, wing pitch parameters and spanwise bending respectfully.

To capture more than 99 % of variance of all data (male and female), a minimum of 7 out of 14 PCs was required for wingtip components, 16 out of 22 PCs for wing pitch components and 7 out of 7 PCs for spanwise bending (**Figure 4.5**). PCs beyond these minimums were likely to capture noise rather than important variation in data so were discarded from then on to further reduce the dimensions of data.

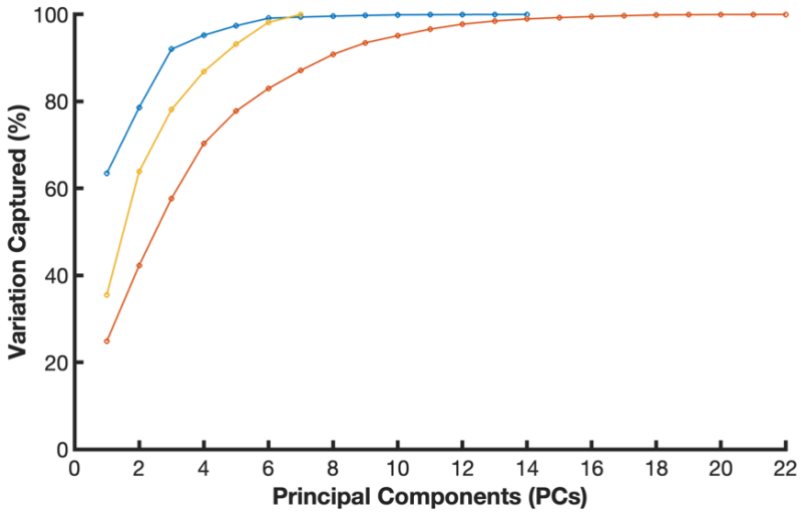

Figure 4.5 Cumulative percentage of variation captured in wing kinematics with number of principal components

Variation captured in wingtip parameters (blue), spanwise bending (yellow) and wing pitch parameters (orange).

Temperature ranges were truncated to 22 and 32 °C for males and 22 and 28 °C for female mosquitoes, to reflect the limits of their flight performance and to reconstruct the most realistic wing kinematics. **Figure 4.6** and **4.7** show the time history of reconstructed wing kinematics and of male and female mosquitos independently. The reconstructed stroke angle of male and female mosquitoes became shallower as temperature increased (**Figure 4.6A and B**). Where stroke angle mid-way through the stroke (0.5), shifted from – 20.7 ° to – 15.4 ° for males and – 23.2 ° to – 18.6 ° for females between temperature extremes. On the other hand, the reconstructed deviation angle of male and female mosquitoes mid-way through the stroke shifted from 12.7 ° to 11.6 ° and 4.5 ° to 1.7 ° for males and females respectively (**Figure 4.6C and D**). The shape of male and female wing twist constant and wing twist gradient through the stroke, remained approximately the same with increasing temperature (**Figure 4.7A and C**). However with

increasing temperature, male wing twist constant experienced a proportion through the stroke delay of ~ 0.04 (right shift) between 22 and 32 °C reconstructions (**Figure 4.7A**). Male wing twist gradient similarly displayed delays with temperature but this varied more obviously in some areas through the stroke. For example, from 0.4 to 0.6 proportion through the stroke, male wing twist gradient was delayed by ~ 0.03 in comparison to 0.6 to 0.8 proportion though the stroke delays of ~ 0.05 between wingbeats reconstructed at 22 and 32 °C (**Figure 4.7C**). On the other hand, female wing twist constant and gradient delayed the most from 0.6 to 0.8 through the stroke from 22 to 28 °C (**Figure 4.7B and D**). The fluctuations reported in spanwise bending of male reconstructed wingbeats, became increasingly less pronounced at greater temperatures, whereas females remained approximately the same (**Figure 4.7E and F**).

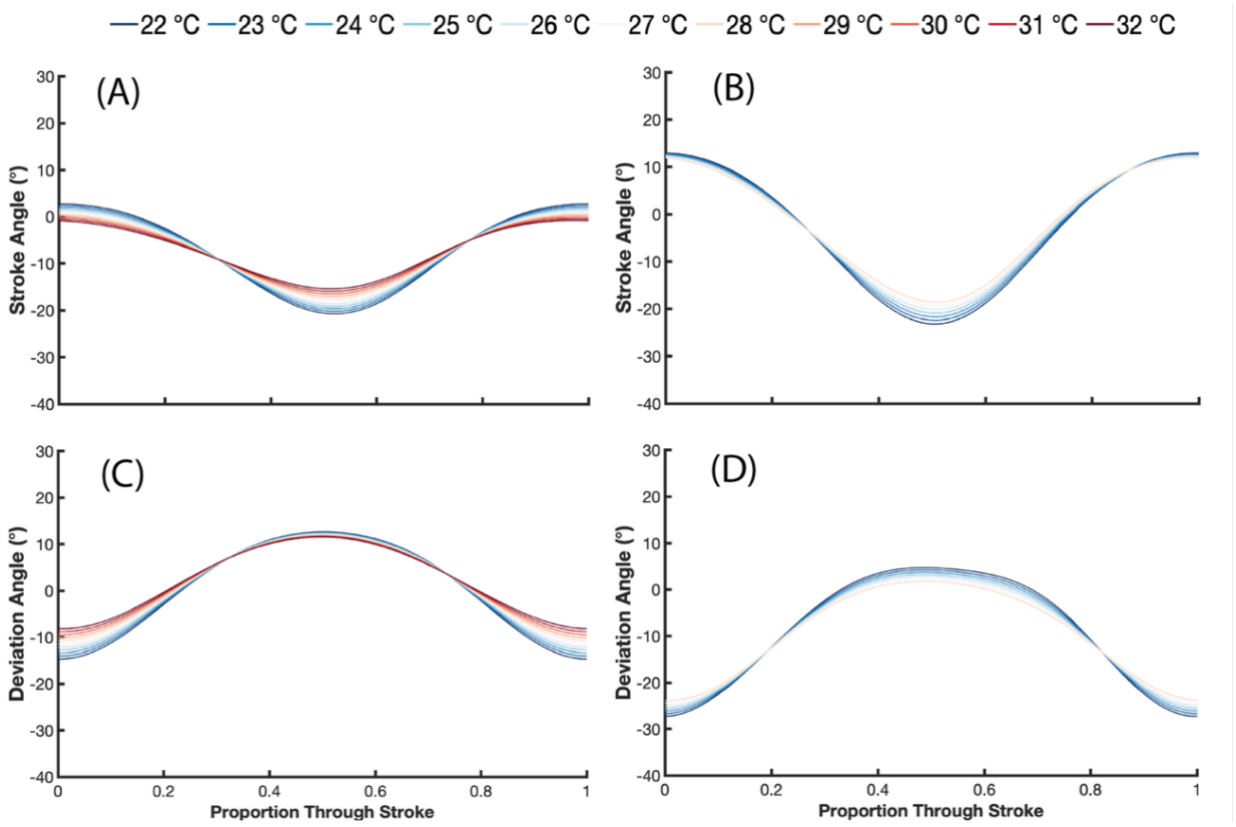

Figure 4.6 Time history reconstruction of wingtip kinematics

(A and B) Stroke angle and (C and B) deviation angle reconstruction for male (A and C) and female (B and D) mosquitoes. Each line colour represents reconstruction at a different temperature.

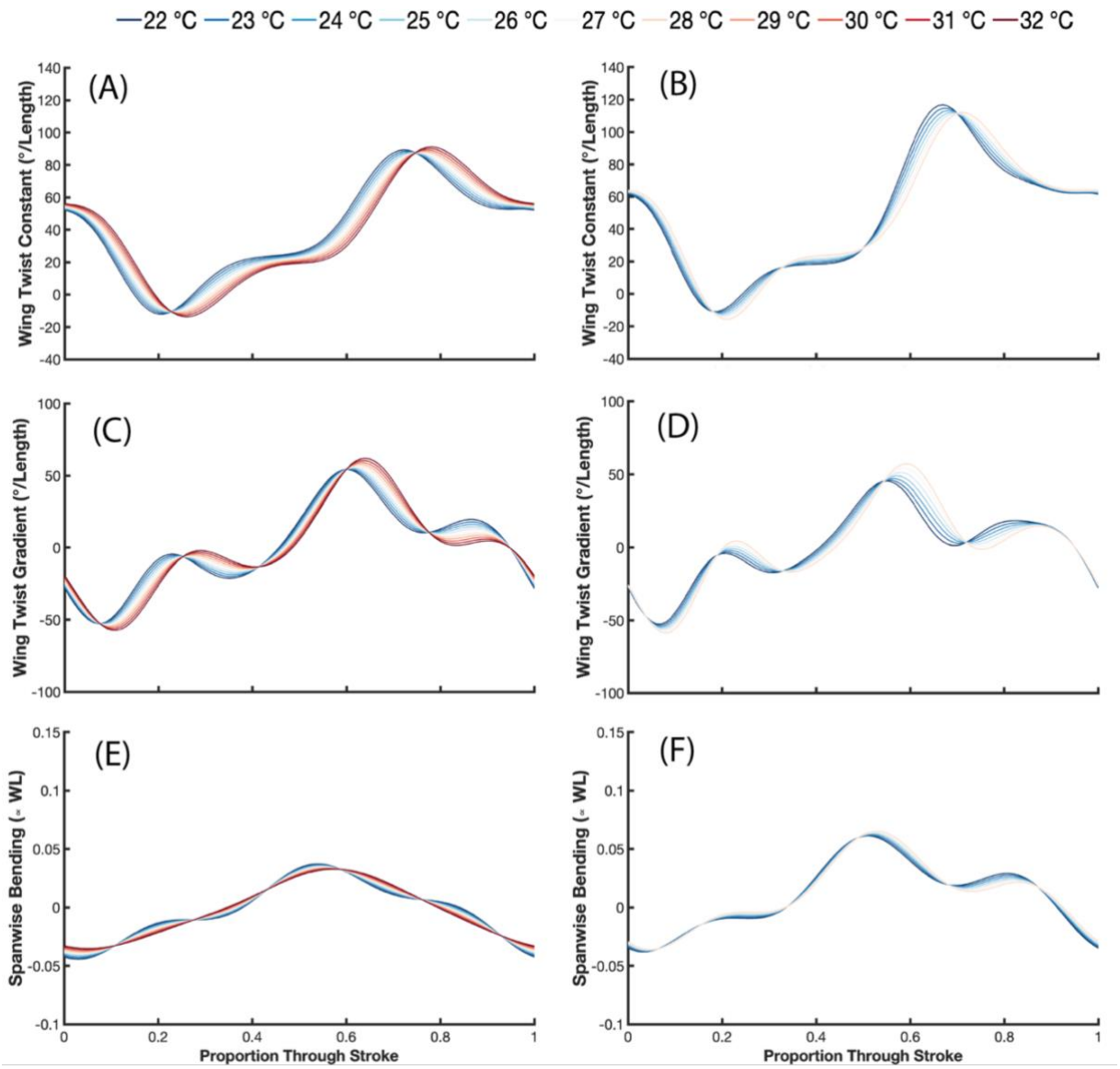

Figure 4.7 Time history reconstruction of wing pitch parameters and spanwise bending

(A and B) Wing twist constant, (C and B) wing twist gradient and (E and F) spanwise bending reconstruction for male (A, C and E (column one)) and female (B, D and F (column two)) mosquitoes. Each line colour represents reconstruction at a different temperature. Spanwise bending as a proportion of wing length (WL).

Changes in stroke amplitude, stroke plane angle (angle between wingtips at the extremes of the stroke), and mid-wing pitch angle at supination with temperature, were also estimated from reconstructed wingbeats and plotted against raw data as seen in **Figure 4.8**. From 22 to 32 °C reconstructions, male stroke amplitude decreased from 35.8 ° to 24.4 ° at ~ 1.14 °/ °C. Stroke plane angle increased from 50.4 ° to 54.3 ° at ~ 0.38 °/ °C, and mid-wing pitch at supination decreased from 39.3 ° to 24.5 ° at ~ 1.48 °/ °C. Meanwhile for female reconstructions from 22 to 28 °C, stroke amplitude decreased from 47.3 ° to 39.2 ° at ~ 1.36 °/ °C. Stroke plane decreased from 42.3 ° to 40.6 ° at ~ 0.28 °/ °C, and mid-wing pitch angle at supination decreased from 45.4 ° to 39.9 ° at ~ 0.92 °/ °C.

Lastly, the wingtip path of reconstructed wingbeats can be seen for both male and female mosquitoes in **Figure 4.9**. As temperature increased, the wingtip path of male generated wingbeats declined and for female wingbeats, the wing trace shifted posteriorly.

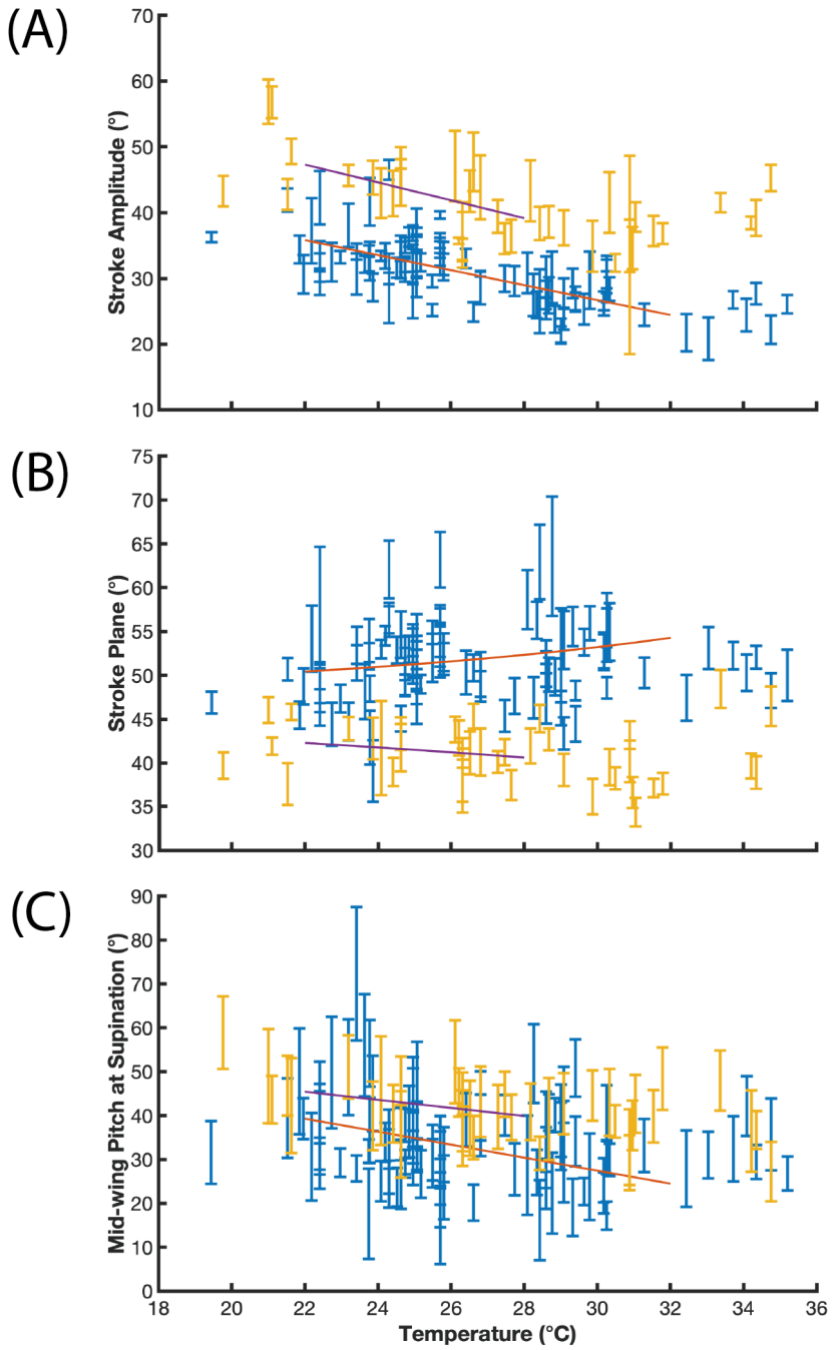

Figure 4.8 Stroke amplitude, stroke plane angle and mid-wing pitch at supination of male and female mosquitoes from reconstructions against raw data

(A) Stroke amplitude, (B) stroke plane and (C) mid-wing pitch at supination. Vertical bars denote the mean and one standard deviation of each male (blue bars) and female (yellow bars) mosquito recorded (raw data). Coloured lines are PCA estimates of kinematic parameters for male (orange) and female (purple) wingbeats from 22 – 32 °C and 22 – 28 °C respectfully. Equation of the line for male stroke amplitude $y = -1.14x + 60.88$ and female stroke amplitude $y = -1.36x + 77.14$. Male stroke plane ($y = 0.38x + 41.84$), female stroke plane ($y = 0.38x + 48.22$), male mid-wing pitch at supination ($y = -1.48x + 71.89$) and female mid-wing pitch at supination ($y = -0.92x + 65.69$).

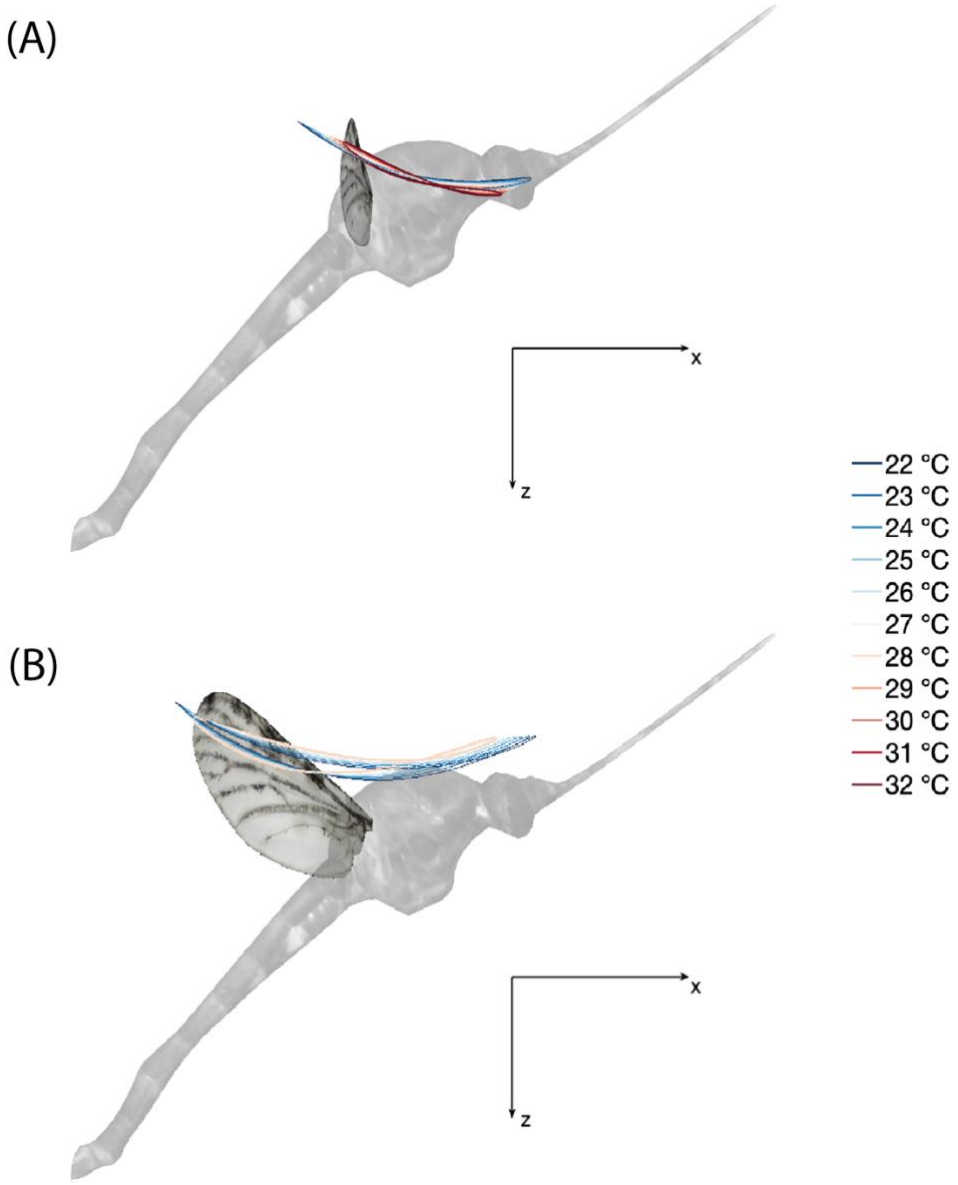

Figure 4.9 Wingtip path variation with temperature

Reconstructed wingtip path of (A) male mosquitoes from 22 to 32 °C and (B) female mosquitoes from 22 to 28 °C.

4.4 Discussion

There are currently over 3,500 identified mosquito species that occupy temperate to tropical parts of the world (Hawkes and Hopkins, 2022). Mean temperatures have been reported to range from 28 °C in Thailand and up to 39 °C in shallow pools in parts of Mauritius, are extremely advantageous for the mosquitoes life cycle (Srisuka et al., 2022, Jepson et al., 1947). I therefore sampled the kinematics of malaria mosquito *Anopheles gambiae* at different ambient temperatures, to first report that wingbeat frequency for both males and females increased with temperature before plateauing at different temperatures. Meanwhile, overall, body kinematics did not vary with temperature with the exception of female body pitch that correlated weakly. Lastly, to generate descriptor wingbeats to test the effect of temperature, only 7 PCs for wingtip, 16 PCs for wing pitch, and 7 PCs for spanwise bending was needed to capture > 99 % of parameter variation out of 43 PCs (grand total) calculated for 12,578 wingbeats.

4.4.1 Kinematics and Temperature

Data collection was performed during swarm times in order to access the upper limits of mosquito flight performance, as during swarm times, a 50 – 100 Hz boost in wingbeat frequency was expected in addition to the effects of ambient temperature during flight manoeuvres (Albert, UCL, pers comms) (Garcia Castillo

et al., 2021). Experimental conditions were supportive of swarming behaviour according to Somers et al. (2022) where *Anopheles* were able to swarm in 30 × 30 × 30 cm bug dorms, and lone males flapped faster in 5 × 5 × 5 cm flight arenas with only 12:12 hour day night cycles. However, flight observed in this study was ultimately not categorised as swarming behaviour, as male antennae vital for detecting females remained retracted during recordings (Nijhout and Sheffield, 1979). This was further confirmed by additional footage taken outside of swarm times and with the lab lights on to reveal no difference in behaviour (footage was then included in the dataset). Speakers playing an artificial female flight tone, and tethering a live female within the flight arena as additional stimuli was also attempted, but was unsuccessful at encouraging mating behaviour and manoeuvres (Nakata et al., 2022). It was therefore concluded, that the failure to swarm was largely owed to disturbances when transferring individuals into the flight arena from where they were housed (BugDorm), as erect antennae were seen prior to this transfer. The idea of keeping mosquitoes in the flight arena to acclimatise, was inappropriate as recordings needed a dust and water free environment that would have been introduced with the sugar water saturated cotton rolls required for feeding. The placement of one mosquito at a time within the flight arena was a further condition that needed to be satisfied as a crowded arena may have resulted in pseudo-replication and obstruction of camera if more than one mosquito was in the field of view.

In fluid dynamics, temperature, humidity, and pressure are closely related. At high temperatures, air has low viscosity (density) and high pressure as the area that air molecules occupy expands when the number and velocity of collisions between molecules rises. Whereas humidity decreases air pressure, as lighter

water molecules leave less room for heavier oxygen and nitrogen molecules. Humid or hot conditions therefore require more power (profile power and inertial power to flap wings) to accelerate air required to generate an equivalent lift force, in comparison to a lower humidity or temperature environment. Wing frequency for both sexes thereby increased with ambient temperature, in line with aerodynamic requirements as described above and muscle physiology as poikilotherms (Reinhold et al., 2018, Unwin and Corbet, 1984). However, the large increase in wingbeat frequencies observed cannot be explained entirely by the changes in air density. For example, a 10 °C change in temperature only promotes an ~ 3.5 % change in air density, that in turn only requires a ~ 1.5 % change in wingbeat frequency (an ~ 10 Hz change in wingbeat frequency if originally 800 Hz) to maintain vertical force (Masateru Meada, RVC, pers comms). Further investigation between environmental conditions and underlying body energetics is therefore needed (**Section 6.3.2**). Male mosquitoes also had greater wingbeat frequencies and plateaued at a greater temperature than their female counterparts, that may be explained by several lines of research. For example, (I) anatomical differences in body size and wing length could be one explanation as females were generally smaller but had longer wing lengths (body length 4.57 ± 0.17 mm and wing length 3.29 ± 0.11 mm) than the males (body length 4.96 ± 0.25 mm and wing length 3.08 ± 0.14 mm) (**Figure 3.7**). Cator et al. (2010) identified larger *A.gambiae* to operate at higher wingbeat frequencies than smaller individuals but wing length to correlate with wingbeat frequency between 23 – 29 °C. This was unlike my findings where wing length and wingbeat frequencies did not correlate (**Figure 3.8**) but this discrepancy could be attributed to Cator's tethering of subjects, and wider range of mosquito sizes available (male wing lengths 2.71 - 3.14 mm, female wing lengths 2.82 – 3.38 mm) (Cator et al.,

2010, Callahan et al., 2018). On the other hand, (II) the mechanical resonance of flight muscle for maximum efficiency determined by temperature may also differ between sexes. It may be speculated that underlying molecular mechanisms such as heat shock proteins (Quan et al., 2022) in males might be adapted/present to tolerate and or operate better at high temperatures. Thus, enabling wingbeat frequency to increase with temperature before plateauing and possibly failing later on (delayed heat death) than the females. Recordings at even greater temperatures (> 35.2 °C) to see when wingbeat frequency would begin to decrease was attempted but getting the lab hot enough proved challenging.

My result of males flapping approximately ×1.5 times faster than females before plateauing was unexpected as Somers et al. (2022) similarly reported a ×1.5 surge in male wingbeat frequency during swarming behaviour at only 28 °C. Further experiments to clarify whether flight tones are due to varying temperature and or swarming behaviour are therefore required.

4.4.2 PCA Analysis and Sequence Reconstruction

Due to the large size of the mosquito dataset, and overall poor relationship between body kinematics with varying temperature, the use of PCA to define wingbeat kinematics (including time-varying and other summary parameters e.g., stroke plane) at specified temperatures was enabled. The creation of descriptor wingbeats was essential to test the effect of time-varying wingbeat parameters

against temperature, as the approach of binning data by a temperature range, then taking the mean of wing kinematics would have been unsuitable due to phase differences. Taking the mean of wing kinematics would have thus produced data that appears smeared, atypical to what you would expect to observe during a wingbeat.

A large proportion of data captured in the first few PCs indicates that data within the parameter are similar, have close relationships, recognisable patterns and or little variation from wingbeat to wingbeat. The higher number of PCs to capture > 99 % variation in wing pitch parameters than wingtip parameters and spanwise bending was therefore anticipated due to the mosquitoes peculiar approach to generating lift with their highly deformable high aspect ratio wings, and dominating rotational phase nature (Bomphrey et al., 2017).

4.5 Conclusion

This thesis chapter presented the effect of temperature on *Anopheles* kinematics, in addition to, methods of data compression and formatting of a large dataset that often accumulates with kinematic studies. Both male and female mosquitoes were subject to ambient temperature change that altered their flight behaviour. Summary parameters, wingbeat frequency and stroke amplitude increased and decreased respectfully, but plateaued at different points at greater temperatures. The non-significant result of body kinematics with varying temperature, meant the large dataset could then undergo data compression via Fourier fitting and PCA to create descriptor wingbeats to test the effect of temperature as e.g., deviation angle cannot be simply regressed. Only a small subset of PCs were found to describe more than 99 % of variation in the data for wingtip, wing twist and bending parameters. This method further enabled the reconstruction of additional summary parameters such as, stroke plane and mid-wing pitch at supination from PC scores. Future studies wanting to test time-varying kinematics against different independent variables may benefit the most from the data compression and handling ideas presented here. Conversely, future advancements may use these results for the most advanced estimates of aerodynamic force production in *Anopheles* (see **Section 6.3.5**), and facilitate the development of the most advanced population control techniques to date in line with global warming.

Chapter 5

Body Kinematics and Operating Time Scales of *Coenosia attenuata*

5.1 Introduction

Coenosia attenuata (killer flies) are small ambush predators that are often used as control agents against agricultural pests (Kühne, 1998, Mateus, 2012). Their benefitable feeding habits include the consumption of fruit flies, whiteflies, psyllids, and gnats of comparable body size, but must first be efficiently located and chased (Martínez et al., 2017). Most predators thereby minimise their energetic costs in the form of muscle work, by first considering their environment, prey size, and physical abilities rivalled against their own. Killer flies consequently employ close proximity proportional navigation (PN, **Figure 5.1**) to minimise flight duration and distance, by monitoring their prey's location, and correcting its own course to maintain a constant line of sight (LoS) (Chance, 2019, Rossoni et al., 2021, Fabian et al., 2018). Robber flies (Wardill et al., 2017), dragonflies (Olberg et al., 2000), bats (Ghose et al., 2009), and Harris' hawks (Brighton and Taylor, 2019) similarly use PN against fast moving targets. Whilst one classic example of human mechanisation of this technique is the development of guided missiles (Palumbo et al., 2010).

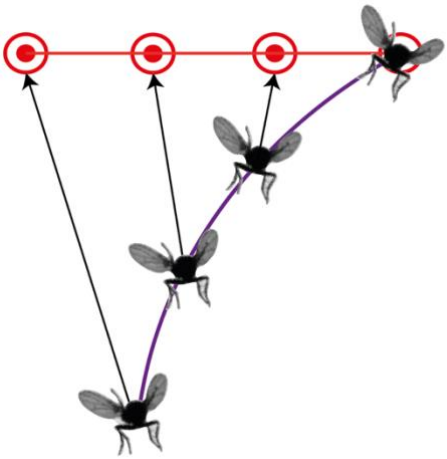

Figure 5.1 Illustration of proportional navigation

During pursuit, the killer fly (pursuer, along the purple line path) locates its target (red circle with red ring), then maintains a constant line of sight (LoS, black arrow) till interception. Figure adapted from (Fabian et al., 2018).

Equation 5.1 Modelling proportional navigation

$$\dot{\gamma} = N \times \dot{\lambda}$$

To model PN, **Equation 5.1** is used where, $\dot{\gamma}$ is the rotation rate of the predator's heading angle, *N* is the navigation constant (also referred to as navigational gain or fixed gain in literature) and $\dot{\lambda}$ is the line of sight rotation rate between the pursuer and target (Thyselius et al., 2023, Rossoni et al., 2021). The turn rate of the pursuer is therefore proportional to the rotation rate of the LoS, and *N* values are a dimensionless number that determines the pursuer's ability to manoeuvre during flight (i.e., how rapidly the pursuer can adjust its bearing). Meaning *N* = 1 is a constant bearing angle, generally high *N* values denote large changes to the pursuer's LoS and faster convergence towards prey, and vice versa for low *N*

values. Variations in navigation constant of the pursuer thus trade off flight stability and speed of convergence to the target.

Attacks from above (against clear sky) and below (with cluttered backgrounds) are uncommon in predatory insects due to their restrictions in vision, and effects of vicious and inertial drag. However, both have been observed in killer flies with dive accelerations impressively reaching up to 36 ms^2, when compared to the Peregrine falcon diving at 12 ms^2 (Rossoni et al., 2021, Ponitz et al., 2014). The compound eye (**Section 1.6**) is possibly the most metabolically expensive (e.g., due to its heavy weight) part of their sensory system, and most vital variable when deciding to attack (Niven and Laughlin, 2008, Wardill et al., 2015, Gonzalez-Bellido et al., 2011, Laughlin et al., 1998). Hunting dragonflies with up to 97 % success rates for example, are certainly supported by their large and developed eyes (e.g., *Anax junius,* body length up to 76 mm, interommatidial angle ~ 0.24 degrees (Land, 1997, Sherk, 1978, Bodmer, 2023)) to produce relatively high resolution images to estimate size and distance of prey (Olberg et al., 2000, Olberg et al., 2005). Killer flies on the other hand, have limited spatial resolution constrained by their small compound eyes (*Coenosia attenuata*, body length 4 mm (Fabian et al., 2018) and interommatidial angle of 1.88 degrees (Gonzalez-Bellido et al., 2011). This means that they launch attacks without knowing their target's absolute distance and size.

Previous studies encouraged hunting behaviour in killer flies by presenting a moving target at velocities in line with prey recorded infield studies. Wardill et al. (2015) found a 2.14 mm black bead moving between 0.55 - 0.85 m/s to be best conditions for high attack probability, and a minimum pursuit distance of

approximately 100 mm for killer flies. Rossoni et al. (2021) used a 2.1 mm black bead between 0.65 – 0.8 m/s and found maximum pursuit distance to be 170 mm and wingbeat frequency to not correlate with dive angle. Meanwhile, Fabian et al (2018) used a 1.3 – 2.9 mm silvered bead between 0.10 – 0.79 m/s and live *Drosophila* (0.54 – 1.23 m/s) for linear and erratic targets respectfully. They then reported a navigation constant of $N \approx 1.5$ for optimum control with close target proximity in killer flies. As well as $N \approx 3$ for *Holcocephala fusca* (robber fly) that are long distance hunters in comparison (pursuit distance 81 – 788 mm, *Coenosia* pursuit distance 23 – 213 mm) (Fabian et al., 2018). However, the papers aforementioned only described the flight trajectories and some body kinematics as a point mass (with no knowledge on body orientation) of *Coenosia* hunting behaviour. Important detail on wing kinematics that in turn determine body rotations, and manipulate aerodynamic force production of manoeuvres are thus also absent in literature.

Killer flies and their close range pursuit, and small body size thereby caught my attention as ideal candidates for the experimental setup described in **Section 2.2**. In this study I aimed to report the body (e.g., body accelerations and angular rate) and wing kinematics (e.g., wing twist) of *Coenosia attenuata* when manoeuvring in response to artificial prey. Kinematics will provide insight on for instance, their operating time scales for comparison to other predatory insects and escaping insects of comparable size such a robber flies (6 mm, *Coenosia* 4 mm (Fabian et al., 2018)) and *Drosophila* (~ 2.7 mm (Ristroph et al., 2013)). Moreover, insight on how *Coenosia* may orientate themselves relative to prey for more accurate fitting of navigation models, and how they generate their extreme manoeuvres. The camera rig was personalised with two different configurations of hunting

stimuli (a moving black bead) to encourage manoeuvres: (I) a bipolar stepper motor for a circular motion, and a (II) servo motor for a linear back and forth. PN was not observed in this study as killer flies did not strongly interact with the bead however, surveillance behaviour was likely as the killer fly frequently approached and exited the field of view of the high speed cameras.

5.2 Methods

5.2.1 *Coenosia* Insect Care

Coenosia attenuata pupae were kindly provided by the Gonzalez-Bellido group at the University of Minnesota. Pupae were then reared at the University of Leeds in damp coconut husk at 23 ° C and 80 % humidity in 30 × 30 × 30 cm mesh cages (BugDorm, MegaView Science Co, Ltd, Taiwan). Once emerged, adults were provided consistently with water and wild type fruit flies (Blade Biological Ltd, UK) at an approximate 10:1 ratio to minimise cannibalism. Adults (mean body length 3.4 ± 0.034 mm (mean ± SD) and wing length 2.9 ± 0.028 mm) were then individually isolated 3-days post-eclosion, for up to 72-hours in 15 ml falcon tubes, with wet paper towel before attempting data collection.

5.2.2 Tailored Kinematic Acquisition

High-speed Photron cameras were set to record a 6,400 fps at 1024 × 1024-pixel resolution for all experiments using the setup described in **Section 2.2**. However, killer flies were tested in mixed (sex) groups of five to keep individuals alert, and to increase the odds of successful recordings within a 200 mm diameter free-flight arena. Subjects were then exposed to two different types of stimuli in order to encourage high-speed manoeuvres as detailed in the following subsections. For both stimuli options, once insects had been exposed to the stimulus, they

were also replaced with a new group of starved insects every 30 minutes, as insects became tired or desensitised to the stimulus.

Once footage had been obtained, the fly tracker was modified so that forward and backward filtering was performed on the tracked body and wingtip kinematics (**Section 2.2.3**). This was done using a 3rd order low pass Butterworth filter, with a cut-off frequency of 150 Hz and 1000 Hz for the body and wingtips respectfully. Whereas a 5th order low pass Butterworth filter with a cut-off frequency of 2100 Hz was used on the wings. For body and wing kinematic parameter definitions please refer to **Figure 2.8**.

5.2.2.1 Circular Motion Stimulus

A stepper motor (26M048B2B, Portescap, USA) with a 3D printed holder (Shapr3D Version 5.4 and printed with the Ultimaker S7 Pro Series) was used to repetitively half rotate (20 revolutions per minute (RPM), 23 steps) a 20 mm diameter PLA disc. Extruding from this disc was a 45 mm long and 0.5 mm diameter white painted spring steel attachment (arch length 60 mm, max surface speed 6.27 m/s) with a 2.1 mm black bead thread through and glued at its tip. A Arduino Uno Rev3 (Arduino IDE Version 2.0.1., USA) was used to control the stepper motor, to continuously rotate the bead clockwise and anticlockwise three times before a two second delay to maintain killer fly attention (depicted in **Figure 5.2A**). This stimulus was positioned just outside the field of view of the high-speed cameras.

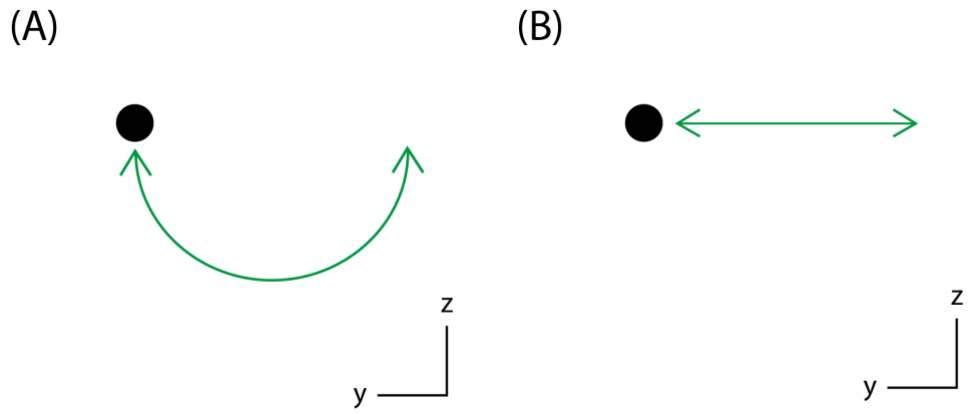

Figure 5.2 Stimulus used to encourage flight manoeuvres

(A) Bipolar stepper motor used to drive the beads circular motion. (B) Servomotor used to drive the back and forth movement of artificial prey. Green arrows are the beads (black circle) path. Not to scale.

5.2.2.2 Linear Motion Stimulus

Once insects had settled (perched) within the free-flight arena, a 2.1 mm black bead was quickly moved approximately linearly back and forth to simulate prey (**Figure 5.2B**). The mechanism for the moving bead was as follows, a brushless servomotor (SB-2272MG, 250 - 333 Hz frequency and 1520 microseconds pulse width, Sarvox Servo, Belgium) with heatsinks on either side (Model 6744762 17K/W, Fischer Elektronik Germany), and a 85 mm 3-D printed arm (Shapr3D Version 5.4 and Ultimaker S7 Pro Series, USA) was responsible for driving the bead's motion. Attached to the end of the printed arm was a 0.5 mm thick, matte white (White 2.0, Culture Hustle, USA) spring steel component that was then fed into a shorter carbon fibre tube to linearly guide and minimise the bead's

oscillation (attached to the end of the spring steel). A Arduino Uno Rev3 (Arduino IDE Version 2.0.1., USA) was used to control the servo motor between 0 and 30 degrees, with 30 ms delays to get the bead to travel ~ 20 mm in each direction and between 0.05 – 1.3 m/s (0.625 m/s mean velocity). The stimulus also paused every second to prevent overheating of the servo motor and to maintain killer fly attention.

Due to the beads linear motion and compact build, the stimulus was able to be placed within the high-speed camera's field of view without dramatically obstructing the insects during recordings (**Figure 5.3A**). This then enabled the position of the bead to be tracked and area masked so that it did not interfere with the fly tracker (**Figure 5.3B**).

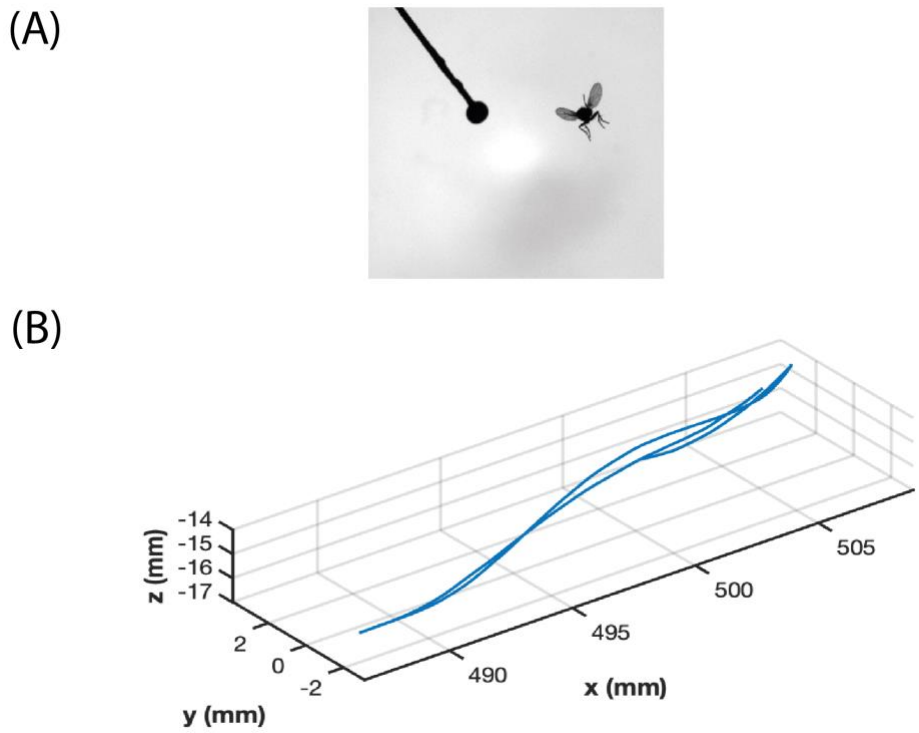

Figure 5.3 Stimulus appearance in camera view and tracked bead position

(A) Linear stimulus appearance (black rod and bead at its end) and approaching killer fly in one camera view and (B) an example plot of the bead's location tracked.

5.3 Results

5.3.1 Kinematic Results Overview

71 sequences were acquired using the bipolar stepper motor stimulus (from now on referred to as Dataset one) and 39 sequences were acquired using the servomotor (Dataset two).

5.3.1.1 Verification of Proportional Navigation

However, before further analysis, sequences from Dataset two were first checked for signs of PN by calculating the distance between the bead stimulus and killer fly over time (**Figure 5.4**). Only sequences where the stimulus was moving, distance consistently decreased, and the minimum distance between the pursuer and bead reached less than 10 mm were then selected for PN modelling. All sequences that met these requirements (7 sequences) showed no signs of PN as navigation constants calculated were near zero (N = 0.14 ± 0.25 navigation constant), and the navigation constant of *Coenosia* has been reported to be N = 1.5 in the past (Fabian et al., 2018). It was therefore concluded that the killer flies were not performing pursuit behaviour towards both stimuli types. From here on, detail on the bead stimuli were consequently not reported further, and sequences from Dataset one and two were grouped (110 total number of sequences) to focus on reporting body and wing kinematics during manoeuvres.

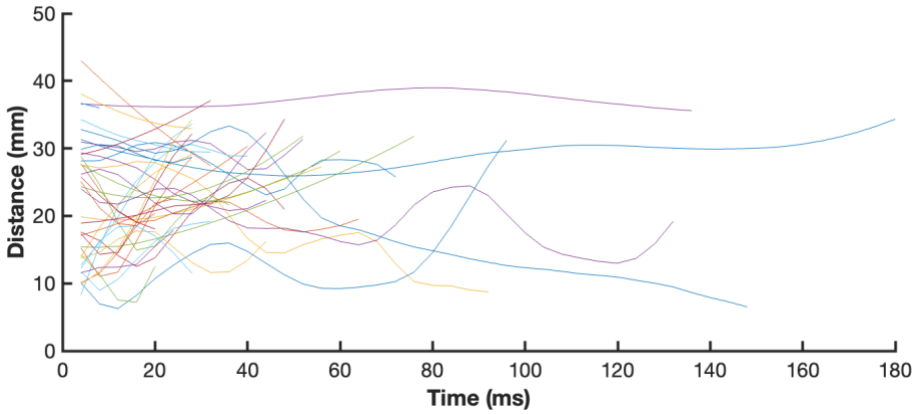

Figure 5.4 Distance between the killer fly and bead over time

Each line plotted represents the distance between the killer fly and bead in one sequence (*N* = 39 sequences).

5.3.2 Sample Sequences and their Kinematics

Footage acquired captured the free-flight trajectories, and body and wing kinematics of *Coenosia*, with 262 ± 27 Hz wingbeat frequencies and 120 ± 17 º stroke amplitudes. Sequences were brief, with the mean sequence length being 352 frames (54 ms or ~ 14 wingbeats) before the subject exited the view of high-speed cameras. Nonetheless, killer flies performed a range of manoeuvres as previewed in **Figures 5.5** and **5.6**.

In **Figure 5.5 column one,** a banked turn is shown. Changes in wingtip (stroke and deviation angle) and wing pitch angle between the left and right wing generated active torques that in turn caused the body to yaw (117 º) and roll (120 º) right for approximately 0.015 seconds (15 ms or ~ 4 wingbeats) (**Figure 5.5B**).

During this period body yaw and roll velocities, and angular velocity also peaked at ~15000 º/s and ~ 4000 º/s before decreasing respectfully (**Figure 5.5C and D**). The body then underwent pitch (- 50 º in 0.020 seconds (20 ms or ~ 5 wingbeats)) in its new direction before increasing wingbeat frequency (251 to 267 Hz, not shown in figure).

In **Figure 5.5 column two,** the subject did a U-turn where during the first saccade (0 – 0.09 seconds), body angles remained approximately constant and the flight trajectory straight. The U-turn (- 130 º, - 50 º, and - 30 º change in yaw, pitch and roll respectfully in 0.09 - 0.125 seconds (77.5 ms or ~ 19 wingbeats), **Figure 5.5B**), then occurred in two major steps most easily seen in changes in angular velocity with local minima of – 5700 º/s and – 12400 º/s (**Figure 5.5D**). In addition, there was a slight increase in wingtip angles in both wings, and greater differences in left mid-wing pitch on the up and downstroke (**Figure 5.5E to F**). Once the turn had been completed a second saccade (0.125 – 0.18 seconds) then occurred where the body approached near pre-turn pitch and roll body angles.

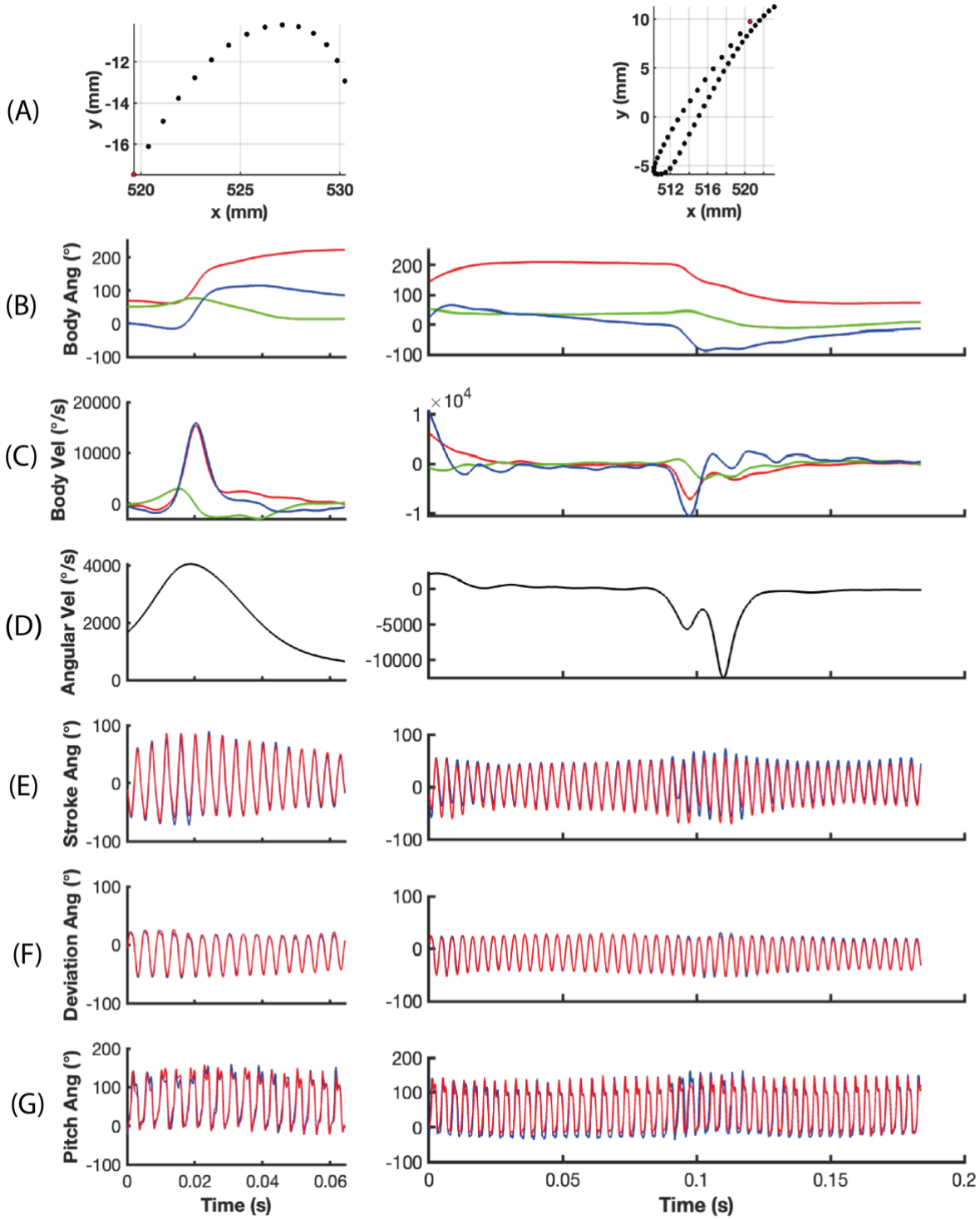

Figure 5.5 Sample sequences: banked turn and U-turn

Flight parameters over time for an example banked turn (column one) and U-turn (column two). The corresponding rows show (A) the two dimensional flight trajectory of the insect where each black dot is the body's position at each wingbeat, and the red dot is the fly's final position in the sequence. (B and C) Body angle and body angle velocities described as yaw (red), pitch (green) and roll (blue) in the laboratory fixed axis system. (D) Angular velocity, wingtip angles where stroke angle (E), deviation angle (F) and (G) is mid-wing pitch angle. For (E to F) rows, left (blue) and right (red) wings.

In the repertoire of flight manoeuvres observed, killer flies also flew upside down in portions of their flight path without crashing. In **Figure 5.6 column one,** the killer fly begun upside down in the sequence then rolled (150 º to 25 º in 0.04 seconds (40 ms or ~ 10 wingbeats), anti-clockwise) so that the body was upright (**Figure 5.6B**). Yaw, pitch and their corresponding changes in velocity remained approximately stable (**Figure 5.6B and C**). Subtle differences in wingtip angles were observed however more obvious differences in mid-wing pitch angle was seen in **Figure 5.6G**, where greater elastic recoil was observed during stroke reversal at the end of the upstroke (pronation) than stroke reversal at the end of the downstroke (supination) (Ishihara and Horie, 2017).

In the sequence depicted in **Figure 5.6 column two**, the killer fly can be observed flying backwards for 0.03 seconds (30 ms or ~ 8 wingbeats). All body angles remained stable, but yaw and roll body angle velocities increased (up to 2388 º/s and 2698 º/s respectfully) then decreased, whilst body pitch velocity remained near zero (**Figure 5.6B and C**). Wingtip angles were of similar magnitude and the mid-wing pitch angles of left and right wings were also similar throughout the sequence (**Figure 5.6E to G**). Although, wingtip angles used were interestingly

shallow with stroke amplitudes operating between 100 º and 107 º at a mean wingbeat frequency of 291 Hz.

Lastly in **Figure 5.6 column three**, the killer fly came to a quick stop. The body first pitched up by 76 º (at a peak pitch velocity 5883 º/s) before yaw and roll decreased (**Figure 5.6B and C**). Deviation angle increased approximately symmetrically for both wings, but stroke angle increase occurred at a greater rate for the left wing (**Figure 5.6E and F**). Whereas a right shift (delay) in mid-wing pitch angle can be seen at first for the left wing **(Figure 5.6G**). These kinematics for the left and right wings then became symmetrical at different time points at 0.027 seconds and 0.014 seconds into the sequence for stroke angle and mid-wing pitch angle respectfully (**Figure 5.6E and G**).

This results section only describes a small proportion of the flight behaviours observed. Although it is sufficient to show that small changes in wing kinematics and their operating time scales, are responsible for the wide range of body rotations and manoeuvres. **Figure 5.7** summarises *Coenosia* flight performance in all sequences. Wingbeat frequency ranged between 176.2 – 334.6 Hz, with a median of 263.4 Hz, and interquartile range (IQR) of 33.5 Hz (**Figure 5.7A**). Total velocity ranged between 0.053 – 1.570 m/s, with a median of 0.458 m/s, and IQR of 0.310 m/s (**Figure 5.7B**). Meanwhile, total acceleration ranged between 0.238 – 51.320 m/s^2, with a median of 7.052 m/s^2, and IQR of 6.245 m/s^2 (**Figure 5.7C**). Whilst the angular velocity of all data had a median of – 9.18 º/s and IQR 819.98 º/s (range -1.30×10^4 to 1.60×10^4 º/s) and angular acceleration median of -

24.81 º/s^2 and IQR 3.79 × 10^4 º/s^2 (range -1.88 × 10^6 to 1.89 × 10^6 º/s^2) (**Figure 5.7D and E**).

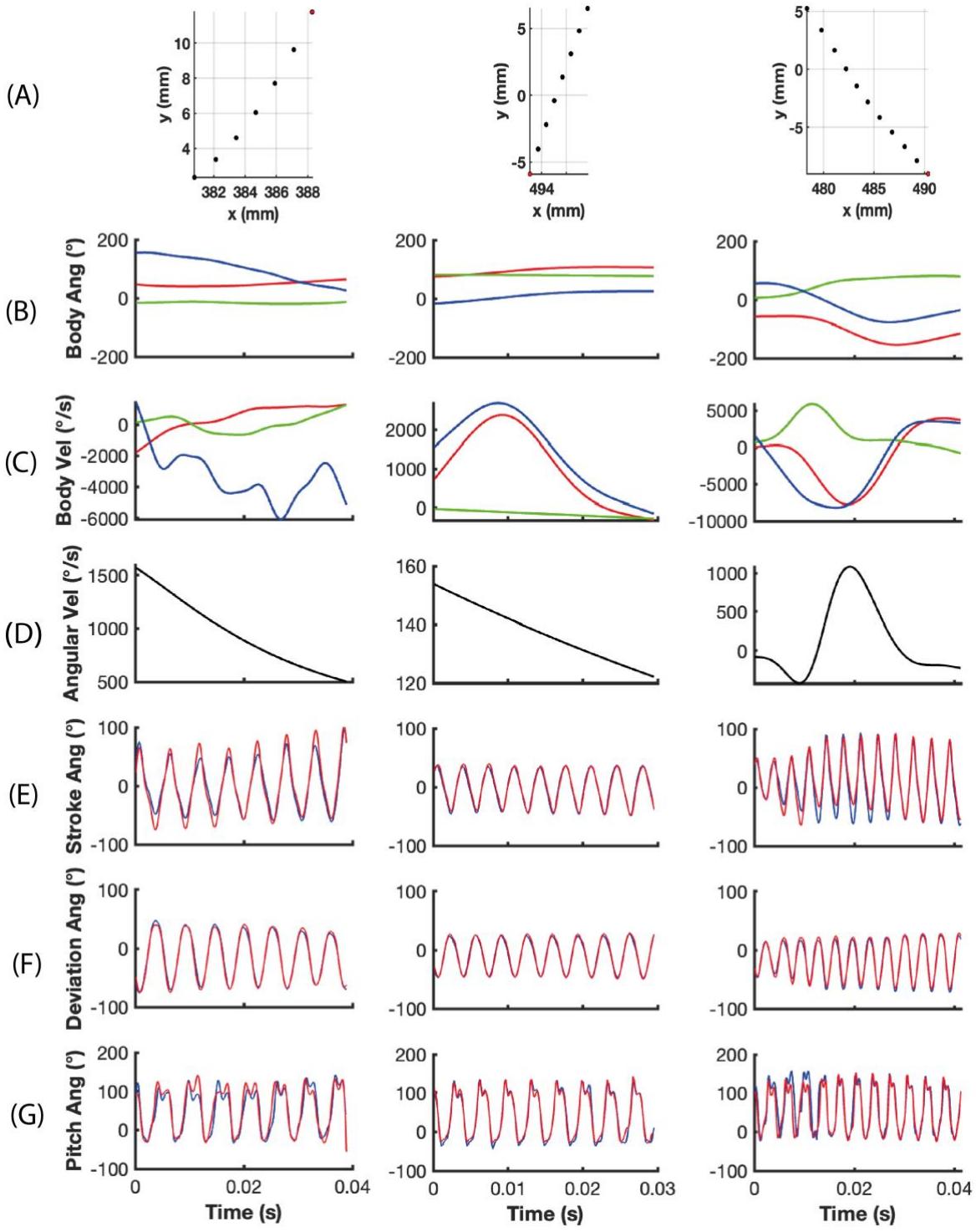

Figure 5.6 Sample sequences: upside down flight, backwards flight and flight coming to quick stop

Flight parameters over time for an example sequence of upside down flight (column one), backwards flight (column two) and a quick stop (column three). The corresponding rows show (A) the two dimensional flight trajectory of the insect where each black dot is the body's position with each wingbeat, and red dot is the fly's final position in the sequence. (B and C) Body angle and body angle velocities described as yaw (red), pitch (green) and roll (blue) in the laboratory fixed axis system. (D) Angular velocity, wingtip angles where stroke angle (E), deviation angle (F), and (G) is mid-wing pitch angle. For (E to F) rows, left (blue) and right (red) wings.

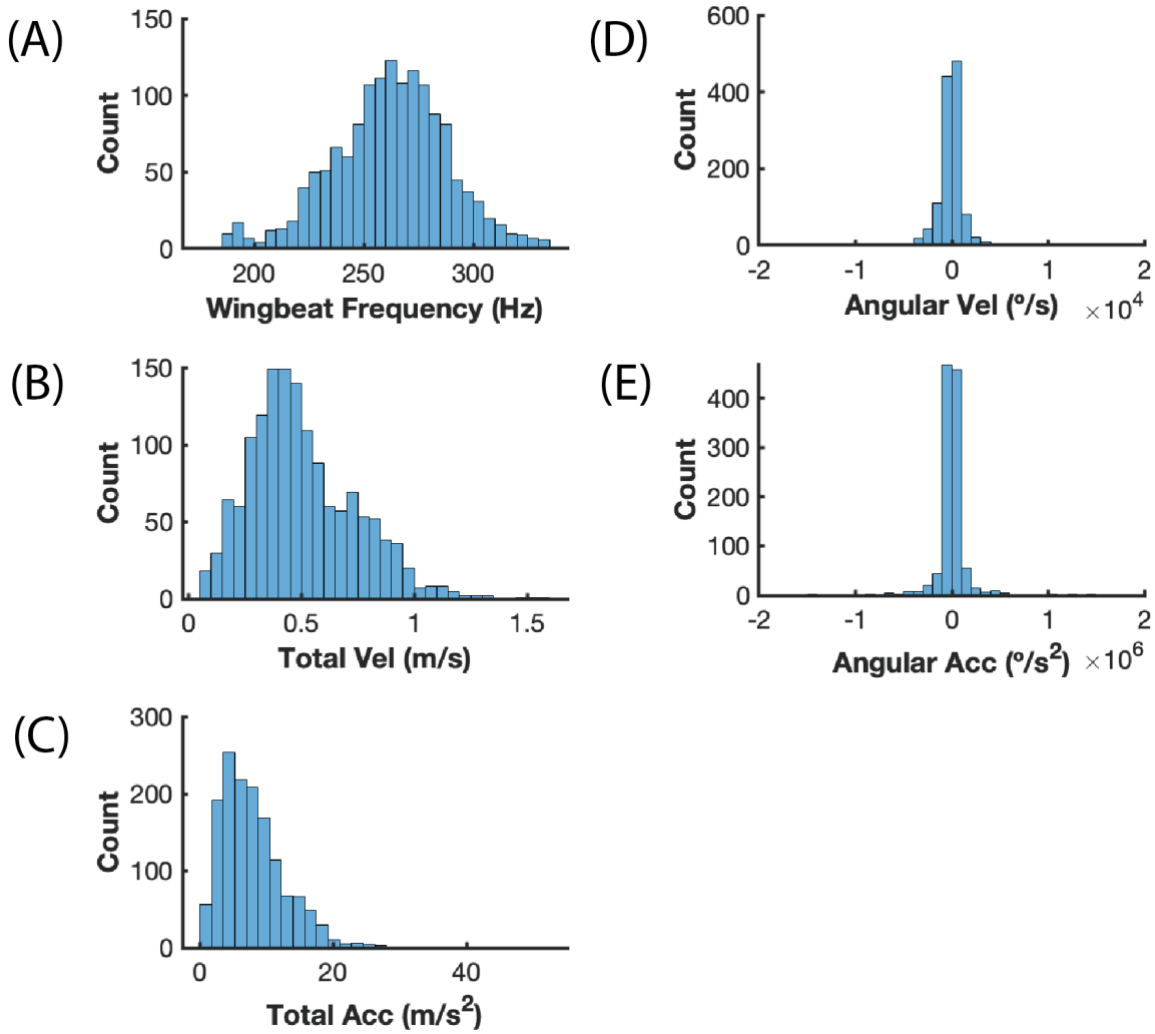

Figure 5.7 Histograms of *Coenosia* flight performance

(A) Wingbeat frequency, (B) total velocity, (C) total body acceleration, (D) angular velocity and (E) angular acceleration. *N* = 1,453 wingbeats.

5.3.3 Body Kinematics

As the killer fly was able to approach the bead/recording volume from any location within the free-flight arena, a range of changes in body yaw was observed (**Figure 5.8A**). However, a change in yaw angle meant that individuals had to decrease flight speed before they could accelerate again (**Figure 5.8B and C**). The greatest change in yaw was 148.5 º in 0.039 seconds (39 ms or ~ 10 wingbeats).

Killer flies varied in body pitch (range - 55.28 to 82.39 º, median 34.95 º and IQR 22.73 º) and roll (range – 192.55 to 200.56 º, median 0.90 º and IQR 35.22 º) as shown in **Figure 5.9A and B.** As well as body yaw (median - 655.98 $º/s^2$ and IQR 9.56 $\times$ 10^4 $º/s^2$), pitch (median - 378.59 $º/s^2$ and IQR 7.81 $\times$ 10^4 $º/s^2$), and roll (median 128.72 $º/s^2$ and IQR 1.75 $\times$ 10^5 $º/s^2$) acceleration (**Figure 5.9C - E**). The maximum body acceleration for yaw, pitch and roll was 6.12 $\times$ 10^6 $º/s^2$, 1.15 $\times$ 10^6 $º/s^2$, and 5.12 $\times$ 10^6 $º/s^2$ respectfully (**Figure 5.9C - E**). Changes in body angle and body angle accelerations over time may also be observed in **Figure 5.10**.

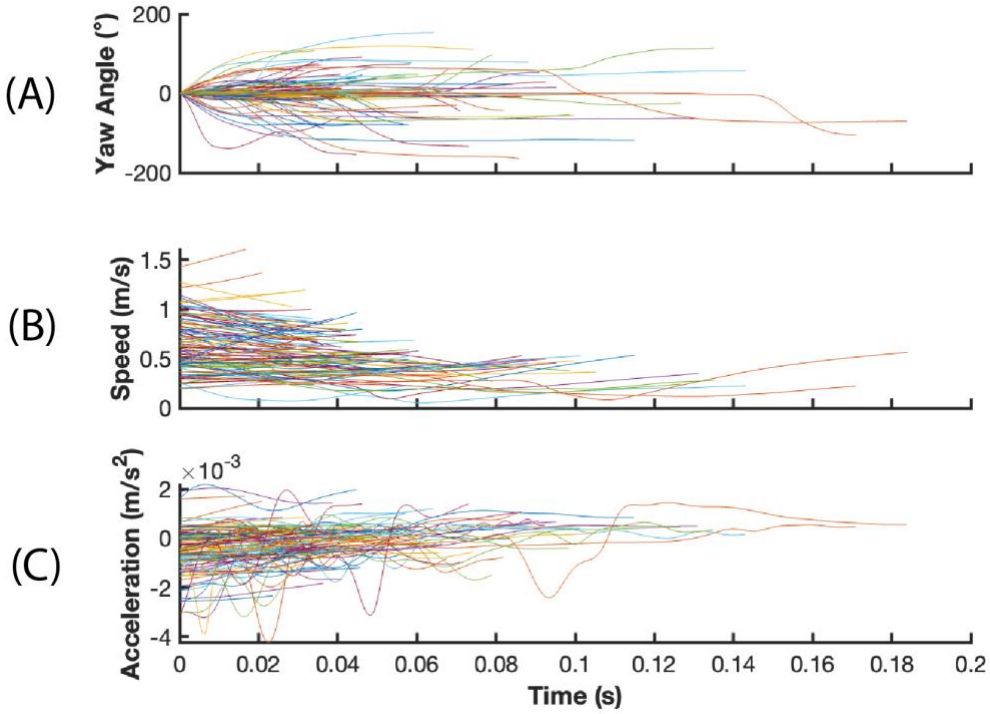

Figure 5.8 Yaw angle, flight speed and acceleration over time

Change in (A) yaw angle, (B) flight speed and (C) acceleration over time for *N* = 110 sequences. Each coloured line represents one sequence.

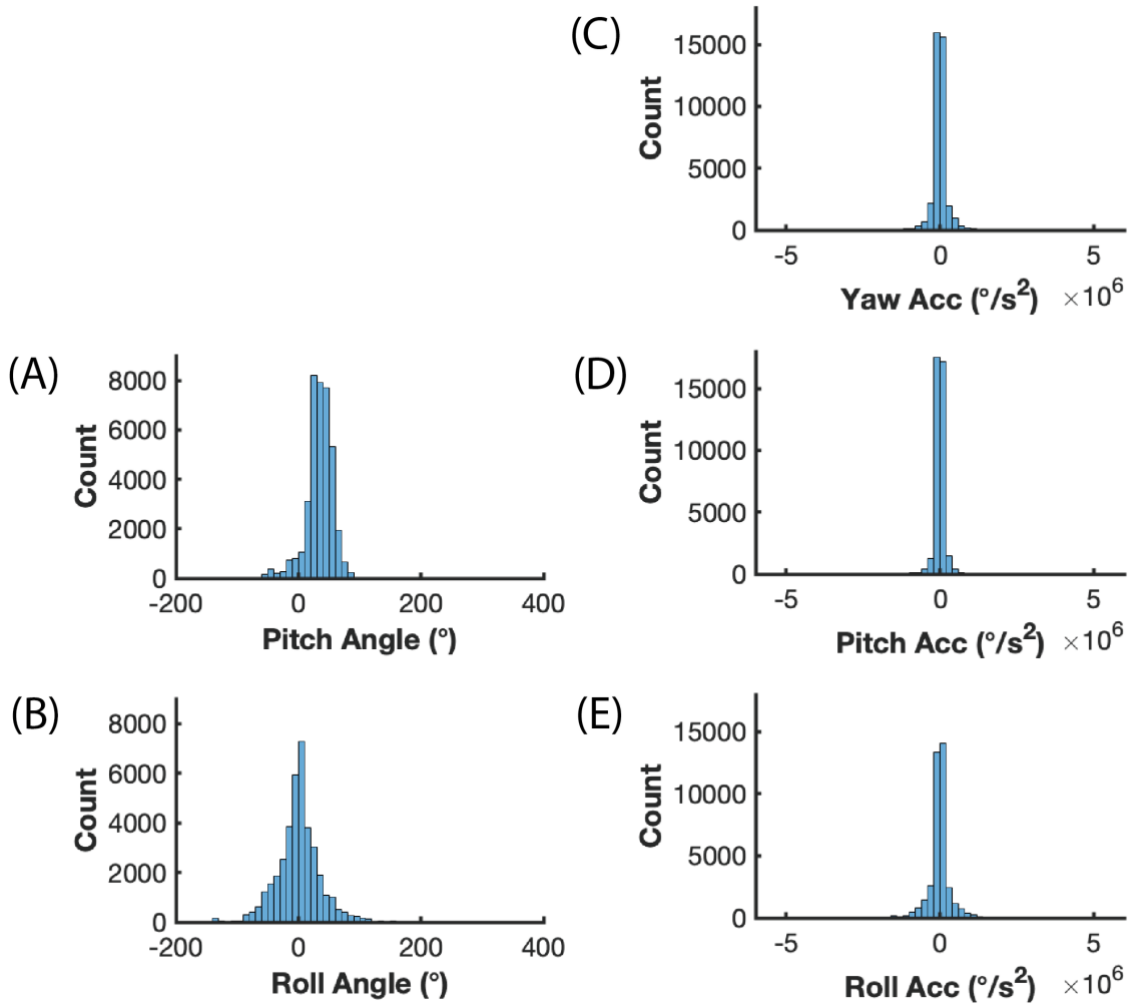

Figure 5.9 Histogram of *Coenosia* body angles and accelerations

(A) Body pitch and (B) roll angle, (C to E) yaw, pitch and roll body accelerations. *N* = 38,671 body positions from *N* = 110 sequences.

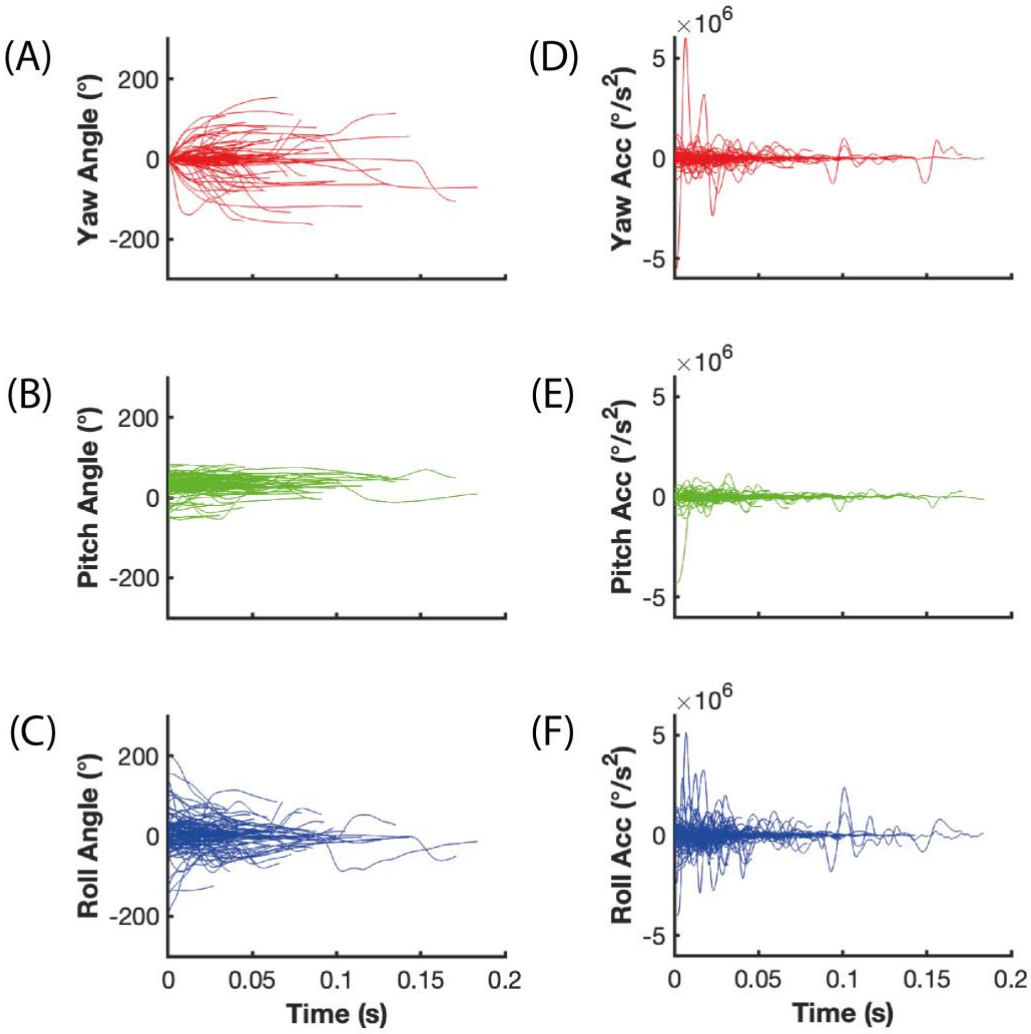

Figure 5.10 Killer fly body angles and accelerations

(A to C) Body angles and (D to F) body accelerations where yaw is red, pitch is green and roll is blue. *N* = 38,671 body positions from *N* = 110 sequences.

5.3.4 Wing Kinematics

Sequences were segregated into stable and unstable wingbeats to show the subtle changes in wing kinematics responsible for the range of body kinematics observed in this study (**Figure 5.11**). Stable wingbeats were defined as wingbeats where linear and angular body acceleration was lower than half the SD of all sequences, and unstable wingbeats were wingbeats that did not meet this criteria (Muijres et al., 2014). Out of the 1,453 wingbeats, 135 were classified as stable and 1,318 as unstable. The mean and SD wingbeat frequency of stable and unstable groups was 272 ± 19 Hz and 266 ± 25 Hz respectfully. Subtle differences in the time-history of left and right wing kinematics (wingtip angles, mid-wing pitch and spanwise bending), can also be seen in **Figure 5.12** at peak yaw, pitch and roll accelerations. Selection of wingbeats accountable for peak body accelerations was defined as those three SDs away from the mean over all wingbeats.

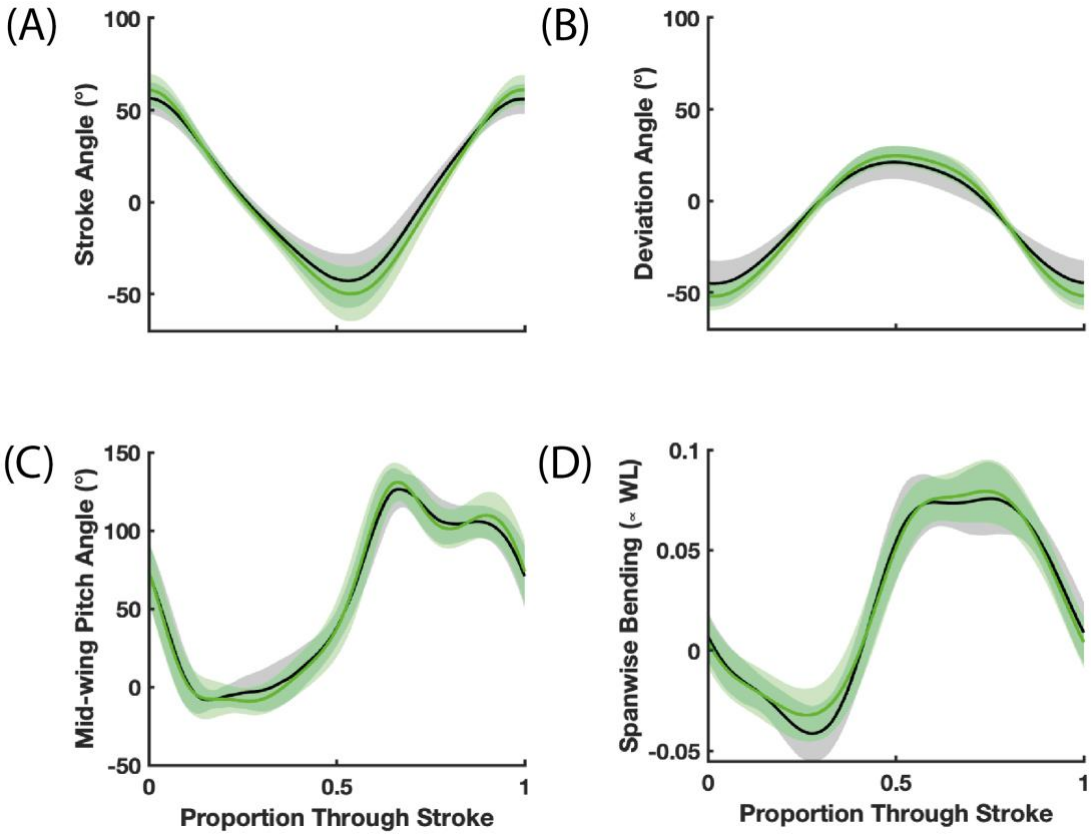

Figure 5.11 Stable and unstable wing kinematic parameters

Stable (grey, *N* = 135 wingbeats) and unstable (green, *N* = 1,318 wingbeats) wing kinematic parameters. (A) Stroke angle, (B) deviation angle, (C) mid-wing pitch angle and (D) spanwise bending as a proportion of wing length (WL). Solid lines are means and shaded bounds are standard deviation.

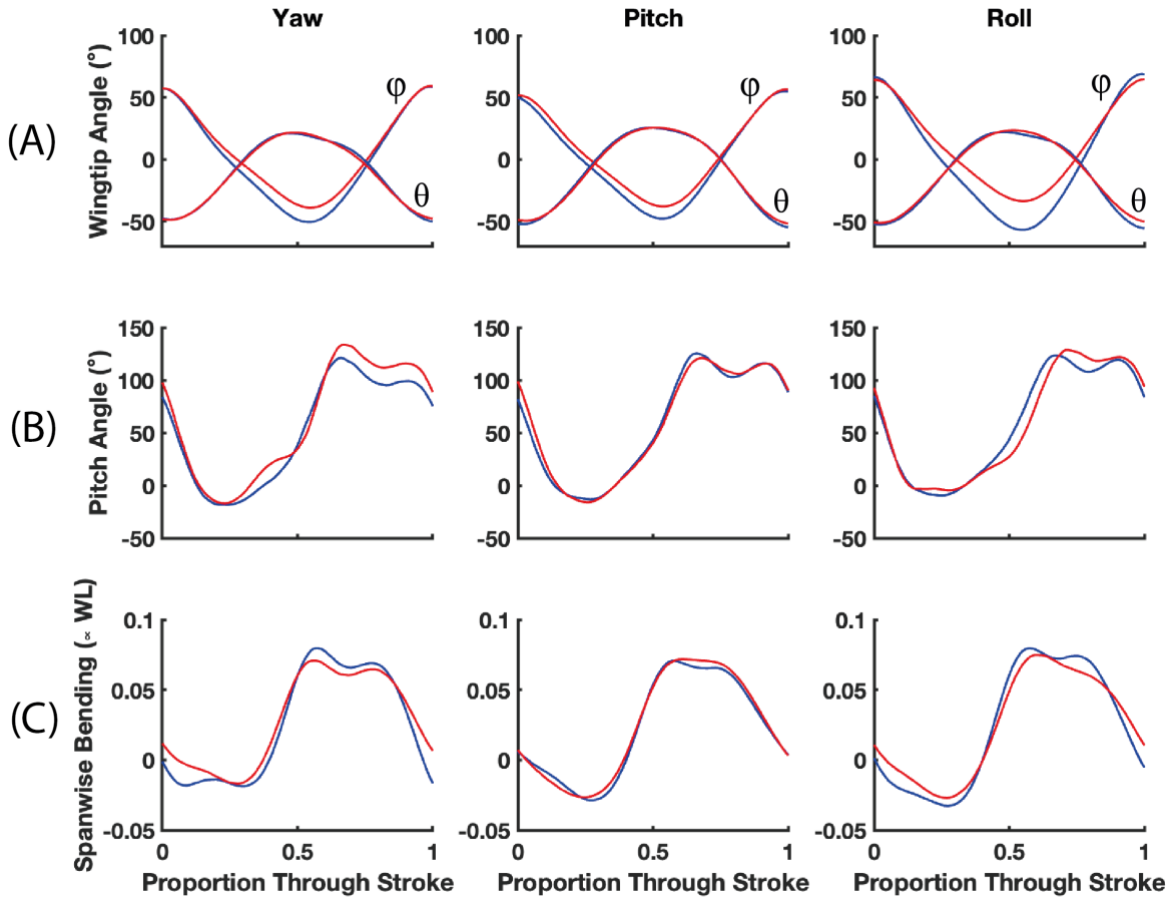

Figure 5.12 Average wing kinematics for peak yaw, pitch and roll accelerations

Average left (blue) and right (red) wing kinematics that produced peak (column one) right yaw from *N* = 8 wingbeats, (column two) pitch up from *N* = 12 wingbeats and (column three) roll accelerations to the right from *N* = 11 wingbeats. Row (A) wing tip angles (stroke angle (**φ**) and deviation angle (**θ**)), (B) mid-wing pitch angle and (C) spanwise pending as a proportion of wing length (WL) respectfully.

5.4 Discussion

Killer flies as sit and wait predators frequently entered the field of view of high-speed cameras in response to stimuli presented. However, no clear pursuit behaviour was observed amongst individuals. Surveillance behaviour may have been observed alternatively, where the insect entered the field of view, surveyed suitability of the prospective target throughout the approach, and then abandoned the chase, although this is yet to be verified. Nonetheless, angular velocities and accelerations observed were extremely high, and it was further reported that *Coenosia* underwent substantial wing deformation during manoeuvres which may have been assumed to be rigid alike *Drosophila* in the past of similar body size and wing length (**Figure 5.13**) (Faruque and Sean Humbert, 2010, Fry et al., 2005). Changes in wing twist dominated phases of stroke reversal, and spanwise bending, a relatively new parameter used to describe wing deformation was further reported for the first time in this species to vary through the stroke.

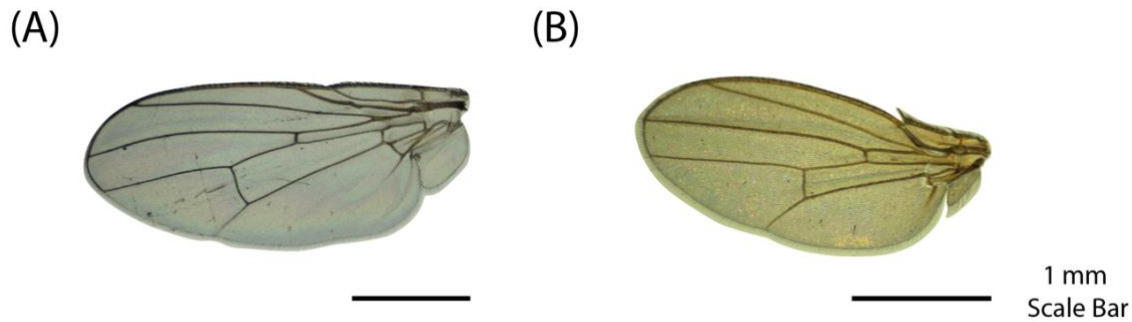

Figure 5.13 *Coenosia* and *Drosophila* wing

Microscope images of (A) *Coenosia* and (B) *Drosophila* wing for size comparison. Approximate wing length of *Coenosia* is 3mm and *Drosophila* is 2.5 mm.

5.4.1 *Coenosia* Response to Stimuli

Flying animals that use PN operate at high speeds and are more manoeuvrable than their targets. However, users (e.g., Harris' hawks (Brighton and Taylor, 2019, Jones et al., 2007)) are typically not limited by vision unlike *Coenosia*. To encourage take off/manoeuvres, it was therefore important that my setup fulfilled requirements such as the bead being of similar size (*Drosophila* body length ~ 2 – 3 mm (Flatt, 2020)) and velocities of natural prey (e.g., 0.54 – 1.23 m/s in (Fabian et al., 2018)). However, as the linear driven stimuli was positioned at the upper limits of the high-speed cameras' views to minimise subject and camera obstruction, pursuit behaviour that may have been performed from above was not captured in recordings. This was also likely as killer flies were frequently seen perched on the upper half of the free-flight arena, and in some sequences, collisions with the spring steel was observed but were excluded from analysis as subjects fell. Initial testing of this stimulus positioned at the bottom of high-speed camera views was done however, insects had the tendency to fly towards the reflections of the bead on the top disc of the free flight arena as they were closer than the physical bead. A larger flight arena was deemed inappropriate as high-speed cameras would have to be positioned further away thus, decreasing the spatial resolution of footage required to calculate wing twist with high-precision.

Alternative stimuli methods were also attempted during the experimental design period such as presenting a moving black circle on a high refresh rate screen positioned outside of the free-flight arena. This was to ensure *Coenosia* perceived the target as a continuously moving object (flicker fusion frequency (FFF), **Section 1.6**). However, further complications arose from screen reflections and

maximising the probability of attack in line with Wardill et al. (2015), where the highest take-off/pursuit probability favoured a target subtended velocity (in degrees/msec) and subtended size (in degrees) ratio of 0.37 (determined by distance of the screen from subjects, and the size and speed of the moving black circle). Furthermore, discrepancies in FFF values from photoreceptor measurements (186 Hz in *Coenosia* (Gonzalez-Bellido et al., 2011)) and behaviour experiments led to the final selection of a physical bead stimulus. *Calliphora* (blowflies) for instance, have been reported to have 240 Hz FFF determined with electrodes (Autrum and Hoffmann, 1960), but recent behavioural studies revealed blowflies to have FFF values as low as 60 Hz (Dixon et al., unpublished).

To verify surveillance behaviour, tracking the head angle independently from the body angle would have been useful. Although this is only possible as *Coenosia* have long necks, and forelimbs remained extended in anticipation of grasping prey (further discussed in **Section 6.3.3**).

5.4.2 *Coenosia* Flight Performance

Sequences captured showed a broad range of flight manoeuvres that were controlled by subtle changes in wing kinematics. These modifications then had a great effect on body kinematics as summarised in **Figures 5.7** and **5.9**. Banked turns performed were stereotypical as changes in yaw and roll were dominant and pitch was minor. Along with delays in flight speed with changes in direction,

and speed increasing again once the turn had been completed. Mujires et al. (2014) and (2015) interestingly described similar banking parameters in escaping *Drosophila*, that typically occurred with mean 93 º changes in heading (range 20 – 180 º), peak turn rate median of 5300 º/s (IQR 3800 – 9000 º/s), and turn durations of 49 ± 18 ms (~ 9 wingbeats). In addition to this, a small increase in wingbeat frequency and less than 5 º change in wingtip and wing pitch angles was seen (Muijres et al., 2015, Muijres et al., 2014). However, total flight velocities of *Coenosia* in this current study (0.503 ± 0.236 m/s) were lower than *Drosophila* (mean 1.3 m/s, range 0.78 – 2.03 m/s) against hunting dragonflies (mean 2.28 m/s) (Combes et al., 2013). That is likely to be explained by *Drosophila* being able to fly freely in a large 7.3 × 7.3 × 4.6 metre enclosure. Although killer flies here were able to achieve greater mean accelerations (8 m/s^2) and angular velocities (816 º/s) than *Drosophila* (5.5 m/s^2 and 776 º/s respectfully) demonstrating their greater flight agility. Differences in acceleration may be explained by greater muscle mass in *Coenosia* but requires further investigation. Whereas the mean angular velocity of killer flies were comparable to hunting dragonflies (*Libellula cyanea*, body length ~ 40 - 48 mm (Combes et al., 2013)) turning at 914 º/s despite being up to 10 times smaller (Combes et al., 2012). But, it is possible that killer flies can reach even higher velocities when hunting.

5.5 Conclusion

This study provided insight on the kinematic steps required for *Coenosia* live action target tracking. Kinematic output (body trajectory) was the result of subtle differences in all wing parameters, including wing torsion and wing bending described for the first time in this species. *Coenosia*'s tendency to perform extreme manoeuvres thereby denoted a high tolerance to manage and correct flight instabilities which rely on the rapid transduction of sensory information from photoreceptors and proprioceptors (**Section 1.6**). Future studies would benefit from refining the prey stimulus to capture successful hunting behaviour with forelimbs when extended anteriorly, in order to quantify head movement independently from the thorax. This species thus remains of importance when wanting to investigate navigation models and when developing highly manoeuvrable MAVs (see **Section 1.1** and **Section 6.3.4**).

Chapter 6

General Discussion

6.1 Summary of Key Findings

This thesis presented novel insights into the free-flight kinematics of pterygotes, which may then feed into studies of insect flight control and aerodynamics. This was facilitated by the development and use of a new and flexible camera rig to capture footage. Footage was then fed into a completely automated voxel-carving package to obtain kinematics of unprecedented resolution, including relatively new descriptors of wing torsion and bending. The first experimental chapter on *Anopheles* was the first to demonstrate the setups capabilities, by enabling me to report to my knowledge, the second largest database of high-precision free-flight kinematics. It was then first discovered that *Anopheles* were able to reduce their stroke amplitude to even smaller angles than previously reported for any flying insect. This was facilitated by the encouragement of flight manoeuvres in subjects which was absent in the previous record (Bomphrey et al., 2017). Secondly, wingtip, wing twist and spanwise bending for all wingbeats was reported, and was found to be significantly different between males and females. Lastly, this chapter highlighted the importance of non-wing appendages for flight control and stability. I presented for the first time, the leg metrics and in depth kinematics of both intact and damaged mosquitoes during free-flight. The leg MOI of intact subjects contributed largely to the stability of mosquitoes in the roll axis and damaged mosquitoes adjusted their leg kinematics in response to leg loss.

In the second experimental chapter of this thesis, male and female *Anopheles* wing summary parameters (wingbeat frequency and stroke amplitude) positively correlated with increasing temperature, and plateaued at different temperatures. Meanwhile, body kinematics did not correlate with temperature but with the exception of female body pitch that correlated weakly. This overall poor relationship between body kinematics and varying temperature, thus meant that this large dataset could also undergo Fourier fitting (to summarise time varying data) and PCA (to create a set of independent parameters and identify which are most important to describe data variation), to create a descriptor wingbeat that enabled testing of the effect of temperature. In total, a minimum of 7, 16 and 7 PCs was sufficient to describe more than 99 % of variation in 12,578 wingbeats for wingtip, mid-wing pitch and spanwise camber respectfully. PC scores were then tested/validated with kinematic reconstruction to predict changes in stroke amplitude, stroke plane and timing of supination with temperature.

The final experimental chapter aimed to describe the body kinematics and operating time scales of highly manoeuvrable *Coenosia*. This was done to exhibit their flight agility and for comparison against other aerial predators and escaping insects of similar size. Though *Coenosia* did not exhibit pursuit behaviour, this study still revealed incredibly high angular rates and accelerations whilst insects maintained subtle differences in wing kinematics for peak yaw, pitch and roll acceleration. Manoeuvres performed against the two types of artificial prey presented, ranged from upside down flight to flying backwards that is not typical behaviour of other flying insects. It was further speculated that *Coenosia* here was instead exhibiting surveillance behaviour, as subjects frequently approached and exited the field of view of high-speed cameras.

6.2 Insect Free-flight Lab

The methods and use of photogrammetry are well established and rehearsed. Observational studies of these miniature animals in literature have therefore utilised this technique frequently, whilst heavily relying on the accuracy of camera calibrations to calculate 3D coordinates from 2D image coordinates (Aber et al., 2010, Matthews, 2008, Walker et al., 2009). However, previous setups and data processing pathways fall short in multiple areas (e.g., limited camera views and lead to laborious data analysis) to limit photogrammetry use to its maximum potential. This then led to the development of the ten high-speed camera rig detailed in **Section 2.2** to obtain high-precision insect free-flight kinematics. In this section I thereby discuss some considerations for its design and settings used during data collection.

Multiple designs of the free flight arena was explored before determining its cylinder shape and dimensions. To minimise image distortion in a sphere or hemisphere shaped arena, surfaces must be thin and require uniform thickness which can be difficult to achieve in plastic forming processes. The cylinder design had the additional advantage of surfaces (walls and top/bottom discs) being easy to replace in the event of scratches, or altered e.g., to insert a hole for stimuli. Meanwhile, cameras operated on camera rails to adjust distance rather than paired with zoom lenses to avoid barrel or pincushion distortion of images (Drap and Lefèvre, 2016). Sequences were also filmed in monochrome due to the nature of coloured sensors that result in overall less light absorption (low light sensitivity), and lower resolution images (Weber and Menko, 2005).

In addition to calibrations taken at the start and end of data collection days, care was further taken to take calibrations during the day in case cameras were accidently knocked. Camera positions (i.e. camera rails were evenly spaced out around scaffolding) and settings were optimised for each species investigated. However, trade-offs between image resolution (camera sensor dependent), insect behaviour, and wing length also came into play. Mosquitoes with high wingbeat frequencies and aspect ratio wings, meant that 15 frames per wingbeat (if beating at 800 Hz) at 12,000 fps at 768 × 720 px resolution deemed most appropriate, even though the maximum frame rate of the high-speed cameras was 540,000 fps (at 128 × 16 px resolution, FASTCAM Mini AX200, Photron Ltd).

Far-red LEDs were synchronised to the shutter speeds of high-speed cameras for full brightness using a LED driver (fitted with a monostable multi-vibrator) that detected frame rate and produced a pulse at a restricted current. This was done to strobe the lights via modulation of square waves and duty cycle to minimise excessive light exposure that may damage sensors over time, and to create short exposure times to reduce motion blur. Asynchronies (lag) in exposure time due to signalling delays between cameras, LED drivers, receive times, and LED rise and fall times were easily identified as fluctuations or large differences in brightness in all high-cameras.

It has been long understood that there are trade-offs when investigating insect flight with a free-flight or tethered approach. One must therefore be careful when interpreting/linking results of free-flight and tethered literature. Tethered insects do not require weight support, meaning that kinematics documented are likely inaccurate to how the insect would behave in nature (Snelling et al., 2012).

Discrepancies in summary parameters such as wingbeat frequency for instance, indicates major behavioural/time variable differences in wing kinematics during free-flight (Arthur et al., 2014, Cator et al., 2011). It is thereby important that further studies where weight support is important, use kinematics obtained from free-flight experiments although it is understandable that tethered approaches are sometimes necessary. For instance, delicate electromyography experiments that investigate the relationship between steering muscle activation and its kinematic output (Balint and Dickinson, 2001, Balint and Dickinson, 2004).

6.3 Future Perspectives

6.3.1 Take Off

Flight initiation requires a robust sequence of events, suited to both internal (e.g., hunger) and environmental (e.g., visual) stimuli, to swiftly transition from terrestrial to aerial modes of locomotion. However, surprisingly little research has been done on the initial events of insect flight, from wing unfolding to lift-off in comparison to aerial kinematics. It would therefore be interesting to adapt the free-flight arena and fly tracker code to obtain high-precision body, leg and wing kinematics of *Anopheles* and *Coenosia* pre-lift off, and during take-off.

Before taking off, several insect orders jump using their tegro-trochanter muscle (TTM) to drive femur extension of their meso-thoracic limb (Schouest Jr et al., 1986). The TTM is a synchronous muscle although arranged alongside asynchronous muscle within the thorax, where only after its firing, asynchronous power muscle (DVM and DLM) oscillations can begin (Levine, 1973). Though, it has been reported that mosquitoes do not have TTMs as powerful jumps could alert their prey when fleeing (Smith et al., 2020). Instead they have extracoxal depressor trochanter muscles (EDT), EDT1 for forelimb, EDT2 for midlimb, and EDT3 for hindlimb push off (Muijres et al., 2017). Thereby raising questions on how mosquitoes with limb damage take-off, and how their COM positioning and ground reaction force of each limb may differ in comparison to intact mosquitoes (Li et al., 2011). Furthermore, it is possible that leg kinematics underwent the greatest change during take-off, and immediately after take-off that was not

captured in the footage described in **Chapter 3**. Mosquitoes may have therefore already adjusted their leg and wing kinematics to compensate for leg loss before entering the view of high-speed cameras for flight stability. Additional footage of mosquito take-off could therefore be valuable for further understanding how flight stability is achieved.

To my knowledge, no research has been done on *Coenosia* take-off. As sit and wait predators, take-off must be extremely vital to launch themselves towards prey. It may therefore be speculated that *Coenosia* behave similarly to *Drosophila* during escape take-offs, where *Drosophila* have been reported to adjust their posture, and so the position of their COM away from looming threats 200 ms before taking off in the same direction (Card and Dickinson, 2008). It is further unknown if *Coenosia* jump during take-off or benefit from aerodynamic ground effect (Rayner and Bone, 1997). This is where airflow accelerated towards the ground generally benefits lift generation, and decreases drag as upwash interacting with the surface below decreases downwash momentum to reduce induced power (Kolomenskiy et al., 2016, Dudley, 2000b). Although the significance of aerodynamic ground effect varies in literature. Truong et al. (2013) for example, revealed that non-jumping rhinoceros beetles (*Trypoxylus dichotomus*) benefited from ground effect, as total vertical force increased by 18.4 % and 8.6 % in their first and second wing stroke respectively (Truong et al., 2013). Whereas, Van Veen et al. (2019) reported negligible ground effect in mosquitoes (*Anopheles coluzzii*) during take offs. Differences described above are likely to be explained by a number of variables such as insect size, wing morphology and kinematics, and therefore cannot be anticipated.

Detail on *Anopheles* and *Coenosia* take-off, will further highlight the importance of morphology and kinematics to suit their lifestyles even though both *Diptera*.

6.3.2 Mosquito

Although my findings novel, my study on *Anopheles* inevitably raised further questions as to why wingbeat frequency of male and female mosquitoes increased significantly with temperature. As the change in air density was insufficient to fully explain the latter, further research is required to better understand the complex interaction between environmental conditions (temperature and humidity), underlying energetics and effect on wingbeat frequency. This may be approached with a combination of respirometry and thermal techniques to quantify the operating temperature of flight muscle, that can then be used to provide insight on flight efficiency. During respirometry, organismal oxygen consumption ($\dot{V}O2$) or carbon dioxide output ($\dot{V}CO2$) during aerobic respiration can be used to calculate chemical input and estimate metabolic rate. To supplement this, monitoring heat loss may also be used to calculate chemical input and estimate metabolic rate as it is a by-product of metabolism. To estimate thoracic/flight muscle temperature, using a thermal imaging camera rather than placing a thermocouple within the thorax is likely to be more appropriate due to their small size. However, monitoring changes in atmospheric temperature with a thermal camera before equilibrium to room temperature may be challenging. Consequently, these techniques could not be incorporated into the high-speed camera rig for simultaneous recordings, as

respirometry requires a small sealed chamber in order to identify small fluctuations in gas concentration that may restrict natural flight.

6.3.3 Killer Fly

Future work on *Coenosia* should focus on prey interception and sensory elements that facilitate their manoeuvrability. During my research, *Coenosia* were identified to have surprisingly long necks that may increase head mobility ideal for high manoeuvrability, in comparison to *Drosophila* and *Calliphora* (also both *Diptera*), where the head is commonly attached to the thorax almost abruptly (**Figure 6.1**). It was also identified that in some sequences *Coenosia* were flying with forelimbs sprawled forwards in preparation for grasping and grappling their prey (Gonzalez-Bellido, UMN, pers comms). The features described above and their distinct antennae, as a result enabled the calculation of heading angle (independent from the body) in a preliminary sequence. Head movement preceding take-off and during flight towards prey would be a strong indication of target tracking as the compound eye's line of sight is fixed and to keep the target within a cell-dense region (Bomphrey et al., 2016). However, this leg spawling behaviour was not consistent and occurred at low frequencies in my dataset, and was thus likely a hunting response towards bead reflections or other *Coenosia* within the free-flight arena as subjects did not show signs of pursuit behaviour against the physical bead.

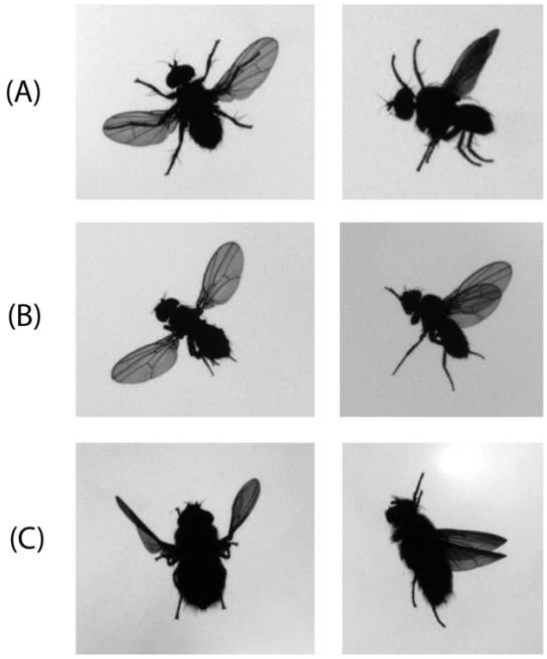

Figure 6.1 Insect appearance in high-speed cameras

Row (A) killer fly, row (B) fruit fly and row (C) blowfly. Killer flies have relatively long necks in comparison to fruit flies and blowflies, that may be used in future studies to calculate head angle independently from the rest of the body. Not to scale.

6.3.4 Application to Biomimetics

Several micro-air vehicles (MAVs) have adopted the flapping mechanism of insects, and operate at similar spatiotemporal scales (Fuller et al., 2014, Jafferis et al., 2019). However, most MAVs do not mimic insect flight beyond this. This is due to a number of reasons such as weight restrictions for power supplies and hardware for continuous sensory feedback (e.g., sensors and adjustable actuators) that must be within the limits of the lift generating wings. To therefore optimise flight efficiency and to achieve maximum manoeuvrability, the

development of light weight biomimetic materials is vital. Recent work on insect wing biomimicry introduced 3D printed polypropylene wings (Saito et al., 2021), laser cut and bonded Mylar and carbon fibre (Liu et al., 2017), and UV-curable polymers for wing topographies (Reid et al., 2021) but, this research topic continues to require much greater attention. The work presented here will therefore provide an in-depth target of how artificial wings should behave when developing highly deformable flapping wings in their spanwise and chordwise directions.

6.3.5 Aerodynamic Modelling

High-precision and in-depth kinematic data is required to accurately estimate aerodynamic forces. One approach of estimating flight forces is blade element theory (BET) that involves a quasi-steady state assumption, meaning that time history is assumed unimportant. In summary, BET splits the wing into a series of chordwise slices (blade elements), aerodynamic forces of each slice is then calculated independently and summed (Walker and Taylor, 2021, Ellington and Lighthill, 1997). However, this method is likely to give inaccurate results of aerodynamic force production in *Anopheles* but maybe sufficient for *Coenosia* force estimations if wanting quick results. For the reason that, *Anopheles* use lift generating methods, TEV and rotational drag during stroke reversal (wing flapping rotational phase (Bomphrey et al., 2017)) where time history of surrounding fluid is extremely important as fluid flow is re-encountered. Whereas, *Coenosia* are more likely to use more conventional unsteady lift generating

methods (e.g., LEV) with their relatively large stroke amplitudes during wing translation, although this is yet to be verified and it would be interesting to see how aerodynamic forces of *Coenosia* compare to other *Diptera* and other insects of similar size when manoeuvring.

For *Anopheles*, I alternatively propose computational fluid dynamics (CFD) for aerodynamic modelling, which is now a fairly mature field but has been limited by the paucity of accurate kinematic data (i.e., lacking wing deformation that is important and pronounced in many insect species) of insects (Liu and Kawachi, 1998, Liu et al., 1998). During CFD, a mesh model of the wing and environment is first generated. Fluid flows are then simulated by solving Navier-Stokes equations iteratively for each cell to get e.g., wing surface pressure distributions and vertical velocity flow profiles.

Some preliminary CFD simulation results can be seen in **Figure 6.2,** using the male reconstructed wingbeats described in **Chapter 4** at 22, 25, 28 and 31 ºC. Aerodynamic power increased as temperature increased, peaking the most at ~ 41 μW at 0.6 t/T with 31 ºC reconstructed kinematics, thereby prompting further investigation into the wing kinematics responsible and why mosquitoes flap at such high wingbeat frequencies (e.g., from a muscle physiology or neurophysiology perspective).

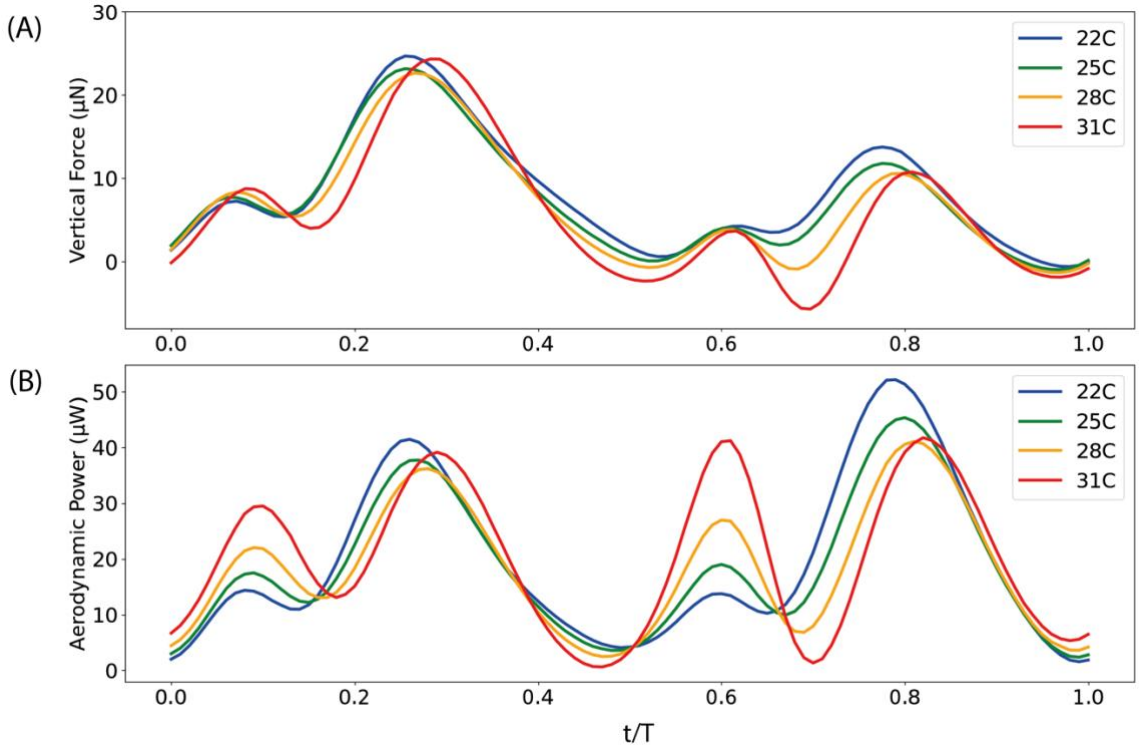

Figure 6.2 Preliminary results of Mosquito CFD

(A) Vertical force and (B) aerodynamic power through a male mosquito wingbeat cycle at 22 ºC (blue), 25 ºC (green), 28 ºC (yellow) and 31 ºC (red). t/T is a proportion through the wingbeat starting from pronation (t/T = 0). Figure generated by collaborators Richard Bomphrey and Marcos Georgiades, RVC.

6.4 Concluding Remarks

In this thesis I presented a new guideline/standard of reporting high-precision body, leg and wing kinematics. Findings presented further provided insight on the magnitude of wing deformation on two very different insect species *Anopheles* and *Coenosia* (e.g., in body morphology and flight ability), the importance of non-wing appendages on overall flight performance, and methods of handling large amounts of data often faced when investigating insect flight.

List of References

ABER, J. S., MARZOLFF, I. & RIES, J. B. 2010. Chapter 3 - Photogrammetry. *In:* ABER, J. S., MARZOLFF, I. & RIES, J. B. (eds.) *Small-Format Aerial Photography.* Amsterdam: Elsevier.

AGIANIAN, B., KRZIC, U., QIU, F., LINKE, W. A., LEONARD, K. & BULLARD, B. 2004. A troponin switch that regulates muscle contraction by stretch instead of calcium. *The EMBO journal,* 23**,** 772-779.

ALBERTZ, J. Albrecht Meydenbauer – Pioneer of Photogrammetric Documentation of the Cultural Heritage. Proceedings 18th International Symposium CIPA, 2001 Potsdam (Germany).

ALDERSLEY, A. & CATOR, L. J. 2019. Female resistance and harmonic convergence influence male mating success in Aedes aegypti. *Scientific Reports,* 9**,** 2145.

ALDRIDGE, H. D. 1987. Turning flight of bats. *Journal of Experimental Biology,* 128**,** 419-425.

ALMUDI, I., VIZUETA, J., WYATT, C., DE MENDOZA, A., MARLÉTAZ, F., FIRBAS, P., FEUDA, R., MASIERO, G., MEDINA, P., ALCAINA-CARO, A., CASARES, F., GOMEZ-GARRIDO, J., GUT, M., ALIOTO, T., VARGAS-CHAVEZ, C., DAVIE, K., MISOF, B., GONZÁLEZ, J., AERTS, S. & MAESO, I. 2020. Genomic adaptations to aquatic and aerial life in mayflies and the origin of insect wings. *Nature Communications,* 11**,** 2631.

ARTHUR, B. J., EMR, K. S., WYTTENBACH, R. A. & HOY, R. R. 2014. Mosquito (Aedes aegypti) flight tones: frequency, harmonicity, spherical spreading, and phase relationships. *The Journal of the Acoustical Society of America,* 135**,** 933-941.

AUTRUM, H. & HOFFMANN, C. 1960. Diphasic and monophasic responses in the compound eye of Calliphora. *Journal of Insect Physiology,* 4**,** 122-127.

BALINT, C. N. & DICKINSON, M. H. 2001. The correlation between wing kinematics and steering muscle activity in the blowfly Calliphora vicina. *Journal of Experimental Biology,* 204**,** 4213.

BALINT, C. N. & DICKINSON, M. H. 2004. Neuromuscular control of aerodynamic forces and moments in the blowfly, Calliphora vicina. *Journal of Experimental Biology,* 207**,** 3813-3838.

BARTH, F. G. & HOLLER, A. 1999. Dynamics of Arthropod Filiform Hairs. V. The Response of Spider Trichobothria to Natural Stimuli. *Philosophical Transactions: Biological Sciences,* 354**,** 183-192.

BEERSMA, D. G. M., STAVENGA, D. G. & KUIPER, J. W. 1977. Retinal lattice, visual field and binocularities in flies. *Journal of comparative physiology,* 119**,** 207-220.

BELTON, P. 1986. Sounds of Insects in Flight. *In:* DANTHANARAYANA, W. (ed.) *Insect Flight.* Berlin, Heidelberg: Springer Berlin Heidelberg.

BENJAMINI, Y. & HOCHBERG, Y. 1995. Controlling the False Discovery Rate: A Practical and Powerful Approach to Multiple Testing. *Journal of the Royal Statistical Society. Series B (Methodological),* 57**,** 289-300.

BENNET-CLARK, H. C. & DAWS, A. G. 1999. Transduction of mechanical energy into sound energy in the cicada Cyclochila australasiae. *Journal of Experimental Biology,* 202**,** 1803-1817.

BERNARD, G. D. & STAVENGA, D. G. 1979. Spectral sensitivities of retinular cells measured in intact, living flies by an optical method. *Journal of comparative physiology,* 134**,** 95-107.

BERTHÉ, R. & LEHMANN, F.-O. 2015. Body appendages fine-tune posture and moments in freely manoeuvring fruit flies. *Journal of Experimental Biology,* 218**,** 3295-3307.

BIEWENER, A. & PATEK, S. 2018a. Insect flight muscle mechanics. *Animal Locomotion.* 2 ed.: OUP Oxford.

BIEWENER, A. & PATEK, S. 2018b. Movement in Air. *Animal Locomotion.* 2 ed. Oxford: Oxford University Press.

BIEWENER, A. & PATEK, S. 2018c. Neuromuscular Control of Movement. *Animal Locomotion.* 2 ed.: OUP Oxford.

BLACKWELL, A. 2008. Biting Midges, Culicoides spp. (Diptera: Ceratopogonidae). *In:* CAPINERA, J. L. (ed.) *Encyclopedia of Entomology.* Dordrecht: Springer Netherlands.

BODMER, H. 2023. *Common Green Darner: Small Wonders* [Online]. University of Minnesota: Department of Entomology. Available: https://entomology.umn.edu/common-green-darner [Accessed].

BOERGENS, K. M., KAPFER, C., HELMSTAEDTER, M., DENK, W. & BORST, A. 2018. Full reconstruction of large lobula plate tangential cells in Drosophila from a 3D EM dataset. *PLOS ONE,* 13**,** e0207828.

BOMPHREY, R. J., NAKATA, T., HENNINGSSON, P. & LIN, H.-T. 2016. Flight of the dragonflies and damselflies. *Philosophical Transactions of the Royal Society B: Biological Sciences,* 371**,** 20150389.

BOMPHREY, R. J., NAKATA, T., PHILLIPS, N. & WALKER, S. M. 2017. Smart wing rotation and trailing-edge vortices enable high frequency mosquito flight. *Nature,* 544**,** 92-95.

BOUYER, J., CULBERT, N. J., DICKO, A. H., PACHECO, M. G., VIRGINIO, J., PEDROSA, M. C., GARZIERA, L., PINTO, A. T. M., KLAPTOCZ, A., GERMANN, J., WALLNER, T., SALVADOR-HERRANZ, G., HERRERO, R. A., YAMADA, H., BALESTRINO, F. & VREYSEN, M. J. B. 2020. Field performance of sterile male mosquitoes released from an uncrewed aerial vehicle. *Science Robotics,* 5**,** eaba6251.

BRANDON, S. C. E., GRAHAM, R. B., ALMOSNINO, S., SADLER, E. M., STEVENSON, J. M. & DELUZIO, K. J. 2013. Interpreting principal components in biomechanics: Representative extremes and single component reconstruction. *Journal of Electromyography and Kinesiology,* 23**,** 1304-1310.

BRIGHTON, C. H. & TAYLOR, G. K. 2019. Hawks steer attacks using a guidance system tuned for closepursuit of erratically manoeuvring targets. *Nature Communications,* 10**,** 2462.

BRISCOE, A. D. & CHITTKA, L. 2001. THE EVOLUTION OF COLOR VISION IN INSECTS. *Annual Review of Entomology,* 46**,** 471-510.

BUCHWALD, R. & DUDLEY, R. 2010. Limits to vertical force and power production in bumblebees (Hymenoptera: Bombus impatiens). *Journal of Experimental Biology,* 213**,** 426-432.

BULLARD, B., BURKART, C., LABEIT, S. & LEONARD, K. 2006. The function of elastic proteins in the oscillatory contraction of insect flight muscle. *Journal of Muscle Research & Cell Motility,* 26**,** 479-485.

BURKHARDT, D. & DE LA MOTTE, I. 1983. How stalk-eyed flies eye stalk-eyed flies: Observations and measurements of the eyes ofCyrtodiopsis whitei (Diopsidae, Diptera). *Journal of comparative physiology,* 151**,** 407-421.

BUSCHBECK, E. K. & FRIEDRICH, M. 2008. Evolution of Insect Eyes: Tales of Ancient Heritage, Deconstruction, Reconstruction, Remodeling, and Recycling. *Evolution: Education and Outreach,* 1**,** 448-462.

BUSTAMANTE, J., JR., AHMED, M., DEORA, T., FABIEN, B. & DANIEL, T. L. 2022. Abdominal Movements in Insect Flight Reshape the Role of Non-Aerodynamic Structures for Flight Maneuverability I: Model Predictive Control for Flower Tracking. *Integrative Organismal Biology,* 4**,** obac039.

CALLAHAN, A. G., ROSS, P. A. & HOFFMANN, A. A. 2018. Small females prefer small males: size assortative mating in Aedes aegypti mosquitoes. *Parasites & Vectors,* 11**,** 445.

CAO, T. & JIN, J. P. 2020. Evolution of Flight Muscle Contractility and Energetic Efficiency. *Frontiers in Physiology,* 11: 1038.

CARD, G. & DICKINSON, M. 2008. Performance trade-offs in the flight initiation of *Drosophila*. *Journal of Experimental Biology,* 211**,** 341.

CASAS, J. & DANGLES, O. 2009. Physical Ecology of Fluid Flow Sensing in Arthropods. *Annual Review of Entomology,* 55**,** 505-520.

CATOR, L. J., ARTHUR, B. J., PONLAWAT, A. & HARRINGTON, L. C. 2011. Behavioral observations and sound recordings of free-flight mating swarms of Ae. Aegypti (Diptera: Culicidae) in Thailand. *Journal of Medical Entomology,* 48**,** 941-946.

CATOR, L. J., NG'HABI, K. R., HOY, R. R. & HARRINGTON, L. C. 2010. Sizing up a mate: variation in production and response to acoustic signals in Anopheles gambiae. *Behavioral Ecology,* 21**,** 1033-1039.

CHANCE, F. S. 2019. Dragonfly-Inspired Algorithms for Intercept Trajectory Planning. US Department of Energy by National Technology & Engineering Solutions of Sandia: Sandia National Laboratories.

CHAPMAN, R. F., SIMPSON, S. J. & DOUGLAS, A. E. 2013. Muscles. *The Insects: Structure and Function.* 5 ed.: Cambridge University Press.

COLEMAN, D., BENEDICT, M., HRISHIKESHAVAN, V. & CHOPRA, I. 2015. Design, Development and Flight-Testing of a Robotic Hummingbird. *American Helicopter Society 71st Annual Forum.* Virginia Beach, VA.

COMBES, S. A. & DUDLEY, R. 2009a. Turbulence-driven instabilities limit insect flight performance. *Proceedings of the National Academy of Sciences,* 106**,** 9105-9108.

COMBES, S. A. & DUDLEY, R. 2009b. Turbulence-driven instabilities limit insect flight performance. *Proceedings of the National Academy of Sciences,* 106**,** 9105.

COMBES, S. A., RUNDLE, D. E., IWASAKI, J. M. & CRALL, J. D. 2012. Linking biomechanics and ecology through predator–prey interactions: flight performance of dragonflies and their prey. *Journal of Experimental Biology,* 215**,** 903-913.

COMBES, S. A., SALCEDO, M. K., PANDIT, M. M. & IWASAKI, J. M. 2013. Capture Success and Efficiency of Dragonflies Pursuing Different Types of Prey. *Integrative and Comparative Biology,* 53**,** 787-798.

CONLEY, K. E. & LINDSTEDT, S. L. 2002. Energy-saving mechanisms in muscle: the minimization strategy. *Journal of Experimental Biology,* 205**,** 2175-2181.

COSENS, D. & LEBLANC, N. 1980. Frequency dependent flicker response enhancement in the lamina ganglionaris of Drosophila. *Journal of comparative physiology,* 137**,** 341-351.

CRIBELLIER, A., STRAW, A. D., SPITZEN, J., PIETERS, R. P. M., VAN LEEUWEN, J. L. & MUIJRES, F. T. 2022. Diurnal and nocturnal mosquitoes escape looming threats using distinct flight strategies. *Current Biology,* 32**,** 1232-1246.e5.

DAWSON, J. W., DAWSON-SCULLY, K., ROBERT, D. & ROBERTSON, R. M. 1997. Forewing asymmetries during auditory avoidance in flying locusts. *Journal of Experimental Biology,* 200**,** 2323-2335.

DICKINSON, M. H. 1990. Linear and Nonlinear Encoding Properties of an Identified Mechanoreceptor on the Fly Wing Measured with Mechanical Noise Stimuli. *Journal of Experimental Biology,* 151**,** 219-244.

DICKINSON, M. H. 1999. Haltere–mediated equilibrium reflexes of the fruit fly, Drosophila melanogaster. *Philosophical Transactions of the Royal Society of London. Series B: Biological Sciences,* 354**,** 903-916.

DICKINSON, M. H., LEHMANN, F.-O. & SANE, S. P. 1999. Wing Rotation and the Aerodynamic Basis of Insect Flight. *Science,* 284**,** 1954-1960.

DICKINSON, M. H. & MUIJRES, F. T. 2016. The aerodynamics and control of free flight manoeuvres in Drosophila. *Philosophical Transactions of the Royal Society B: Biological Sciences,* 371**,** 20150388.

DICKINSON, M. H. & TU, M. S. 1997. The Function of Dipteran Flight Muscle. *Comparative Biochemistry and Physiology Part A: Physiology,* 116**,** 223-238.

DIXON, A. R. & VONDRA, I. 2022. Biting Innovations of Mosquito-Based Biomaterials and Medical Devices. *Materials* [Online], 15.

DÖRING, T. & SPAETHE, J. 2009. Measurements of Eye size and Acuity in Aphids (Hemiptera: Aphididae). *Entomologia Generalis,* 32**,** 77-84.

DRAP, P. & LEFÈVRE, J. 2016. An Exact Formula for Calculating Inverse Radial Lens Distortions. *Sensors* [Online], 16.

DUDLEY, R. 2000a. *The Biomechanics of Insect Flight: Form, Function, Evolution*, Princeton University Press.

DUDLEY, R. 2000b. Kinematics and Aerodynamics of Flight. *The Biomechanics of Insect Flight.* Princeton University Press.

DUDLEY, R. 2000c. Neuromuscular Control of Movement. *The Biomechanics of Insect Flight: Form, Function, Evolution.* Princeton University Press.

ELDREDGE, J. D. & JONES, A. R. 2019. Leading-Edge Vortices: Mechanics and Modeling. *Annual Review of Fluid Mechanics,* 51**,** 75-104.

ELLINGTON, C. P. 1984. The Aerodynamics of Hovering Insect Flight. II. Morphological Parameters. *Philosophical Transactions of the Royal Society of London. Series B, Biological Sciences,* 305**,** 17-40.

ELLINGTON, C. P. & LIGHTHILL, M. J. 1984a. The Aerodynamics of Hovering Insect Flight. IV. Aerodynamic mechanisms. *Philosophical Transactions of the Royal Society of London. B, Biological Sciences,* 305**,** 79-113.

ELLINGTON, C. P. & LIGHTHILL, M. J. 1984b. The Aerodynamics of Hovering Insect Flight. VI. Lift and Power Requirements. *Philosophical Transactions of the Royal Society of London. B, Biological Sciences,* 305**,** 145-181.

ELLINGTON, C. P. & LIGHTHILL, M. J. 1997. The aerodynamics of hovering insect flight. V. A vortex theory. *Philosophical Transactions of the Royal Society of London. B, Biological Sciences,* 305**,** 115-144.

ELLINGTON, C. P., VAN DEN BERG, C., WILLMOTT, A. P. & THOMAS, A. L. R. 1996. Leading-edge vortices in insect flight. *Nature,* 384**,** 626-630.

ESCALANTE, I. & ELIAS, D. O. 2021. The type of leg lost affects habitat use but not survival in a non-regenerating arthropod. *Ecology and Evolution,* 11**,** 10672-10685.

ESCH, H. 1988. The Effects of Temperature on Flight Muscle Potentials in Honeybees and Cuculiinid Winter Moths. *Journal of Experimental Biology,* 135**,** 109-117.

FABIAN, S. T., SUMNER, M. E., WARDILL, T. J., ROSSONI, S. & GONZALEZ-BELLIDO, P. T. 2018. Interception by two predatory fly species is explained by a proportional navigation feedback controller. *Journal of The Royal Society Interface,* 15**,** 20180466.

FARUQUE, I. & SEAN HUMBERT, J. 2010. Dipteran insect flight dynamics. Part 1 Longitudinal motion about hover. *Journal of Theoretical Biology,* 264**,** 538-552.

FEUERBACHER, E., FEWELL, J. H., ROBERTS, S. P., SMITH, E. F. & HARRISON, J. F. 2003. Effects of load type (pollen or nectar) and load mass on hovering metabolic rate and mechanical power output in the honey bee *Apis mellifera*. *Journal of Experimental Biology,* 206**,** 1855-1865.

FILLINGER, U., DENZ, A., NJOROGE, M. M., TAMBWE, M. M., TAKKEN, W., VAN LOON, J. J. A., MOORE, S. J., SADDLER, A., CHITNIS, N. & HISCOX, A. 2023. A randomized, double-blind placebo-control study assessing the protective efficacy of an odour-based 'push–pull' malaria vector control strategy in reducing human-vector contact. *Scientific Reports,* 13**,** 11197.

FLATT, T. 2020. Life-History Evolution and the Genetics of Fitness Components in Drosophila melanogaster. *Genetics,* 214**,** 3-48.

FONTAINE, E. I., ZABALA, F., DICKINSON, M. H. & BURDICK, J. W. 2009. Wing and body motion during flight initiation in Drosophilarevealed by automated visual tracking. *Journal of Experimental Biology,* 212**,** 1307-1323.

FRY, S. N., SAYAMAN, R. & DICKINSON, M. H. 2003. The Aerodynamics of Free-Flight Maneuvers in Drosophila. *Science,* 300**,** 495.

FRY, S. N., SAYAMAN, R. & DICKINSON, M. H. 2005. The Aerodynamics of Hovering Flight in Drosophila. *Journal of Experimental Biology,* 208**,** 2303-2318.

FULLER, S. B., KARPELSON, M., CENSI, A., MA, K. Y. & WOOD, R. J. 2014. Controlling free flight of a robotic fly using an onboard vision sensor inspired by insect ocelli. *J R Soc Interface,* 11**,** 20140281.

GARCIA CASTILLO, S. S., PRITTS, K. S., KRISHNAN, R. S., HARRINGTON, L. C. & LEAGUE, G. P. 2021. Harmonic convergence coordinates swarm mating by enhancing mate detection in the malaria mosquito Anopheles gambiae. *Scientific Reports,* 11**,** 24102.

GAU, J., LYNCH, J., AIELLO, B., WOLD, E., GRAVISH, N. & SPONBERG, S. 2023. Bridging two insect flight modes in evolution, physiology and robophysics. *Nature,* 622**,** 767-774.

GHOSE, K., TRIBLEHORN, J. D., BOHN, K., YAGER, D. D. & MOSS, C. F. 2009. Behavioral responses of big brown bats to dives by praying mantises. *J Exp Biol,* 212**,** 693-703.

GIBSON, G. & RUSSELL, I. 2006. Flying in Tune: Sexual Recognition in Mosquitoes. *Current Biology,* 16**,** 1311-1316.

GIURFA, M., NÚÑEZ, J., CHITTKA, L. & MENZEL, R. 1995. Colour preferences of flower-naive honeybees. *Journal of Comparative Physiology A,* 177**,** 247-259.

GNATZY, W., GRÜNERT, U. & BENDER, M. 1987. Campaniform sensilla of Calliphora vicina (Insecta, Diptera). *Zoomorphology,* 106**,** 312-319.

GONZALEZ-BELLIDO, P. T., WARDILL, T. J. & JUUSOLA, M. 2011. Compound eyes and retinal information processing in miniature dipteran species match their specific ecological demands. *Proc Natl Acad Sci USA,* 108**,** 4224-9.

GREENWALT, C. H. 1962. Dimensional Relationships for Flying Animals. *Smithsonian Miscellaneous Collections.* City Of Washington: The Smithsonian Insitution.

GREETER, J. S. M. & HEDRICK, T. L. 2016. Direct lateral maneuvers in hawkmoths. *Biology Open,* 5**,** 72-82.

GRIMALDI, D. & ENGEL, M. S. 2005. *Evolution of the Insects,* New York, US, Cambridge University Press.

GULLAN , P. J. & CRANSTON, P. S. 2004. *The Insects: An Outline of Entomology*, Wiley-Blackwell.

HAWKES, F. M. & HOPKINS, R. J. 2022. The mosquito: An introduction. *In:* HALL, M. & TAMÏR, D. (eds.) *Mosquitopia: The Place of Pests in a Healthy World.* New York: Routledge

HEDENSTRÖM, A. 2014. How Insect Flight Steering Muscles Work. *PLOS Biology,* 12**,** e1001822.

HEDRICK, T. L., CHENG, B. & DENG, X. 2009. Wingbeat Time and the Scaling of Passive Rotational Damping in Flapping Flight. *Science,* 324**,** 252-255.

HEDRICK, T. L. & DANIEL, T. L. 2006. Flight control in the hawkmoth Manduca sexta: the inverse problem of hovering. *Journal of Experimental Biology,* 209**,** 3114-3130.

HEIDE, G. & GÖTZ, K. G. 1996. Optomotor Control of Course and Altitude in Drosophila Melanogaster is Correlated With Distinct Activities of at Least Three Pairs of Flight Steering Muscles. *Journal of Experimental Biology,* 199**,** 1711-1726.

HEINRICH, B. 1974. Thermoregulation in Endothermic Insects. *Science,* 185**,** 747-756.

HEINRICH, B. 1979. Thermoregulation of African and European Honeybees during Foraging, Attack, and Hive Exits and Returns. *Journal of Experimental Biology,* 80**,** 217-229.

HELPS, T., ROMERO, C., TAGHAVI, M., CONN, A. T. & ROSSITER, J. 2022. Liquid-amplified zipping actuators for micro-air vehicles with transmission-free flapping. *Science Robotics,* 7**,** eabi8189.

HUANG, J., ZHANG, G. & WANG, Y. 2013. Effects of age, ambient temperature and reproductive status on wing beat frequency of the rice leafroller Cnaphalocrocis medinalis (Guenée) (Lepidoptera: Crambidae). *Applied Entomology and Zoology,* 48**,** 499-505.

HULBERT, A. J. & ELSE, P. L. 2000. Mechanisms Underlying the Cost of Living in Animals. *Annual Review of Physiology,* 62**,** 207-235.

IKEDA, K. & KOENIG, J. H. 1988. Morphological identification of the motor neurons innervating the dorsal longitudinal flight muscle of Drosophila melanogaster. *Journal of Comparative Neurology,* 273**,** 436-444.

ISHIHARA, D. & HORIE, T. 2017. Passive mechanism of pitch recoil in flapping insect wings. *Bioinspiration & Biomimetics,* 12**,** 016008.

ISHIHARA, D., YAMASHITA, Y., HORIE, T., YOSHIDA, S. & NIHO, T. 2009. Passive maintenance of high angle of attack and its lift generation during flapping translation in crane fly wing. *Journal of Experimental Biology,* 212**,** 3882-3891.

IWAMOTO, H. 2011. Structure, function and evolution of insect flight muscle. *Biophysics (Nagoya-shi, Japan),* 7**,** 21-28.

JACKSON, K. M. 1979. Fitting of Mathematical Functions to Biomechanical Data. *IEEE Transactions on Biomedical Engineering,* BME-26**,** 122-124.

JAFFERIS, N. T., HELBLING, E. F., KARPELSON, M. & WOOD, R. J. 2019. Untethered flight of an insect-sized flapping-wing microscale aerial vehicle. *Nature,* 570**,** 491-495.

JEPSON, W. F., MOUTIA, A. & COURTOIS, C. 1947. The Malaria Problem in Mauritius: the Bionomics Of Mauritian Anophelines. *Bulletin of Entomological Research,* 38**,** 177-208.

JOHNSON, B. J., ROHDE, B. B., ZEAK, N., STAUNTON, K. M., PRACHAR, T. & RITCHIE, S. A. 2018. A low-cost, battery-powered acoustic trap for surveilling male Aedes aegypti during rear-and-release operations. *PLOS ONE,* 13**,** e0201709.

JOLLIFFE, I. T. & CADIMA, J. 2016. Principal component analysis: a review and recent developments. *Philosophical Transactions of the Royal Society A: Mathematical, Physical and Engineering Sciences,* 374**,** 20150202.

JONES, A. R. & BABINSKY, H. 2010. Unsteady Lift Generation on Rotating Wings at Low Reynolds Numbers. *Journal of Aircraft,* 47**,** 1013-1021.

JONES, M. P., PIERCE, K. E. & WARD, D. 2007. Avian Vision: A Review of Form and Function with Special Consideration to Birds of Prey. *Journal of Exotic Pet Medicine,* 16**,** 69-87.

JOSEPHSON, R. & ELLINGTON, C. 1997. Power output from a flight muscle of the bumblebee Bombus terrestris. II. CHARACTERIZATION OF THE PARAMETERS AFFECTING POWER OUTPUT. *The Journal of Experimental Biology,* 200**,** 1227–1239

JOSEPHSON, R. K., MALAMUD, J. G. & STOKES, D. R. 2000a. Asynchronous muscle: a primer. *Journal of Experimental Biology,* 203**,** 2713-2722.

JOSEPHSON, R. K., MALAMUD, J. G. & STOKES, D. R. 2000b. Power output by an asynchronous flight muscle from a beetle. *Journal of Experimental Biology,* 203**,** 2667-2689.

JOSEPHSON, R. K., MALAMUD, J. G. & STOKES, D. R. 2001. The efficiency of an asynchronous flight muscle from a beetle. *Journal of Experimental Biology,* 204**,** 4125.

JOSEPHSON, R. K. & YOUNG, D. 1985. A Synchronous Insect Muscle with an Operating Frequency Greater than 500 Hz. *Journal of Experimental Biology,* 118**,** 185.

KARÁSEK, M., MUIJRES, F. T., DE WAGTER, C., REMES, B. D. W. & DE CROON, G. C. H. E. 2018. A tailless aerial robotic flapper reveals that flies use torque coupling in rapid banked turns. *Science,* 361**,** 1089-1094.

KARDUM HJORT, C., SMITH, H. G., ALLEN, A. P. & DUDANIEC, R. Y. 2023. Morphological Variation in Bumblebees (Bombus terrestris) (Hymenoptera: Apidae) After Three Decades of an Island Invasion. *Journal of Insect Science,* 23**,** 10.

KATTI, P., HALL, A. S., PARRY, H. A., AJAYI, P. T., KIM, Y., WILLINGHAM, T. B., BLECK, C. K. E., WEN, H. & GLANCY, B. 2022. Mitochondrial network configuration influences sarcomere and myosin filament structure in striated muscles. *Nature Communications,* 13**,** 6058.

KIM, D., DEBRIERE, T. J., CHERUKUMALLI, S., WHITE, G. S. & BURKETT-CADENA, N. D. 2021. Infrared light sensors permit rapid recording of wingbeat frequency and bioacoustic species identification of mosquitoes. *Scientific Reports,* 11**,** 10042.

KING, D. G. & TANOUYE, M. A. 1983. Anatomy of motor axons to direct flight muscles in Drosophila. *Journal of Experimental Biology,* 105**,** 231 – 239.

KOLOMENSKIY, D., MAEDA, M., ENGELS, T., LIU, H., SCHNEIDER, K. & NAVE, J.-C. 2016. Aerodynamic Ground Effect in Fruitfly Sized Insect Takeoff. *PLOS ONE,* 11**,** e0152072.

KOOI, C. J. V. D., STAVENGA, D. G., ARIKAWA, K., BELUŠIČ, G. & KELBER, A. 2021. Evolution of Insect Color Vision: From Spectral Sensitivity to Visual Ecology. *Annual Review of Entomology,* 66**,** 435-461.

KÜHNE, S. 1998. Open rearing of generalist predators: A strategy for improvement of biological pest control in greenhouses. *Phytoparasitica,* 26**,** 277-281.

LAITONE, E. V. 1997. Wind tunnel tests of wings at Reynolds numbers below 70 000. *Experiments in Fluids,* 23**,** 405-409.

LAND, M. F. 1997. VISUAL ACUITY IN INSECTS. *Annual Review of Entomology,* 42**,** 147-177.

LAND, M. F. & NILSSON, D. E. 2002. *Animal Eyes*, Oxford University Press.

LAUGHLIN, S. B., DE RUYTER VAN STEVENINCK, R. R. & ANDERSON, J. C. 1998. The metabolic cost of neural information. *Nature Neuroscience,* 1**,** 36-41.

LEAGUE, G. P., HARRINGTON, L. C., PITCHER, S. A., GEYER, J. K., BAXTER, L. L., MONTIJO, J., ROWLAND, J. G., JOHNSON, L. M., MURDOCK, C. C. & CATOR, L. J. 2021. Sexual selection theory meets disease vector control: Testing harmonic convergence as a “good genes” signal in Aedes aegypti mosquitoes. *PLOS Neglected Tropical Diseases,* 15**,** e0009540.

LEVINE, J. 1973. Properties of the nervous system controlling flight inDrosophila melanogaster. *Journal of comparative physiology,* 84**,** 129-166.

LI, L., RUTLIN, M., ABRAIRA, VICTORIA E., CASSIDY, C., KUS, L., GONG, S., JANKOWSKI, MICHAEL P., LUO, W., HEINTZ, N., KOERBER, H. R., WOODBURY, C. J. & GINTY, DAVID D. 2011. The Functional Organization of Cutaneous Low-Threshold Mechanosensory Neurons. *Cell,* 147**,** 1615-1627.

LIANG, C. & LI, H. 2018. Aerofoil optimization for improving the power performance of a vertical axis wind turbine using multiple streamtube model and genetic algorithm. *Royal Society Open Science,* 5**,** 180540.

LINARI, M., REEDY, M. K., REEDY, M. C., LOMBARDI, V. & PIAZZESI, G. 2004. Ca-Activation and Stretch-Activation in Insect Flight Muscle. *Biophysical Journal,* 87**,** 1101-1111.

LINDSAY, T., SUSTAR, A. & DICKINSON, M. 2017. The Function and Organization of the Motor System Controlling Flight Maneuvers in Flies. *Current Biology,* 27**,** 345-358.

LIU, H., ELLINGTON, C. P., KAWACHI, K., VAN DEN BERG, C. & WILLMOTT, A. P. 1998. A Computational Fluid Dynamic Study of Hawkmoth Hovering. *Journal of Experimental Biology,* 201**,** 461-477.

LIU, H. & KAWACHI, K. 1998. A Numerical Study of Insect Flight. *Journal of Computational Physics,* 146**,** 124-156.

LIU, L. & SUN, M. 2019. Dynamic flight stability of hovering mosquitoes. *Journal of Theoretical Biology,* 464**,** 149-158.

LIU, Z., YAN, X., QI, M., ZHU, Y., HUANG, D., ZHANG, X. & LIN, L. 2017. Artificial insect wings with biomimetic wing morphology and mechanical properties. *Bioinspiration & Biomimetics,* 12**,** 056007.

LOPEZ-REYES, K., LANKHEET, M. J., VAN TOL, R. W. H. M., BUTLER, R. C., TEULON, D. A. J. & ARMSTRONG, K. F. 2023. Tracking the flight and landing behaviour of western flower thrips in response to single and two-colour cues. *Scientific Reports,* 13**,** 14178.

LOYA, A. K., VAN HOUTEN, S. K., GLASHEEN, B. M. & SWANK, D. M. 2022. Shortening deactivation: quantifying a critical component of cyclical muscle contraction. *American Journal of Physiology-Cell Physiology,* 322**,** C653-C665.

LYU, Y. Z., ZHU, H. J. & SUN, M. 2020. Wing kinematic and aerodynamic compensations for unilateral wing damage in a small phorid fly. *Physical Review E,* 101**,** 012412.

MAGINNIS, T. L. 2006. Leg regeneration stunts wing growth and hinders flight performance in a stick insect (Sipyloidea sipylus). *Proceedings of the Royal Society B: Biological Sciences,* 273**,** 1811-1814.

MAISAK, M. S., HAAG, J., AMMER, G., SERBE, E., MEIER, M., LEONHARDT, A., SCHILLING, T., BAHL, A., RUBIN, G. M., NERN, A., DICKSON, B. J., REIFF, D. F., HOPP, E. & BORST, A. 2013. A directional tuning map of Drosophila elementary motion detectors. *Nature,* 500**,** 212-216.

MANKOWSKA, N. D., MARCINKOWSKA, A. B., WASKOW, M., SHARMA, R. I., KOT, J. & WINKLEWSKI, P. J. 2021. Critical Flicker Fusion Frequency: A Narrative Review. *Medicina* [Online], 57.

MARDEN, J. H. 1989. Bodybuilding Dragonflies: Costs and Benefits of Maximizing Flight Muscle. *Physiological Zoology,* 62**,** 505-521.

MARTÍNEZ, N., ILLESCAS RIQUELME, C. & GARCIA-AVILA, C. 2017. First Report of “Hunter-Fly” Coenosia attenuata (Diptera: Muscidae) in Mexico. *Florida Entomologist,* 100**,** 171-175.

MATEUS, C. 2012. Bioecology and behaviour of Coenosia attenuata in greenhouse vegetable crops in the Oeste region, Portugal. *Bulletin of Insectology,* 65**,** 257-263.

MATTHEWS, N. A. 2008. *Aerial and close-range photogrammetric technology : providing resource documentation, interpretation, and preservation,* Denver, Colo. :, U.S. Department of the Interior, Bureau of Land Management, National Operations Center.

MAYA, R., LERNER, N., BEN-DOV, O., PONS, A. & BEATUS, T. 2023. A hull reconstruction–reprojection method for pose estimation of free-flying fruit flies. *Journal of Experimental Biology,* 226**,** jeb245853.

MELLANBY, K. & HALDANE, J. S. 1934. The site of loss of water from insects. *Proceedings of the Royal Society of London. Series B - Biological Sciences,* 116**,** 139-149.

MEYER-ROCHOW, V. B. 1981. Electrophysiology and histology of the eye of the bumblebee Bombus hortorum (L.) (Hymenoptera: Apidae). *Journal of the Royal Society of New Zealand,* 11**,** 123-153.

MILLER, W. E. 1977. Wing Measure as a Size Index in Lepidoptera: the Family Olethreutidae. *Annals of the Entomological Society of America,* 70**,** 253-256.

MISOF, B., LIU, S., MEUSEMANN, K., PETERS, R. S., DONATH, A., MAYER, C., FRANDSEN, P. B., WARE, J., FLOURI, T., BEUTEL, R. G., NIEHUIS, O., PETERSEN, M., IZQUIERDO-CARRASCO, F., WAPPLER, T., RUST, J., ABERER, A. J., ASPÖCK, U., ASPÖCK, H., BARTEL, D., BLANKE, A., BERGER, S., BÖHM, A., BUCKLEY, T. R., CALCOTT, B., CHEN, J., FRIEDRICH, F., FUKUI, M., FUJITA, M., GREVE, C., GROBE, P., GU, S., HUANG, Y., JERMIIN, L. S., KAWAHARA, A. Y., KROGMANN, L., KUBIAK, M., LANFEAR, R., LETSCH, H., LI, Y., LI, Z., LI, J., LU, H., MACHIDA, R., MASHIMO, Y., KAPLI, P., MCKENNA, D. D., MENG, G., NAKAGAKI, Y., NAVARRETE-HEREDIA, J. L., OTT, M., OU, Y., PASS, G., PODSIADLOWSKI, L., POHL, H., VON REUMONT, B. M., SCHÜTTE, K., SEKIYA, K., SHIMIZU, S., SLIPINSKI, A., STAMATAKIS, A., SONG, W., SU, X., SZUCSICH, N. U., TAN, M., TAN, X., TANG, M., TANG, J., TIMELTHALER, G., TOMIZUKA, S., TRAUTWEIN, M., TONG, X., UCHIFUNE, T., WALZL, M. G., WIEGMANN, B. M., WILBRANDT, J., WIPFLER, B., WONG, T. K. F., WU, Q., WU, G., XIE, Y., YANG, S., YANG, Q., YEATES, D. K., YOSHIZAWA, K., ZHANG, Q., ZHANG, R., ZHANG, W., ZHANG, Y., ZHAO, J., ZHOU, C., ZHOU, L., ZIESMANN, T., ZOU, S., LI, Y., XU, X., ZHANG, Y., YANG, H., WANG, J., WANG, J., KJER, K. M., et al. 2014. Phylogenomics resolves the timing and pattern of insect evolution. *Science,* 346**,** 763.

MIYAN, J. A., EWING, A. W. & LIGHTHILL, M. J. 1985. How Diptera move their wings: a re-examination of the wing base articulation and muscle systems concerned with flight. *Philosophical Transactions of the Royal Society of London. B, Biological Sciences,* 311**,** 271-302.

MORAG, N., MULLENS, B. A. & GOTTLIEB, Y. 2013. Assessment of Survival and Body Size Variation of Culicoides imicola (Diptera: Ceratopogonidae) as Functions of “Candidatus Cardinium” (Bacteroidetes) Infection Status. *Applied and Environmental Microbiology,* 79**,** 6260-6263.

MORDOCH, L., SABAG, E., RIBAK, G. & PINCHASIK, B.-E. 2024. Insect-Inspired Drones: Adjusting the Flapping Kinetics of Insect-Inspired Wings Improves Aerodynamic Performance. *Advanced Intelligent Systems***,** 2400173.

MOUND, L. A. 2009. Chapter 254 - Thysanoptera. *In:* RESH, V. H. & CARDÉ, R. T. (eds.) *Encyclopedia of Insects (Second Edition).* San Diego: Academic Press.

MOUNTCASTLE, A. M. & COMBES, S. A. 2013. Wing flexibility enhances load-lifting capacity in bumblebees. *Proceedings of the Royal Society B: Biological Sciences,* 280**,** 20130531.

MOUNTCASTLE, A. M., RAVI, S. & COMBES, S. A. 2015. Nectar vs. pollen loading affects the tradeoff between flight stability and maneuverability in bumblebees. *Proceedings of the National Academy of Sciences,* 112**,** 10527-10532.

MUIJRES, F. T., CHANG, S. W., VAN VEEN, W. G., SPITZEN, J., BIEMANS, B. T., KOEHL, M. A. R. & DUDLEY, R. 2017. Escaping blood-fed malaria mosquitoes minimize tactile detection without compromising on take-off speed. *Journal of Experimental Biology,* 220**,** 3751-3762.

MUIJRES, F. T., ELZINGA, M. J., IWASAKI, N. A. & DICKINSON, M. H. 2015. Body saccades of Drosophila consist of stereotyped banked turns. *Journal of Experimental Biology,* 218**,** 864-875.

MUIJRES, F. T., ELZINGA, M. J., MELIS, J. M. & DICKINSON, M. H. 2014. Flies Evade Looming Targets by Executing Rapid Visually Directed Banked Turns. *Science,* 344**,** 172-177.

MUIJRES, F. T., JOHANSSON, L. C., BARFIELD, R., WOLF, M., SPEDDING, G. R. & HEDENSTRÖM, A. 2008. Leading-Edge Vortex Improves Lift in Slow-Flying Bats. *Science,* 319**,** 1250-1253.

NABAWY, M. R. A. & CROWTHER, W. J. 2017. The role of the leading edge vortex in lift augmentation of steadily revolving wings: a change in perspective. *Journal of The Royal Society Interface,* 14**,** 20170159.

NAGESH, I., WALKER, S. M. & TAYLOR, G. K. 2019. Motor output and control input in flapping flight: a compact model of the deforming wing kinematics of manoeuvring hoverflies. *Journal of The Royal Society Interface,* 16**,** 20190435.

NAKATA, T., SIMÕES, P., WALKER, S. M., RUSSELL, I. J. & BOMPHREY, R. J. 2022. Auditory sensory range of male mosquitoes for the detection of female flight sound. *Journal of The Royal Society Interface,* 19**,** 20220285.

NGUYEN, Q.-V., CHAN, W. L. & DEBIASI, M. 2016. Hybrid design and performance tests of a hovering insect-inspired flapping-wing micro aerial vehicle. *Journal of Bionic Engineering,* 13**,** 235-248.

NIJHOUT, H. F. & SHEFFIELD, H. G. 1979. Antennal Hair Erection in Male Mosquitoes: A New Mechanical Effector in Insects. *Science,* 206**,** 595-596.

NIVEN, J. E. & LAUGHLIN, S. B. 2008. Energy limitation as a selective pressure on the evolution of sensory systems. *Journal of Experimental Biology,* 211**,** 1792-1804.

NIVEN, J. E. & SCHARLEMANN, J. P. W. 2005. Do insect metabolic rates at rest and during flight scale with body mass? *Biology letters,* 1**,** 346-349.

OLBERDING, J. P. & DEBAN, S. M. 2017. Effects of temperature and force requirements on muscle work and power output. *Journal of Experimental Biology,* 220**,** 2017-2025.

OLBERG, R., WORTHINGTON, A., FOX, J., BESSETTE, C. & LOOSEMORE, M. 2005. Prey size selection and distance estimation in foraging adult dragonflies. *Journal of comparative physiology. A, Neuroethology, sensory, neural, and behavioral physiology,* 191**,** 791-7.

OLBERG, R. M., WORTHINGTON, A. H. & VENATOR, K. R. 2000. Prey pursuit and interception in dragonflies. *Journal of Comparative Physiology A,* 186**,** 155-162.

PALUMBO, N. F., BLAUWKAMP, R. A. & LLOYD, J. M. 2010. Basic Principles of Homing Guidance. *Johns Hopkins Apl Technical Digest,* 29**,** 25-41.

PANTOJA-SÁNCHEZ, H., GOMEZ, S., VELEZ, V., AVILA, F. W. & ALFONSO-PARRA, C. 2019. Precopulatory acoustic interactions of the New World malaria vector Anopheles albimanus (Diptera: Culicidae). *Parasites & Vectors,* 12**,** 386.

PECKHAM, M., CRIPPS, R., WHITE, D. & BULLARD, B. 1992. Mechanics and Protein Content of Insect Flight Muscles. *Journal of Experimental Biology,* 168**,** 57-76.

PENNETIER, C., WARREN, B., DABIRÉ, K. R., RUSSELL, I. J. & GIBSON, G. 2010. “Singing on the Wing” as a Mechanism for Species Recognition in the Malarial Mosquito Anopheles gambiae. *Current Biology,* 20**,** 131-136.

PEREZ, J. M., ALEDO, P. G. & SANCHEZ, P. P. 2012. Real-time voxel-based visual hull reconstruction. *Microprocessors and Microsystems,* 36**,** 439-447.

PERZ-EDWARDS, R. J., IRVING, T. C., BAUMANN, B. A. J., GORE, D., HUTCHINSON, D. C., KRŽIČ, U., PORTER, R. L., WARD, A. B. & REEDY, M. K. 2011. X-ray diffraction evidence for myosin-troponin connections and tropomyosin movement during stretch activation of insect flight muscle. *Proceedings of the National Academy of Sciences,* 108**,** 120.

PICHAUD, F. & CASARES, F. 2022. Shaping an optical dome: The size and shape of the insect compound eye. *Seminars in Cell & Developmental Biology,* 130**,** 37-44.

PONITZ, B., SCHMITZ, A., FISCHER, D., BLECKMANN, H. & BRÜCKER, C. 2014. Diving-Flight Aerodynamics of a Peregrine Falcon (Falco peregrinus). *PLOS ONE,* 9**,** e86506.

PROVINI, P., CAMP, A. L. & CRANDELL, K. E. 2023. Emerging biological insights enabled by high-resolution 3D motion data: promises, perspectives and pitfalls. *Journal of Experimental Biology,* 226**,** jeb245138.

QIU, F., LAKEY, A., AGIANIAN, B., HUTCHINGS, A., BUTCHER, G. W., LABEIT, S., LEONARD, K. & BULLARD, B. 2003. Troponin C in different insect muscle types: identification of two isoforms in Lethocerus, Drosophila and Anopheles that are specific to asynchronous flight muscle in the adult insect. *Biochemical Journal,* 371**,** 811-821.

QUAN, Y., WANG, Z., WEI, H. & HE, K. 2022. Transcription dynamics of heat shock proteins in response to thermal acclimation in Ostrinia furnacalis. *Frontiers in Physiology,* 13.

RAY, R. P., NAKATA, T., HENNINGSSON, P. & BOMPHREY, R. J. 2016. Enhanced flight performance by genetic manipulation of wing shape in Drosophila. *Nature communications,* 7**,** 10851-10851.

RAYNER, J. M. V. & BONE, Q. 1997. On the aerodynamics of animal flight in ground effect. *Philosophical Transactions of the Royal Society of London. Series B: Biological Sciences,* 334**,** 119-128.

REID, G., MCCORMACK, J. C., HABIMANA, O., BAYER, F., GOROMONZI, C., CASEY, E., COWLEY, A. & KELLEHER, S. M. 2021. Biomimetic Polymer Surfaces by High Resolution Molding of the Wings of Different Cicadas. *Materials* [Online], 14.

REINHOLD, J. M., LAZZARI, C. R. & LAHONDÈRE, C. 2018. Effects of the Environmental Temperature on Aedes aegypti and Aedes albopictus Mosquitoes: A Review. *Insects,* 9**,** 158.

RIBAK, G., BARKAN, S. & SOROKER, V. 2017. The aerodynamics of flight in an insect flight-mill. *PLOS ONE,* 12**,** e0186441.

RISKIN, D. K., WILLIS, D. J., IRIARTE-DÍAZ, J., HEDRICK, T. L., KOSTANDOV, M., CHEN, J., LAIDLAW, D. H., BREUER, K. S. & SWARTZ, S. M. 2008. Quantifying the complexity of bat wing kinematics. *Journal of Theoretical Biology,* 254**,** 604-615.

RISTROPH, L., RISTROPH, G., MOROZOVA, S., BERGOU, A. J., CHANG, S., GUCKENHEIMER, J., WANG, Z. J. & COHEN, I. 2013. Active and

passive stabilization of body pitch in insect flight. *Journal of The Royal Society Interface,* 10**,** 20130237.
ROSS, A. 2017. Insect Evolution: The Origin of Wings. *Current Biology,* 27**,** R113-R115.
ROSSONI, S., FABIAN, S. T., SUTTON, G. P. & GONZALEZ-BELLIDO, P. T. 2021. Gravity and active acceleration limit the ability of killer flies (Coenosia attenuata) to steer towards prey when attacking from above. *Journal of The Royal Society Interface,* 18**,** 20210058.
ROTHE, U. & NACHTIGALL, W. 1989. Flight of the honey bee. *Journal of Comparative Physiology B,* 158**,** 739-749.
SAITO, K., NAGAI, H., SUTO, K., OGAWA, N., SEONG, Y. A., TACHI, T., NIIYAMA, R. & KAWAHARA, Y. 2021. Insect wing 3D printing. *Scientific Reports,* 11**,** 18631.
SALLUM, M. A. M., OBANDO, R. G., CARREJO, N. & WILKERSON, R. C. 2020. Identification keys to the Anopheles mosquitoes of South America (Diptera: Culicidae). IV. Adult females. *Parasites & Vectors,* 13**,** 584.
SCHOUEST JR, L. P., ANDERSON, M. & MILLER, T. A. 1986. The ultrastructure and physiology of the tergotrochanteral depressor muscle of the housefly, Musca domestica. *Journal of Experimental Zoology,* 239**,** 147-158.
SHERK, T. E. 1978. Development of the compound eyes of dragonflies (Odonata). III. Adult compound eyes. *J Exp Zool,* 203**,** 61-80.
SIMMONS, P. J. 1982. The function of insect ocelli. *Trends in Neurosciences,* 5**,** 182-183.
SKEJØ, S. D., LUND, M. E., STENSVIG, M., KAAE, N. M. & RASMUSSEN, J. 2021. Running in circles: Describing running kinematics using Fourier series. *Journal of Biomechanics,* 115**,** 110187.
SMITH, N. M., BALSALOBRE, J. B., DOSHI, M., WILLENBERG, B. J. & DICKERSON, A. K. 2020. Landing mosquitoes bounce when engaging a substrate. *Scientific Reports,* 10**,** 15744.
SMITH, N. M., CLAYTON, G. V., KHAN, H. A. & DICKERSON, A. K. 2018. Mosquitoes modulate leg dynamics at takeoff to accommodate surface roughness. *Bioinspiration & Biomimetics,* 14**,** 016007.
SNELLING, E. P., SEYMOUR, R. S., MATTHEWS, P. G. D. & WHITE, C. R. 2012. Maximum metabolic rate, relative lift, wingbeat frequency and stroke amplitude during tethered flight in the adult locust Locusta migratoria. *Journal of Experimental Biology,* 215**,** 3317-3323.
SOMERS, J., GEORGIADES, M., SU, M. P., BAGI, J., ANDRÉS, M., ALAMPOUNTI, A., MILLS, G., NTABALIBA, W., MOORE, S. J., SPACCAPELO, R. & ALBERT, J. T. 2022. Hitting the right note at the right time: Circadian control of audibility in Anopheles mosquito mating swarms is mediated by flight tones. *Science Advances,* 8**,** eabl4844.
SOTAVALTA, O. 1952. Flight-Tone and Wing-Stroke Frequency of Insects and the Dynamics of Insect Flight. *Nature,* 170**,** 1057-1058.
SRISUKA, W., SULIN, C., SOMMITR, W., RATTANARITHIKUL, R., AUPALEE, K., SAEUNG, A. & HARBACH, R. E. 2022. Mosquito (Diptera: Culicidae) Diversity and Community Structure in Doi Inthanon National Park, Northern Thailand. *Insects* [Online], 13.
STEINMANN, T., CASAS, J., KRIJNEN, G. & DANGLES, O. 2006. Air-flow sensitive hairs: boundary layers in oscillatory flows around arthropod appendages. *Journal of Experimental Biology,* 209**,** 4398-4408.

STEVENSON, R. D. & JOSEPHSON, R. K. 1990. EFFECTS OF OPERATING FREQUENCY AND TEMPERATURE ON MECHANICAL POWER OUTPUT FROM MOTH FLIGHT MUSCLE. *Journal of Experimental Biology,* 149**,** 61-78.

STONE, G. N. & WILLMER, P. G. 1989. Warm-Up Rates and Body Temperatures in Bees: The Importance of Body Size, Thermal Regime and Phylogeny. *Journal of Experimental Biology,* 147**,** 303-328.

STORK, N. E. 2018. How Many Species of Insects and Other Terrestrial Arthropods Are There on Earth? *Annual Review of Entomology,* 63**,** 31-45.

STREINZER, M., BROCKMANN, A., NAGARAJA, N. & SPAETHE, J. 2013. Sex and Caste-Specific Variation in Compound Eye Morphology of Five Honeybee Species. *PLOS ONE,* 8**,** e57702.

SUAREZ, R. K. 2000. Energy Metabolism during Insect Flight: Biochemical Design and Physiological Performance. *Physiological and Biochemical Zoology,* 73**,** 765-771.

SUN, M. & TANG, J. 2002. Unsteady aerodynamic force generation by a model fruit fly wing in flapping motion. *Journal of Experimental Biology,* 205**,** 55-70.

SYME, D. A. & JOSEPHSON, R. K. 2002. How to Build Fast Muscles: Synchronous and Asynchronous Designs. *Integrative and Comparative Biology,* 42**,** 762-770.

TAYLOR, G. K. 2012. Wings and flight. *In:* DOUGLAS, A. E., CHAPMAN, R. F. & SIMPSON, S. J. (eds.) *The Insects: Structure and Function.* 5 ed. Cambridge: Cambridge University Press.

TERCEL, M. P. T. G., VERONESI, F. & POPE, T. W. 2018. Phylogenetic clustering of wingbeat frequency and flight-associated morphometrics across insect orders. *Physiological Entomology,* 43**,** 149-157.

THYSELIUS, M., OGAWA, Y., LEIBBRANDT, R., WARDILL, T. J., GONZALEZ-BELLIDO, P. T. & NORDSTRÖM, K. 2023. Hoverfly (Eristalis tenax) pursuit of artificial targets. *Journal of Experimental Biology,* 226**,** jeb244895.

TRIMARCHI, J. R. & SCHNEIDERMAN, A. M. 1994. The motor neurons innervating the direct flight muscles of Drosophila melanogaster are morphologically specialized. *Journal of Comparative Neurology,* 340**,** 427-443.

TRUONG, T. V., BYUN, D., KIM, M. J., YOON, K. J. & PARK, H. C. 2013. Aerodynamic forces and flow structures of the leading edge vortex on a flapping wing considering ground effect. *Bioinspiration & Biomimetics,* 8**,** 036007.

UNWIN, D. M. & CORBET, S. A. 1984. Wingbeat frequency, temperature and body size in bees and flies. *Physiological Entomology,* 9**,** 115-121.

URCA, T., DEBNATH, A. K., STEFANINI, J., GURKA, R. & RIBAK, G. 2020. The Aerodynamics and Power Requirements of Forward Flapping Flight in the Mango Stem Borer Beetle (Batocera rufomaculata). *Integrative Organismal Biology,* 2**,** obaa026.

USHERWOOD, J. R., STAVROU, M., LOWE, J. C., ROSKILLY, K. & WILSON, A. M. 2011. Flying in a flock comes at a cost in pigeons. *Nature,* 474**,** 494-497.

VAN VEEN, W. G., VAN LEEUWEN, J. L. & MUIJRES, F. T. 2020. Malaria mosquitoes use leg push-off forces to control body pitch during take-off.

Journal of Experimental Zoology Part A: Ecological and Integrative Physiology, 333**,** 38-49.

VEMURI, R., LANKFORD, E. B., POETTER, K., HASSANZADEH, S., TAKEDA, K., YU, Z. X., FERRANS, V. J. & EPSTEIN, N. D. 1999. The stretch-activation response may be critical to the proper functioning of the mammalian heart. *Proceedings of the National Academy of Sciences of the United States of America,* 96**,** 1048-1053.

VIDELER, J. 1995. Body surface adaptations to boundary-layer dynamics. *Symposia of the Society for Experimental Biology,* 49**,** 1-20.

VIJAYAN, S., BALAMURALI, G. S., JOHNSON, J., KELBER, A., WARRANT, E. J. & SOMANATHAN, H. 2023. Dim-light colour vision in the facultatively nocturnal Asian giant honeybee, Apis dorsata. *Proceedings of the Royal Society B: Biological Sciences,* 290**,** 20231267.

VILLARREAL, S. M., WINOKUR, O. & HARRINGTON, L. 2017. The Impact of Temperature and Body Size on Fundamental Flight Tone Variation in the Mosquito Vector Aedes aegypti (Diptera: Culicidae): Implications for Acoustic Lures. *Journal of Medical Entomology,* 54**,** 1116-1121.

WALKER, J. A. 2002. Rotational lift: something different or more of the same? *Journal of Experimental Biology,* 205**,** 3783-3792.

WALKER, S. M., SCHWYN, D. A., MOKSO, R., WICKLEIN, M., MÜLLER, T., DOUBE, M., STAMPANONI, M., KRAPP, H. G. & TAYLOR, G. K. 2014. In Vivo Time-Resolved Microtomography Reveals the Mechanics of the Blowfly Flight Motor. *PLOS Biology,* 12**,** 1-12.

WALKER, S. M. & TAYLOR, G. K. 2021. A semi-empirical model of the aerodynamics of manoeuvring insect flight. *Journal of The Royal Society Interface,* 18**,** 20210103.

WALKER, S. M., THOMAS, A. L. R. & TAYLOR, G. K. 2008. Deformable wing kinematics in the desert locust: how and why do camber, twist and topography vary through the stroke? *Journal of The Royal Society Interface,* 6**,** 735-747.

WALKER, S. M., THOMAS, A. L. R. & TAYLOR, G. K. 2009. Photogrammetric reconstruction of high-resolution surface topographies and deformable wing kinematics of tethered locusts and free-flying hoverflies. *Journal of the Royal Society, Interface,* 6**,** 351-366.

WALKER, S. M., THOMAS, A. L. R. & TAYLOR, G. K. 2012. Operation of the alula as an indicator of gear change in hoverflies. *Journal of The Royal Society Interface,* 9**,** 1194-1207.

WAN, D.-J., CHEN, J., JIANG, L.-B., GE, L.-Q. & WU, J.-C. 2013. Effects of the insecticide triazophos on the ultrastructure of the flight muscle of the brown planthopper Nilaparvata lugens Stål (Hemiptera: Delphacidae). *Crop Protection,* 43**,** 54-59.

WARDILL, T. J., FABIAN, S. T., PETTIGREW, A. C., STAVENGA, D. G., NORDSTRÖM, K. & GONZALEZ-BELLIDO, P. T. 2017. A Novel Interception Strategy in a Miniature Robber Fly with Extreme Visual Acuity. *Curr Biol,* 27**,** 854-859.

WARDILL, T. J., KNOWLES, K., BARLOW, L., TAPIA, G., NORDSTRÖM, K., OLBERG, R. M. & GONZALEZ-BELLIDO, P. T. 2015. The Killer Fly Hunger Games: Target Size and Speed Predict Decision to Pursuit. *Brain, Behavior and Evolution,* 86**,** 28-37.

WARRICK, D. R., TOBALSKE, B. W. & POWERS, D. R. 2009. Lift production in the hovering hummingbird. *Proceedings. Biological sciences,* 276**,** 3747-3752.

WEBER, G. F. & MENKO, A. S. 2005. Color image acquisition using a monochrome camera and standard fluorescence filter cubes. *BioTechniques,* 38**,** 52-56.

WEI, H., KYUNG, H. Y., KIM, P. J. & DESPLAN, C. 2020. The diversity of lobula plate tangential cells (LPTCs) in the Drosophila motion vision system. *Journal of Comparative Physiology A,* 206**,** 139-148.

WEIBEL, E. R. 2002. The pitfalls of power laws. *Nature,* 417**,** 131-132.

WHEELWRIGHT, M., WHITTLE, C. R. & RIABININA, O. 2021. Olfactory systems across mosquito species. *Cell and Tissue Research,* 383**,** 75-90.

WISSER, A. & NACHTIGALL, W. 1984. Functional-morphological investigations on the flight muscles and their insertion points in the blowfly Calliphora erythrocephala (Insecta, Diptera). *Zoomorphology,* 104**,** 188-195.

WITTE, K., SCHOBESBERGER, H. & PEHAM, C. 2009. Motion pattern analysis of gait in horseback riding by means of Principal Component Analysis. *Human Movement Science,* 28**,** 394-405.

XU, H. & ROBERTSON, R. M. 1994. Effects of temperature on properties of flight neurons in the locust. *Journal of Comparative Physiology A,* 175**,** 193-202.

ZANKER, J. M. 1988. How does lateral abdomen deflection contribute to flight control of Drosophila melanogaster? *Journal of Comparative Physiology A,* 162**,** 581-588.

ZELHOF, A. C., HARDY, R. W., BECKER, A. & ZUKER, C. S. 2006. Transforming the architecture of compound eyes. *Nature,* 443**,** 696-699.

Appendix

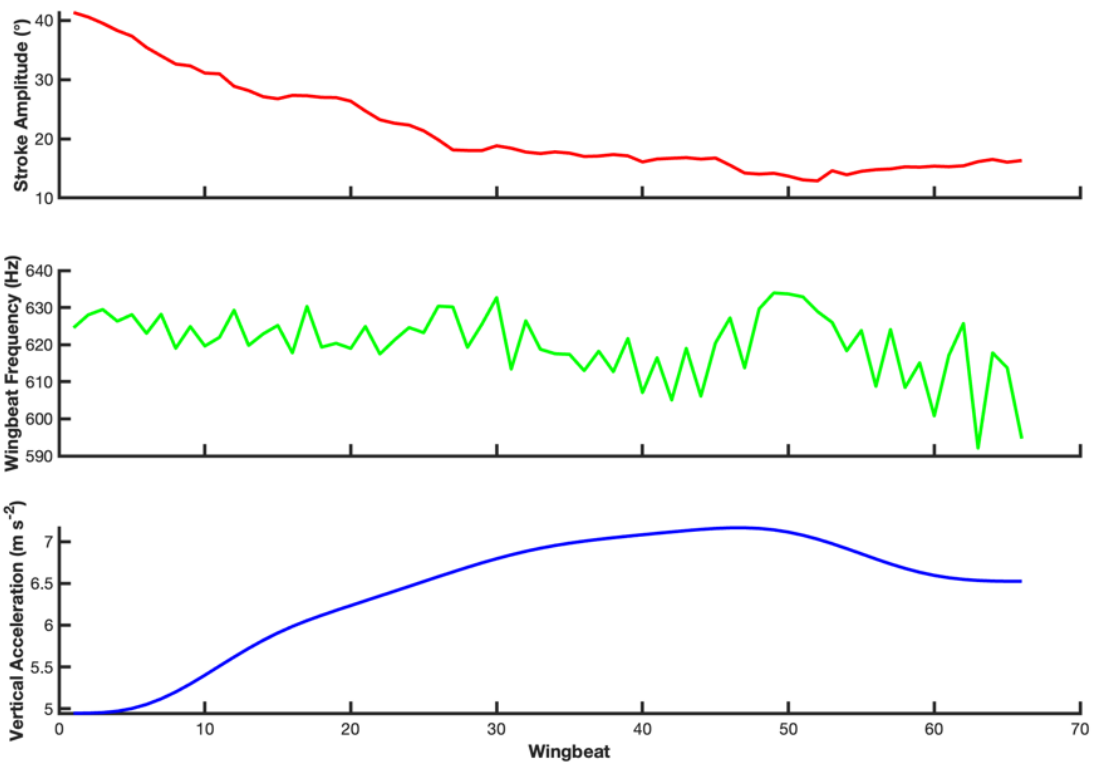

Figure 0.1 Wingbeat parameters for the sequence recorded with the lowest stroke amplitude (12.9 º)

Stroke amplitude (red), wingbeat frequency (green) and vertical acceleration (blue) over 66 wingbeats.

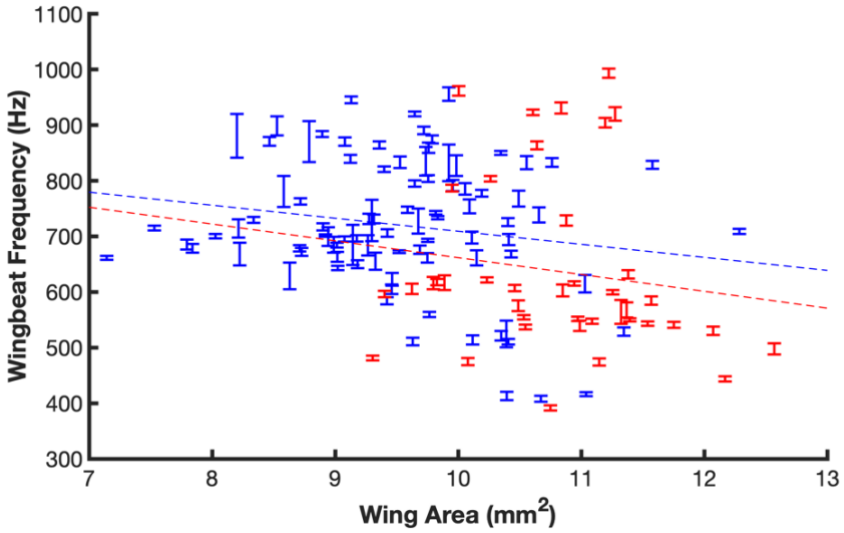

Figure 0.2 Wing area versus wingbeat frequency

Males in blue (N = 90, R^2 = 0.0313 and P = 0.0970) and females in red (N = 39 , R^2 = 0.0212 and P = 0.370). Vertical bars denote the mean and standard deviation of each mosquito recorded.

Table 0.1 Leg kinematic parameter column statistics

	Swing Angle							
	N	Min.	Q_1	Median	Q_3	Max.	Mean	SD
L1_GP9	6188	-64.2	-48.99	-45.25	-40.65	-13.23	-44.93	6.703
L1_GP2	2397	-58.19	-46.46	-42.15	-38.76	-28.67	-42.58	5.945
L1_GP4	1424	-56.42	-42.45	-40.52	-37.79	-27.05	-40.1	4.683
L2_GP9	6142	-47.65	-22.96	-14.08	-5.329	59.86	-14.27	13.41
L2_GP2	2387	-38.73	-12.47	-3.758	6.541	21.28	-4.38	13.74
L2_GP4	1285	-17.93	3.154	13.86	19.66	38.71	11.79	11.04
L3_GP9	6059	-13.9	49.74	62.24	68.92	90.04	59.42	12.71
L3_GP2	1069	42.34	65.27	72.14	78.98	87.76	71.1	10.12
R1_GP9	5999	-61.64	-47.49	-43.01	-39.97	-26.58	-44.05	5.368
R1_GP2	2397	-65.31	-46.31	-42.47	-39.07	-27.28	-43.11	6.338
R1_GP4	1424	-54.4	-47	-42.78	-36.36	-29.42	-41.85	5.872
R2_GP9	6188	-53.03	-19.94	-13.98	-6.02	77.06	-11.92	15.9
R2_GP2	2397	-41.35	-12.84	-3.793	7.937	48.82	-2.93	14.21

R2_GP4	891	-19.4	-3.884	3.922	8.809	34.01	2.868	10.48
R3_GP9	6188	-0.5828	51.83	61.66	69.12	205.4	60.28	14.94
R3_GP2	1286	20.5	61.26	71.7	80.22	92.7	70.69	11.97

	Elevation Angle							
	N	Min.	Q_1	Median	Q_3	Max.	Mean	SD
L1_GP9	6188	-51.48	-30.46	-23.38	-11.05	8.833	-21.44	12.84
L1_GP2	2397	-53.8	-28.78	-21.43	-13.5	10.89	-21.11	11.66
L1_GP4	1424	-42.7	-23.94	-17.17	-6.808	4.801	-16.01	11.28
L2_GP9	6142	-64.21	3.964	16.14	30.03	58.24	16.94	17.26
L2_GP2	2387	-23	8.039	18.03	29.31	59.36	18.14	15.94
L2_GP4	1285	-23.26	1.931	16.63	28.96	53.59	16.08	16
L3_GP9	6059	-67.62	-17.34	9.239	25.02	58.46	3.74	26.78
L3_GP2	1069	-56.22	-20.8	-6.729	16.95	40.11	-4.779	24.34
R1_GP9	5999	-59.85	-29	-21.94	-14.48	7.694	-21.54	11.52
R1_GP2	2397	-52.57	-30.03	-22.01	-16.84	10.15	-22.91	11.61
R1_GP4	1424	-48.73	-32.44	-22.01	-8.481	10.38	-20.48	14.8
R2_GP9	6188	-68.39	3.269	12.8	24.88	55.76	14.15	14.75
R2_GP2	2397	-16.71	3.51	16.42	26.68	64.93	16.38	15.82
R2_GP4	891	-10.49	11.12	18.12	26.53	58.53	19.47	13.16
R3_GP9	6188	-58.75	-20.97	2.348	25.03	83.48	2.375	27.63
R3_GP2	1286	-63.36	-19.73	9.319	26.86	52.44	4.103	28.82

Q_1 is the first quartile (25 % percentile) and Q_3 is the third quartile (75 % percentile).